

AD-A077 351

ATLANTIC RESEARCH CORP ALEXANDRIA VA
TURBULENT BOUNDARY-LAYER ANALYSIS AND EXPERIMENTAL INVESTIGATION--ETC(U)
MAR 79 M K RAZDAN , K K KUO

F/G 21/9.2

F49620-78-C-0016

UNCLASSIFIED

AFOSR-TR-79-1155

NL

1 OF 3
AD-A077351



AD A 077351



LEVEL

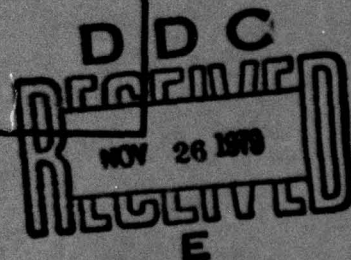
TURBULENT BOUNDARY-LAYER ANALYSIS AND
EXPERIMENTAL INVESTIGATION OF EROSION
BURNING PROBLEM OF COMPOSITE SOLID PROPELLANTS

Scientific Report
October 1, 1977 to September 30, 1978

Sponsored by
U.S. Air Force Office of Scientific Research
Under a Subcontract From
Atlantic Research Corporation
Alexandria, Virginia
Contract No. F49620-78-C-0016

Prepared by
Mohan K. Razdan and Kenneth K. Kuo

March, 1979



DDC FILE COPY

79 11 23 023

THE PENNSYLVANIA STATE UNIVERSITY
College of Engineering
Department of Mechanical Engineering
University Park, Pennsylvania

REPORT DOCUMENTATION PAGE

READ INSTRUCTIONS
BEFORE COMPLETING FORM

1. REPORT NUMBER 19 AFOSR-TR-79-1155	2. GOVT ACCESSION NO.	3. RECIPIENT'S CATALOG NUMBER
4. TITLE (and Subtitle) TURBULENT BOUNDARY-LAYER ANALYSIS AND EXPERIMENTAL INVESTIGATION OF EROSION BURNING PROBLEM OF COMPOSITE SOLID PROPELLANTS	5. TYPE OF REPORT & PERIOD COVERED 9 INTERIM Rept. 1 Oct 77 - 30 Sep 78	
7. AUTHOR(s) MOHAN K/RAZDAN KENNETH E/KUO	8. CONTRACT OR GRANT NUMBER(s) 15 F49620-78-C-0016	6. PERFORMING ORG. REPORT NUMBER
9. PERFORMING ORGANIZATION NAME AND ADDRESS ATLANTIC RESEARCH CORPORATION 5390 CHEROKEE AVENUE ALEXANDRIA, VA 22314	10. PROGRAM ELEMENT, PROJECT, TASK AREA & WORK UNIT NUMBERS 16 2308A1 17 A1 61102F	
11. CONTROLLING OFFICE NAME AND ADDRESS AIR FORCE OFFICE OF SCIENTIFIC RESEARCH/NA BLDG 410 BOLLING AIR FORCE BASE, D C 20332	12. REPORT DATE 11 Mar 1979	
14. MONITORING AGENCY NAME & ADDRESS (if different from Controlling Office)	13. NUMBER OF PAGES 103	
	15. SECURITY CLASS. (of this report) UNCLASSIFIED	
15a. DECLASSIFICATION/DOWNGRADING SCHEDULE		
16. DISTRIBUTION STATEMENT (of this Report) Approved for public release; distribution unlimited.		
17. DISTRIBUTION STATEMENT (of the abstract entered in Block 20, if different from Report)		
18. SUPPLEMENTARY NOTES		
19. KEY WORDS (Continue on reverse side if necessary and identify by block number) EROSIVE BURNING COMPOSITE SOLID PROPELLANTS REACTIVE FLOWS TURBULENT BOUNDARY LAYER		
20. ABSTRACT (Continue on reverse side if necessary and identify by block number) The purpose of this study was to investigate the frequently encountered phenomenon of erosive burning of composite solid propellants in rocket motors. Both theoretical and experimental studies were undertaken. In the theoretical model, the propellant burning process was described by considering a steady, two-dimensional, chemically reacting, turbulent boundary layer over a propellant surface. The diffusion-controlled gas-phase chemical reaction was modeled on the basis of the eddy-break-up concept. The theoretical model, comprised of a set of partial differential equations, was solved numerically. In the experimental		

DD FORM 1 JAN 73 1473

045 550

UNCLASSIFIED

~~Unclassified~~

work, a flat composite-propellant slab was burned in a test chamber by the flow of hot combustion gases which formed a turbulent boundary layer over the surface of the propellant. The burning rate of the propellant was measured by a high-speed motion picture technique at various pressures and free-stream velocities. Comparison of the theoretical results with the experimental data, obtained from the present study and that obtained from existing literature, showed a close agreement. A correlation was developed for the erosive burning rate in terms of pressure and free-stream velocity. From the results of this study, the erosive burning effect is believed to be caused by the increase in gas-to-solid heat feedback introduced by the increase in transport coefficients, and the turbulence-enhanced mixing and reaction of the oxidizer and fuel gases.

UNCLASSIFIED

SECURITY CLASSIFICATION OF THIS PAGE(When Data Entered)

(12)

TURBULENT BOUNDARY-LAYER ANALYSIS AND
EXPERIMENTAL INVESTIGATION OF EROSION
BURNING PROBLEM OF COMPOSITE SOLID PROPELLANTS

Scientific Report

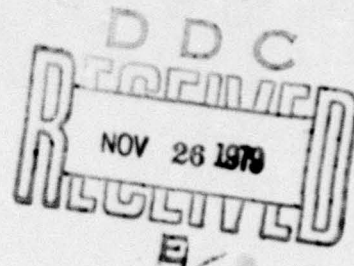
October 1, 1977 to September 30, 1978

Sponsored By

Air Force Office of Scientific Research
Bolling Air Force Base, Washington, D.C.

Under a subcontract from
Atlantic Research Corporation
Alexandria, Virginia

Contract No. F49620-78-C0016



The views and conclusions contained in this document are those of the authors and should not be interpreted as necessarily representing official policies, either expressed or implied, of the Air Force Office of Scientific Research of the U.S. Government.

Prepared by

Mohan K. Razdan, Telephone (814)863-0359
Kenneth K. Kuo, Telephone (814)865-6741

Mechanical Engineering Department
The Pennsylvania State University
University Park, Pennsylvania 16802

AIR FORCE OFFICE OF SCIENTIFIC RESEARCH (AFSC)
NOTICE OF TRANSMITTAL TO DDC
This technical report has been reviewed and is
approved for public release IAW AFR 190-12 (7b).
Distribution is unlimited.
A. D. BLOSE
Technical Information Officer

79 11 23 023

ACKNOWLEDGEMENTS

This research has been sponsored by the Air Force Office of Scientific Research (AFOSR), Bolling Air Force Base, Washington, D.C., under a subcontract (Contract No. F49620-78-C-0016) from Atlantic Research Corporation which was the prime contractor for AFOSR. ✓

The project manager for this contract was Capt. R. F. Sperlein of the AFOSR. Dr. Daweel George of the Air Force Rocket Propulsion Laboratory (AFRPL), Edwards Air Force Base in California, has supplied test propellant samples and N-4 rocket propellant grains. Their support and help is greatly appreciated.

The assistance of Mr. Carl Chambers of Redstone Arsenal who has supplied MK 125 igniters is acknowledged.

The assistance of members of the College of Engineering is also gratefully acknowledged as follows: Mr. R. L. Kovalcin, Mr. W. D. Jones and Mr. S. M. Kovacic, for their help in the experimental work of this study; Mr. R. Houtz and Mr. S. Gulbernath, for fabrication of the test rig. We would also like to thank Mrs. Mary Jane Coleman for typing this report.

Accession For	
NTIS GRA&I	<input checked="checked" type="checkbox"/>
DDC TAB	<input type="checkbox"/>
Unannounced	<input type="checkbox"/>
Justification	
By _____	
Distribution/	
Availability Codes	
Dist	Avail and/or special
A	

TABLE OF CONTENTS

	<u>Page</u>
ACKNOWLEDGEMENTS	i
LIST OF TABLES	v
LIST OF FIGURES	vi
NOMENCLATURE	ix
CHAPTER 1 INTRODUCTION	1
1.1 Physical Description of Erosive-Burning Problem	1
1.2 Previous Related Studies	4
1.2.1 Erosive Burning Studies	4
1.2.2 Steady State Combustion Studies	6
1.2.3 Turbulent Flow Studies	10
1.3 Research Motivation and Objectives	13
CHAPTER 2 THEORETICAL MODELING	15
2.1 Description of the Physical Model	15
2.2 Conservation Equations	17
2.3 Turbulence Closure Models	22
2.4 Modeling of Gas-Phase Chemical Reactions	28
2.5 Burning Rate Equation	33
2.6 Boundary Conditions	34
CHAPTER 3 NUMERICAL METHOD	40
3.1 Numerical Scheme	40
3.2 Procedure in the Development of the Computer Code	44
3.3 Verification of the Numerical Solutions Under Various Boundary-Layer Flow Conditions	46
3.4 Iteration Procedure for Burning Rate Calculation	55

TABLE OF CONTENTS (continued)

	<u>Page</u>
CHAPTER 4 EXPERIMENTAL WORK	56
4.1 Burning Rate Measurement	58
4.1.1 Laser-Photodiode Servomechanism Method	58
4.1.2 High-Speed Motion Picture Method	60
4.2 Erosive-Burning Test-Rig Design	61
4.2.1 Driving Motor	61
4.2.2 Igniter System	66
4.2.3 Test Chamber	66
4.2.4 Feed Mechanism and Pressure Equalizer Chamber	70
4.3 Instrumentation	72
4.3.1 Pressure Measuring Equipment	72
4.3.2 Camera System	73
4.3.3 Motion Analyzer	73
4.3.4 Data Acquisition System	74
4.3.5 Remotely Controlled Ignition System	76
4.4 Procedure Used in Conducting Erosive-Burning Test Firings	78
CHAPTER 5 DISCUSSION OF RESULTS	81
5.1 Experimental Results	81
5.1.1 Discussion of Erosive-Burning Data	81
5.1.2 Comparison of Theoretical Results with Experimental Data	91
5.2 Boundary-Layer Solutions of the Theoretical Model	100
CHAPTER 6 SUMMARY AND CONCLUSION	119
6.1 Summary	119
6.2 Conclusions	121
6.3 Recommendations for Future Study	123
6.3.1 Theoretical Work	123
6.3.2 Experimental Work	124

TABLE OF CONTENTS (continued)

	<u>Page</u>
REFERENCES	125
APPENDIX A ORDER-OF-MAGNITUDE ANALYSIS	132
APPENDIX B NEAR-WALL TREATMENT IN THE NUMERICAL PROCEDURE	140
APPENDIX C FINITE-DIFFERENCE EQUATIONS	144
APPENDIX D PARAMETRIC STUDY IN THE EROSION-BURNING TEST-RIG DESIGN	153
APPENDIX E A SAMPLE CHECK LIST AND DATA SHEET FOR EROSION- BURNING TEST FIRINGS	164
APPENDIX F FREE-STREAM VELOCITY CALCULATION	171
APPENDIX G TABULATED EXPERIMENTAL DATA FOR EROSION-BURNING RATES AT VARIOUS PRESSURES AND FREE-STREAM VELOCITIES	175

LIST OF TABLES

<u>Table</u>	<u>Caption</u>	<u>Page</u>
1	Comparison of Various Experimental Techniques for Measuring Erosive-Burning Rates	7
2	Values of the Constants Used in Turbulence Modeling	53
3	Properties of N-4 Solid Propellant Grain	64
4	Properties Used in Theoretical Calculations	101
C.1	Coefficients in the Finite-Difference Equations of Each Dependable Variable	149
D.1	Properties Used in Parametric Study	159

LIST OF FIGURES

<u>Figure</u>	<u>Caption</u>	<u>Page</u>
1	Two-Stage GDF Model for Ammonium Perchlorate Type Composite Solid Propellants	8
2	Effect of Free-Stream Velocity on the Domain of Turbulence Near the Propellant Surface	11
3	Comparison of Viscous Sublayer Thickness and Diffusion Flame Thickness	11
4	Physical Model Considered in the Theoretical Analysis	16
5	Interface Mass and Energy Balances at the Propellant Surface	35
6	General Layout of the Computer Program	45
7	Comparison of Calculated Velocity and Temperature Profiles with Van Driest's Solution for a Highly Compressible Supersonic Boundary Layer	47
8	Comparison of Calculated Velocity Profiles with the Experimental Data Measured by Head in a Laminar Boundary Layer with Suction	48
9	Comparison of Calculated Temperature Profiles with Solutions of Sparrow and Yu for a Laminar Boundary Layer with Blowing	49
10	Comparison of Calculated Turbulent Boundary-Layer Results with Klebanoff's Measurements	50
11	Calculated Skin-Friction Coefficient for Incompressible Turbulent Boundary Layer over a Flat Plate	51
12	Schematic Diagram of Laser-Photodiode Servomechanism	59
13	Schematic Diagram of the Erosive-Burning Test Rig	62
14	Assembly View of the Erosive-Burning Test Rig	63
15	Assembly View of the Driving Motor and the Rectangular Convergent Nozzle	65
16	Pyrotechnic Igniter System	67
17	Close-Up View of the Test Section and the Leading Edge	69

LIST OF FIGURES (continued)

Figure	Caption	Page
18	Schematic Diagram of Data-Acquisition System	75
19	Circuit Diagram for Remotely Controlled Ignition and High-Speed Photography System	77
20	Cold Flow Test Results to Check the Uniformity of the Flow Out of the Rectangular Nozzle	82
21	Measured Pressure-Time Traces in a Typical Erosive- Burning Test Firing with Exit-Nozzle Throat Diameter of 2.08 cm	83
22	Measured Pressure-Time Traces in an Erosive-Burning Test Firing with Exit-Nozzle Throat Diameter of 2.42 cm	84
23	Measured Pressure-Time Traces in an Erosive-Burning Test Firing with Exit-Nozzle Throat Diameter of 1.93 cm	85
24	Photographs Showing the Location of the Test-Propellant Surface at Various Times During a Test Firing	88
25	Least-Square Polynomial Fit to the Measured y versus t Data	89
26	Comparison of the Predicted Burning Rates with the Experimental Data at Various Pressures and Free- Stream Velocities	93
27	Comparison of the Predicted Burning Rates with the Experimental Data of Marklund and Lake	94
28	Experimental Data for Total Burning Rates at Various Pressures and Free-Stream Velocities	95
29	Experimental Data for Erosive-Burning Augmentation Factor Correlated with Pressure and Free-Stream Velocity	99
30	Calculated Distributions of Turbulent Kinetic Energy, Reynolds Stress and Velocity	104
31	Calculated Temperature Distributions for Different Free-Stream Velocities	106
32	Calculated Temperature Distributions for Different Free-Stream Velocities in the Near-Wall Region	107

LIST OF FIGURES (continued)

<u>Figure</u>	<u>Caption</u>	<u>Page</u>
33	Calculated Distributions of Oxidizer and Fuel Mass Fractions, and the Gas-Phase Heat Generation Rate in the Near-Wall Region	108
34	Effect of Free-Stream Velocity on the Location of the Peak Turbulence Intensity and the Gas-to-Solid Heat Flux	110
35	Effect of Free-Stream Velocity on the Peak Rate of Heat Generation in the Gas Phase, its Location from the Propellant Surface, and the Erosive-Burning Augmentation Factor	111
36	Calculated Turbulent Heat-Flux Distributions for Different Free-Stream Velocities	112
37	Calculated Turbulent Viscosity Distributions for Different Free-Stream Velocities	113
38	Variation of Erosive-Burning Augmentation Factor and the Propellant-Surface Temperature Along the Propellant Surface	115
39	The Effect of Normal Burning Rate on the Erosive-Burning Augmentation Factor	116
40	Computed Erosive-Burning Augmentation Factor Showing the Effect of Propellant-Surface Roughness Height at Different Free-Stream Velocities	118
C.1	Location of Nodal Points Referred to in the Finite Difference-Equations	145
D.1	Schematic Diagram Showing Mass Flow Rates in and out of Each Chamber of the Test Rig	154
D.2	Calculated Pressure-Time Traces in the Test Rig	160
D.3	Calculated Temperature-Time Traces in the Test Rig	161
D.4	Effect of the Test Chamber Exit-Nozzle Area on Pressure and Velocity in the Test Chamber	162
D.5	Effect of Test Chamber Height and Spillage on the Velocity and Pressure in the Test Chamber	163

NOMENCLATURE

Letter Symbols

a'	Pre-exponent in the strand burning-rate law
\hat{a}	Parameter defined in Equation (78)
A_b	Burning-surface area of the propellant
A_{exit}	Exit-nozzle area
A_g	Arrhenius frequency factor in gaseous reactions
A_j	Coefficients of the tridiagonal matrix
A_p	Piston area
A_s	Arrhenius frequency factor in the decomposition of the propellant surface
A_{th}	Throat area of the exit nozzle
A_{ts}	Area of the test section
A^+	Damping constant in Van Driest's hypothesis
\hat{b}	Parameter defined in Equation (79)
B	Blowing parameter defined in Equation (B.4)
B_j	Coefficients of the tridiagonal matrix
$C_1, C_2, C_3, C_4,$	
$C_{EBU}, C_{g1}, C_{g2},$	Constants in turbulence models
C_μ, C_ω	
C_d	Nozzle discharge coefficient
C_f	$2\tau_w / \rho_\infty U_\infty^2$, Skin friction coefficient
C_j	Coefficients of the tridiagonal matrix
C_p	$\sum_{k=1}^n Y_k C_{pk}$, Average heat capacity of the reacting gases
C_{pk}	Heat capacity of k^{th} species
C_s	Heat Capacity of solid propellant
C_v	Constant volume specific heat of gases

NOMENCLATURE (continued)

Letter Symbols

\hat{d}	Source term parameter defined in Equation (81)
D	Damping coefficient defined in Equation (61)
D	Diffusion coefficient in Fick's law
e	Internal energy of gases
E_{ag}, E_{as}	Activation energies in the gas-phase reaction and propellant surface decomposition
F	Symbol representing fuel gas
g	Gravitational acceleration
g_F	$\overline{Y_F'^2}$, Mean-square fluctuations of the fuel mass-fraction
G	Pressure-gradient parameter defined in Equation (B.5)
h	$\sum_{k=1}^n Y_k h_k$, Static enthalpy of gases
$\Delta h_{f,k}^\circ$	Heat of formation of k^{th} species
h_{tc}	Height of the test channel
h_{ign}	Static enthalpy of igniter gases
h_k	$\Delta h_{f,k}^\circ + \int_{T^\circ}^T C_{pk} dT$, Static enthalpy of k^{th} species
Δh	Static enthalpy difference across the boundary layer
H	$h + \frac{1}{2} u_i u_i$, Stagnation enthalpy of gases
ΔH	Stagnation enthalpy difference across the boundary layer
k	Von Karman mixing length constant
k_s	Specific reaction rate constant in the Arrhenius law
K	$\frac{1}{2} \overline{u_i' u_i'}$, Turbulent kinetic energy
K_1, K_2	Constants in the erosive burning-rate correlation, Equation (90)
L	Characteristic length in x-direction
Le	Pr/Sc , Lewis number for laminar flow
Le_t	Lewis number for turbulent flow

NOMENCLATURE (continued)

Letter Symbols

m	Mass of gases in control volume
\dot{m}_b	Mass burning rate of the propellant
\dot{m}_E, \dot{m}_I	Mass entrainment rate at the external and inner boundaries
\dot{m}_{exit}	Exit mass flow rate through the nozzle
\dot{m}_{ign}	Igniter mass flow rate
\dot{m}_{spill}	Mass flow rate through the spillage channel
M_{ts}	$\frac{U_{ts}}{\sqrt{\gamma R T_{ts}}}$, Mach number in the test section
n	Total number of species
n_e	Exponent in the erosive burning-rate correlation, Equation (90)
n'	Exponent in the strand burning-rate law
N	Total number of grid points in the numerical solution
O	Symbol representing the oxidizer gases
p	Pressure
P	Symbol representing the product gases
Pr	$C_p \mu / \lambda$, Prandtl number based on the molecular properties
Pr_t	Prandtl number for turbulent flow, defined in Equation (26)
q_i	Heat flux in i^{th} direction, defined in Equation (7)
\dot{q}_{loss}	Rate of heat loss
q_w	$(\lambda \frac{\partial T}{\partial y})_w$, Heat flux from gas to solid propellant surface
\dot{Q}_r	$\frac{1}{v_F W_F} \sum_{k=1}^n v_k W_k \Delta h_{f,k} \bar{\omega}_k$, Rate of heat generation in the gas phase
Q_s	Heat of reaction at the propellant surface defined in Equation (54)

NOMENCLATURE (continued)

Letter Symbols

\bar{Q}_s	Heat of reaction at a reference temperature defined in Equation (55)
r_b	Total burning rate of the solid propellant
r_{b_o}	$a'p^{n'}$, Strand burning rate of the solid propellant
r_e	$r_b - r_{b_o}$, Erosive burning rate of the solid propellant
R	R_u/W , Gas constant
Re_t	$\bar{\rho}K^2/\mu\epsilon$, Turbulent Reynolds number
Re_x	$\frac{\rho_{\infty} U_{\infty} x}{\mu}$, Reynolds number based on x
R_h	Roughness height
R_u	Universal gas constant
s	Shear stress parameter defined in Equation (B.1)
Sc	$\mu/\bar{\rho}D$, Schmidt number based on the molecular properties
Sc_t	Schmidt number for turbulent flow defined in Equation (25)
S_h	Heat-flux parameter defined in Equation (B.3)
S_k	Species-flux parameter defined in Equation (B.2)
t	Time
T	Temperature
T°	Reference temperature (298K)
T_f	Flame temperature
T_{ign}	Propellant-ignition temperature
T_o	Stagnation temperature
T_p	Temperature within the propellant
T_{pi}	Initial temperature of the propellant
T_{ps}	Surface temperature of the propellant

NOMENCLATURE (continued)

Letter Symbols

\bar{T}_{ps}	Reference surface temperature used to evaluate \bar{Q}_s
u	Gas velocity in x-direction
u_p	Piston velocity
u_*	$\sqrt{\frac{\tau_w}{\rho_\infty}}$, Friction Velocity
U_{ts}	Average velocity of the gases in the test section
v	Gas velocity in y-direction
\bar{V}	Gas volume
W	$(\sum_{k=1}^n Y_k/W_k)^{-1}$, Average molecular weight of gases
W_k	Molecular weight of k^{th} species
x	Coordinate along the propellant surface
x_p	Distance moved by the piston
y	Coordinate normal to the propellant surface
y^+	$\frac{\rho u_* y}{\mu}$, Nondimensional distance
Y_{FS}	Mass fraction of fuel in the solid composite propellant
Y_k	Mass fraction of k^{th} species
Y_{OS}	Mass fraction of oxidizer in the solid composite propellant
Y_{OF}	Scaler mass fraction defined in Equation (45)
ΔY_k	Change in mass fraction of k^{th} species across the boundary layer

Greek Symbols

α_s	Thermal diffusivity of the solid propellant
η	Exponent in the boundary-layer velocity profile
δ	Boundary-layer thickness
γ	C_p/C_v , Ratio of specific heats

NOMENCLATURE (continued)

Greek Symbols

ϵ	$\frac{\mu}{\rho} \overline{u'_{i,j} u'_{i,j}}$, Turbulent dissipation
λ	Thermal conductivity of the gas
λ_s	Thermal conductivity of the solid propellant
μ	Gas viscosity
μ_{eff}	$\mu + \mu_t$, Effective viscosity
μ_t	Turbulent viscosity defined in Equation (23)
$(\frac{\mu}{Pr})_{eff}$	$\equiv \frac{\mu}{Pr} + \frac{\mu_t}{Pr_t}$
$(\frac{\mu}{Sc})_{eff}$	$\equiv \frac{\mu}{Sc} + \frac{\mu_t}{Sc_t}$
v_k	Mole fraction of k^{th} species
ρ	Gas density
ρ_s	Solid propellant density
$\Delta\rho$	Change in density across the boundary layer
σ_g	Constant in the turbulence modeling of g_F equation, Equation (41)
τ	$\mu \frac{\partial u}{\partial y}$, Shear stress
τ_{ij}	Shear stress tensor defined in Equation (6)
Γ	Effective transport coefficient defined in Equation (80)
ϕ	General dependable variable representing u , Y_k , H , K , or ϵ
ψ	Stream function defined in Equation (75)
ω	Transformation coordinate defined in Equation (74)
$\dot{\omega}_k$	Rate change of species k due to chemical reactions

Subscripts

c	Edge of the Couette flow region
r	Reference condition

NOMENCLATURE (continued)

Subscripts

i, j, l	Indices representing the coordinate directions
k	Species index representing fuel (F), oxidizer (O), and product (P) gases
w	Wall (propellant surface) condition
∞	Free-stream condition
$\overline{(\quad)}$	Time-averaged quantity
$(\quad)'$	Fluctuating quantity
$(\quad)_{,i}$	Partial differentiation of the quantity in brackets with respect to x_i

CHAPTER 1

INTRODUCTION

Solid propellants are used in a variety of applications and the most important one is in rocket motors used for high-thrust booster systems. Propellants may be categorized into two groups, colloidal or homogeneous propellants and composite propellants. Currently, composite propellants, which are more energetic, are in common use. A composite solid propellant is one in which the oxidizer exists as a finely divided crystalline solid bonded in a matrix of some suitable plastic fuel. Ammonium perchlorate is the most widely used oxidizer. The burning mechanism for such a propellant is very complex. It involves a large number of chemical and physical processes including change of phase, energy transfer, and mass flow. The burning rate of a propellant primarily depends on the rate of heat transfer from the hot gaseous reaction zone to the propellant surface. Gas-to-solid heat flux causes the propellant to vaporize, and the vaporized gases react very near the surface of the propellant. The burning is additionally complicated if the propellant burns in the presence of a lateral cross-flow of high-velocity combustion gases.

1.1 Physical Description of Erosive-Burning Problem

The phrase "erosive burning" refers to the sensitivity of the solid-propellant burning rate to the velocity of the combustion gases flowing parallel to the propellant surface. The burning rate generally increases with an increase in gas velocity. A high-velocity gas-flow occurs in the central port of a propellant used in a rocket motor.

Under erosive-burning conditions, the high-velocity combustion gases in a rocket motor form a turbulent boundary layer over the propellant

surface. Within the boundary layer, complex transport processes affect the temperature and species distributions. Therefore, the presence of the high-velocity cross-flow of combustion gases can substantially affect the chemical reactions of the gas phase and the rate of heat feedback to the propellant surface. Other parameters that affect the reaction process and heat transfer rate are gas pressure, propellant composition, and fuel-to-oxidizer ratio of a propellant. The effects of the cross-flow of gases and these parameters can cause a significant change in the burning rate of a propellant. In order to predict this change, it is necessary to understand how the rate of heat transfer is affected by various gas dynamic operating conditions and other parameters mentioned above.

The ability to predict the burning rate is of prime importance in the design of a rocket motor because both the thrust level and the burning time depend on the burning rate. Erosive burning is an ever-present problem in high-performance rockets and missiles with high-thrust, short-burning, solid-propellant motors.

Recently, nozzleless rocket motors have attracted considerable interest because they offer a significant economic advantage over more conventional motors. Nozzleless rocket motors have low port-to-throat area ratios, and the gas velocity reaches sonic and supersonic speeds on the propellant surfaces, leading to the extremely serious problem of erosive burning. High-loading fractions (ratio of propellant weight to combustion chamber volume) are necessary in rocket motors for improved performance. However, with high-loading fractions, erosive burning often results in high-pressure peaks and unequal propellant-web burnout, resulting in extended heat exposure of the chamber wall. An understanding

of the erosive-burning problem and accurate predictions of the burning rate can lead to the elimination of these problems through proper modifications in the motor and/or grain design.

1.2 Previous Related Studies

In the present investigation, the erosive-burning problem of composite solid propellants is analyzed by considering a turbulent boundary layer over the propellant surface. Pertinent to this investigation are previous studies in the area of erosive burning, steady state combustion, and turbulence. These are discussed in the following sections.

1.2.1 Erosive Burning Studies

In the past the problem of erosive burning has been investigated by various methods, both theoretical and experimental (1-41). The results of these investigations have been summarized in a literature survey published by Kuo and Razdan (42), and by King (43).

Existing theories of erosive burning can be divided into three distinct classes, depending upon whether the theory is based on a) a phenomenological heat transfer theory that does not take into account chemical reactions and/or flame structure, b) a flame theory based on a description of combustion mechanisms and/or flame structure, or c) an aerothermochemical analysis which includes the consideration of heat, mass and momentum transfer in a chemically-reacting boundary layer.

Among phenomenological heat transfer theories, the Lenoir-Robillard theory (27) is quoted most often. After its development, a number of authors (29,34) have suggested certain modifications in the Lenoir-Robillard model. The essence of this model is that erosive-burning rate is proportional to the forced convection heat-transfer coefficient. The theory is analytical to the extent that use is made of a heat-transfer correlation for a transpiration-cooled surface, and empirical in the sense that the heat-transfer correlation is itself empirical. Compared

to experimental data, the theory exhibits satisfactory agreement, which may not, however, arise from theory validity but from agreement obtained by matching the burning-rate equation to the experimental data. This match is necessary to determine empirical coefficients. The utility of the Lenoir-Robillard theory is limited because the empirical coefficients must be determined experimentally for every propellant. In addition, it does not include the effect of combustion and flame structure.

The representative work on erosive burning based upon flame theory has been reported by Vandenkerckhove (28). He considered the flame structure and the mechanism of solid-phase decomposition. However, the erosive-burning models utilizing combustion mechanism or flame theory concepts are handicapped by their application to special propellants. King (40) has developed a model for the erosive burning of a composite propellant, based on the assumption that the cross-flow of gases bends the diffusion flame, thus bringing the heat release zone closer to the propellant surface. The basic assumption of this model is that the flame is located within the viscous sublayer of a turbulent boundary layer where turbulence is negligible.

An erosive-burning theory based on the boundary-layer approach was first reported in the early original work of Corner (30). He used Prandtl-Karman boundary-layer theory to describe the flow field. However, this work gave no consideration to the effect of mass injection. Tsuji (31), Razdan (32), and Schuyler and Torda (37) analyzed the problem by considering a laminar boundary layer over the propellant surface. However, in a typical erosive-burning situation the boundary layer is turbulent over most of the propellant surface. Lengellé (33) used the integral solutions of turbulent boundary-layer equations in combination

with a diffusion-flame theory to develop his model. Beddini (41) has developed a multi-equation turbulence closure model to solve the boundary-layer problem. In his analysis, however, he considered the combustion of homogeneous propellants, and also expressed the gas-phase chemical reaction rate in terms of the Arrhenius Law.

Experimentally, erosive burning has been studied by various methods. These studies can be divided into two broad categories: laboratory sample methods (4, 6, 26), and direct or indirect measurements (7-9, 11, 25). Depending on the experimental technique involved, the burning rates are average or instantaneous values. A comparison of various experimental techniques is presented in Table 1.

1.2.2 Steady State Combustion Studies

Three of the many steady-state or strand-burning (non-erosive) combustion models stand out as being sufficiently comprehensive to lead toward a better understanding of the burning mechanisms. These are the models of Summerfield (44, 45), Hermance (46), and Beckstead, Derr and Price (47). Although quite different in detail, all three models consider the final stage of gas-phase chemical reactions to be the diffusion flame. We will summarize only the Granular Diffusion Flame (GDF) model of Summerfield.

The model was originally formulated by Summerfield (44), and later improved by Steinz et. al. (45). Essential features of the two-stage GDF model are shown in Figure 1. The model is one-dimensional and assumes that the decomposition process at the propellant surface is controlled by the conductive heat feedback from a two-stage flame occurring in the gas phase. Since a composite propellant is heterogeneous, the fuel and oxidizer gases emerge unmixed from the propellant

Table 1

Comparison of Various Experimental Techniques for
Measuring Erosive-Burning Rates

Experimental Techniques	Operating Conditions	Accuracy	Remarks
<u>Laboratory Sample Methods</u>			
X-Ray	Semi-realistic	Poor	Average or Instantaneous burning rates
Break Wire	Semi-realistic	Poor	Average burning rates
Photographic	Semi-realistic	Good	Instantaneous burning rates
Microwave Interferometer	Semi-realistic	Fair	Average or Instantaneous burning rates
Probes	Semi-realistic	Poor	Average burning rates
Laser-Photodiode Servomechanism	Semi-realistic	Good	Instantaneous burning rates
Pressure Pickup	Semi-realistic	Good	Average burning rates
<u>Direct Motor Firing Methods</u>			
Interrupted Burning	Realistic	Fair	Average burning rates, numerous firings
Thermocouple Probes	Realistic	Poor	Average burning rates
Conductivity Probes	Realistic	Fair	Average burning rates
Ionization Probes	Realistic	Good	Average burning rates
<u>Indirect Motor Firing Methods</u>			
Analysis of the pressure time record	Realistic	Poor	Instantaneous burning rates

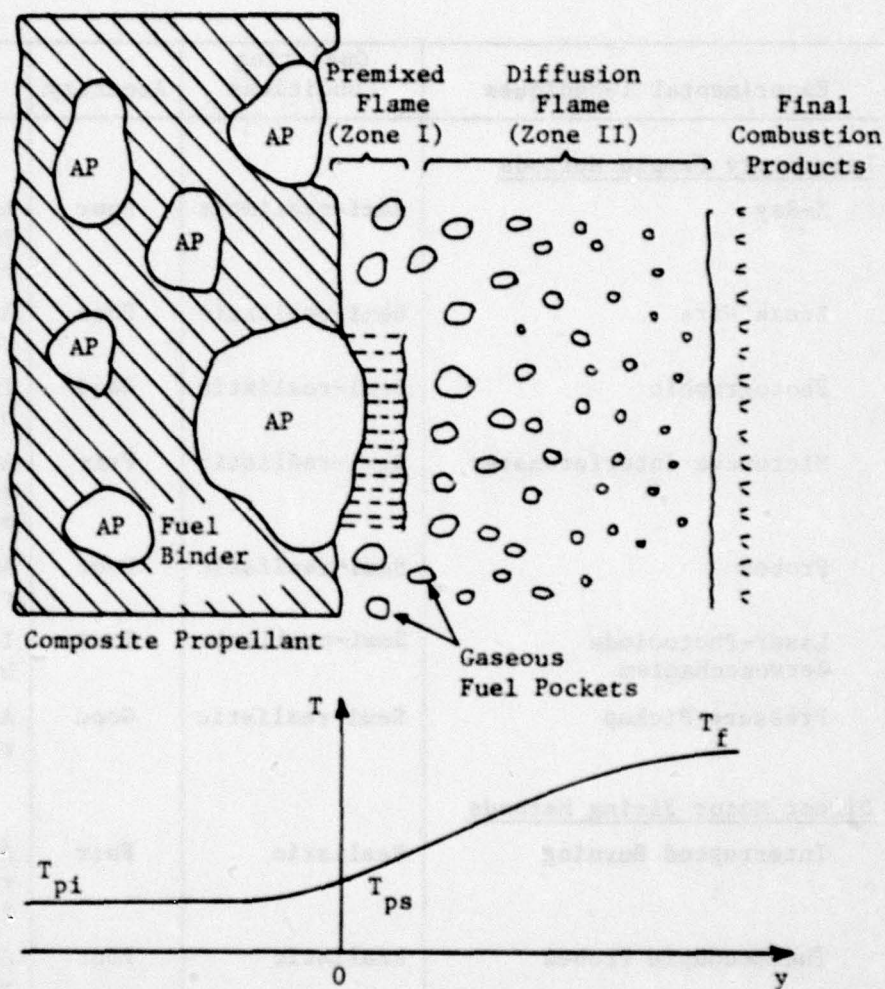


Figure 1 Two-Stage GDF Model for Ammonium Perchlorate Type Composite Solid Propellant

surface. The model presumes that fuel enters the flame zone in tiny gas pockets. Three steps in composite-propellant burning are identified: 1) endothermic zeroth-order pyrolysis of solid fuel and dissociative sublimation of ammonium perchlorate (AP) to ammonia (NH_3) and perchloric acid (HClO_4); 2) premixed exothermic reaction (zone I) between NH_3 and HClO_4 , which is assumed to occur at the surface for normal rocket pressures (pyrolyzed fuel gases in this region are considered dispersed but still unmixed); and 3) exothermic fuel-oxidant reaction (zone II) controlled either by diffusion and/or chemical reaction processes in which gaseous fuel pockets are consumed in the atmosphere of ammonia and perchloric acid. Two reaction zones, ammonia/perchloric acid (A/PA) and fuel-oxidant, are assumed to be parallel to the propellant surface. The overall rate of the fuel-oxidizer reaction is determined by rates of diffusional mixing (predominant at high pressures) and chemical reactions (predominant at low pressures). The pressure dependence of the heat feedback to the propellant surface is strongly influenced by the kinetics of the granular diffusion flame at pressures above 10 atm, even though the heat feedback from this source (20%) is considerably less than the heat contribution from A/PA reactions (80%). The propellant burning rate relationship for this model is based on integrated, steady-state, one-dimensional energy equations for the various stations in the flame zone. The proposed burning-rate equation is a function of pressure, a chemical-reaction time parameter, and a diffusional mixing-time parameter which in turn is a function of oxidizer particle size. These parameters are experimentally evaluated. Correlation of the burning-rate equation is extremely good for a variety of propellants over the pressure range of 1 to 100 atmospheres.

None of the existing solid-propellant combustion models will predict the burning rate of a composite propellant without prior knowledge of propellant combustion characteristics. In each case, various empirical parameters in the model, which are not accurately known, must be varied to match the burning rate characteristics with the experimental results.

1.2.3 Turbulent Flow Studies

As noted in Section 1.2.1, there are differing emphases in various approaches to solve the problem of erosive burning. The most realistic analysis must consider the interaction between flame zone structure and the flow field. Strand-burning combustion of AP composite propellants, as discussed above, is always associated with a diffusion flame. In the presence of a flow field, it is this diffusion flame which interacts with the cross-flow gases and, therefore, affects the heat flux to the propellant surface and the burning rate. Figures 2 and 3 explain this point clearly. The plots are based on the experimental data of references 39, 45 and 48. Erosive-burning data for various free-stream velocities was taken from King's (39) work. With known blowing rates and free-stream velocities, the corresponding friction coefficient was obtained from Simpson and Macquaid's data reported in reference 48. Figure 2 shows that the domain of turbulence is quite close to the propellant surface, and the higher the cross-flow velocity the closer the domain of turbulence. In Figure 3, the height of diffusion flame is always greater than the viscous sublayer thickness; it is clear that the diffusion flame is located in a region where the turbulence cannot be ignored.

Extensive work has been done on turbulent flows in general. However, the work in chemically reacting turbulent-flow problems is far

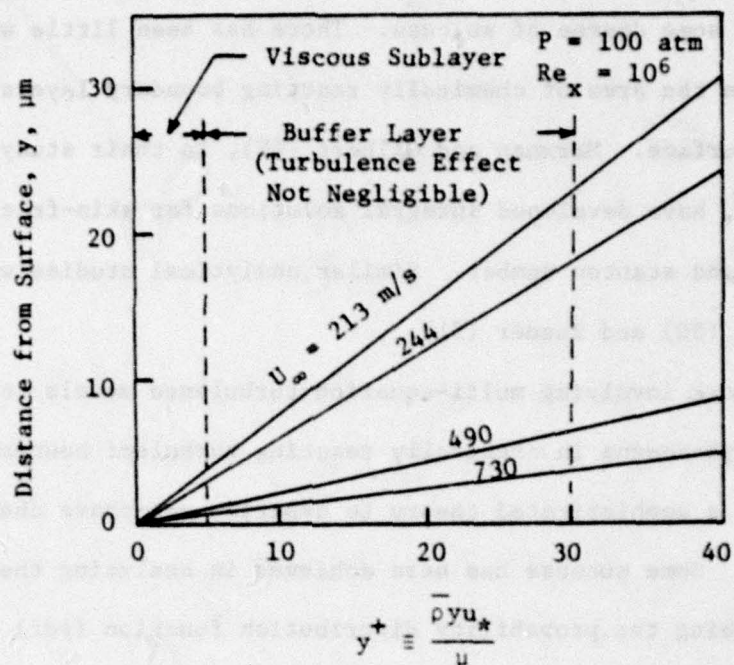


Figure 2 Effect of Free-Stream Velocity on the Domain of Turbulence Near the Propellant Surface

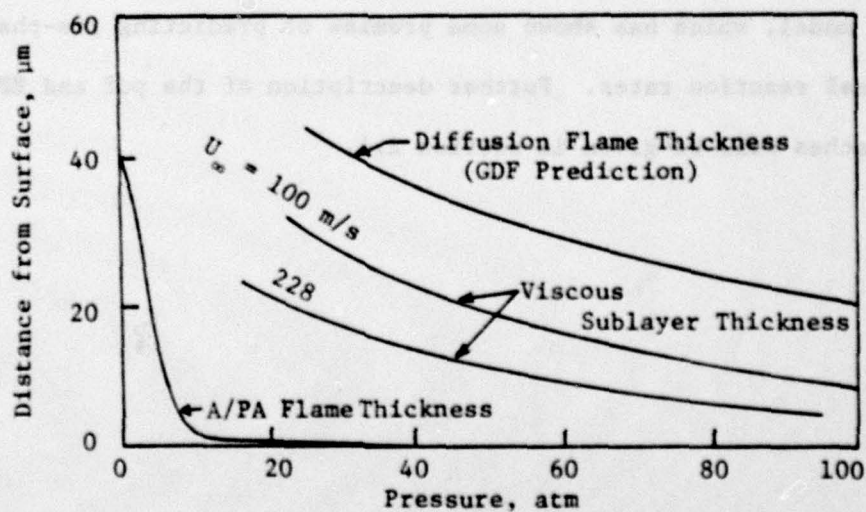
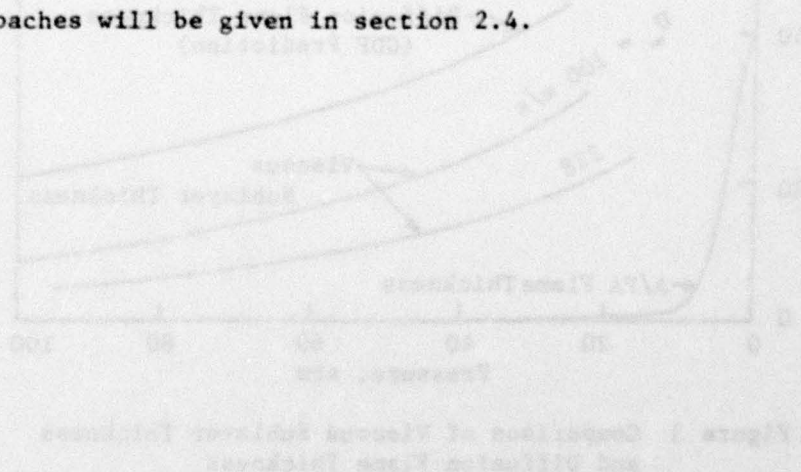


Figure 3 Comparison of Viscous Sublayer Thickness and Diffusion Flame Thickness

from complete. Only recently have these problems been treated realistically with some degree of success. There has been little work done, however, in the area of chemically reacting boundary layers on an ablating surface. Marxman and Gilbert (49), in their study of hybrid combustion, have developed integral solutions for skin-friction coefficient and Stanton number. Similar analytical studies were reported by Denison (50) and Rosner (51).

The work involving multi-equation turbulence models to describe transport phenomena in chemically reacting turbulent boundary layers has lacked a sophisticated theory to describe gas-phase chemical reactions. Some success has been achieved in analyzing the problems by prescribing the probability distribution function (pdf) for species mass fractions and temperature. The pdf modeling has been restricted mostly to free and round jets (see, for example, References 52-55). Spalding (56) has developed an alternate approach, the eddy-break-up (EBU) model, which has shown some promise of predicting gas-phase chemical reaction rates. Further description of the pdf and EBU approaches will be given in section 2.4.



1.3 Research Motivation and Objectives

There are both technological and fundamental aspects of the complicated phenomena of erosive burning. In the technological approach, one proposes simplified models and equations for estimating the burning rate; in the fundamental approach one attempts to identify a possible erosive-burning mechanism and to establish a theory for local erosion phenomena. The previous studies indicate that although technological studies are progressing, all are handicapped by their application to special propellants. There is also a need for experiments to evaluate certain empirical constants. In the past, little work has been done on the fundamental aspect of the problem of erosive burning. With this status in mind, the present research program was undertaken to investigate the erosive-burning problem, both theoretically and experimentally. Objectives of this study are:

1. To formulate a theoretical model based on an aerothermochemical analysis of the erosive-burning problem of composite solid propellants. The analysis considers the heat, mass and momentum transfer in a chemically reacting turbulent boundary layer.
 2. To study the effects of gas velocity, pressure, and propellant physiochemical characteristics on the erosive-burning rate of a propellant.
 3. To verify the theoretical results experimentally by conducting a series of erosive-burning test firings under various experimental conditions for gas velocity and chamber pressure.
 4. To identify a possible erosive-burning mechanism of composite solid propellants.
- 31

Section 2 of this document describes the theoretical model leading to the development of governing equations, turbulence closure models, gas-phase chemical reaction model, and boundary conditions. The numerical method of solving the theoretical model, the development of the computer code, and some boundary-layer solutions are presented in Section 3. In section 4, experimental work related to burning-rate measuring techniques, test-rig design, and instrumentation are discussed. Experimental and theoretical results and their comparison are discussed in Section 5. A summary and the conclusions of this study are given in Section 6.

CHAPTER 2

THEORETICAL MODELING

2.1 Description of the Physical Model

The physical model considered in the theoretical analysis consists of a flat plate with a fixed leading edge as shown in Figures 4a and 4b. In Figure 4a, a test-propellant sample is fed through the flat plate at a rate equal to the burning rate of the propellant, thus maintaining the surface of the propellant at a fixed level. Figure 4b shows a two-dimensional propellant slab glued to the leading edge element. In both cases, the propellant sample is ignited by the hot combustion gas in the free stream, which forms a turbulent boundary layer (after a very short transition distance, usually 0.5 cm) over the burning surface of the propellant. In Figure 4b, the surface changes its position as the propellant burns down; however, the characteristic time of the boundary layer is very small, requiring about 10^{-4} sec. (33) to adjust quickly to any change at the boundaries. Therefore, the current analysis will be applicable to both types of situations illustrated in Figures 4a and 4b.

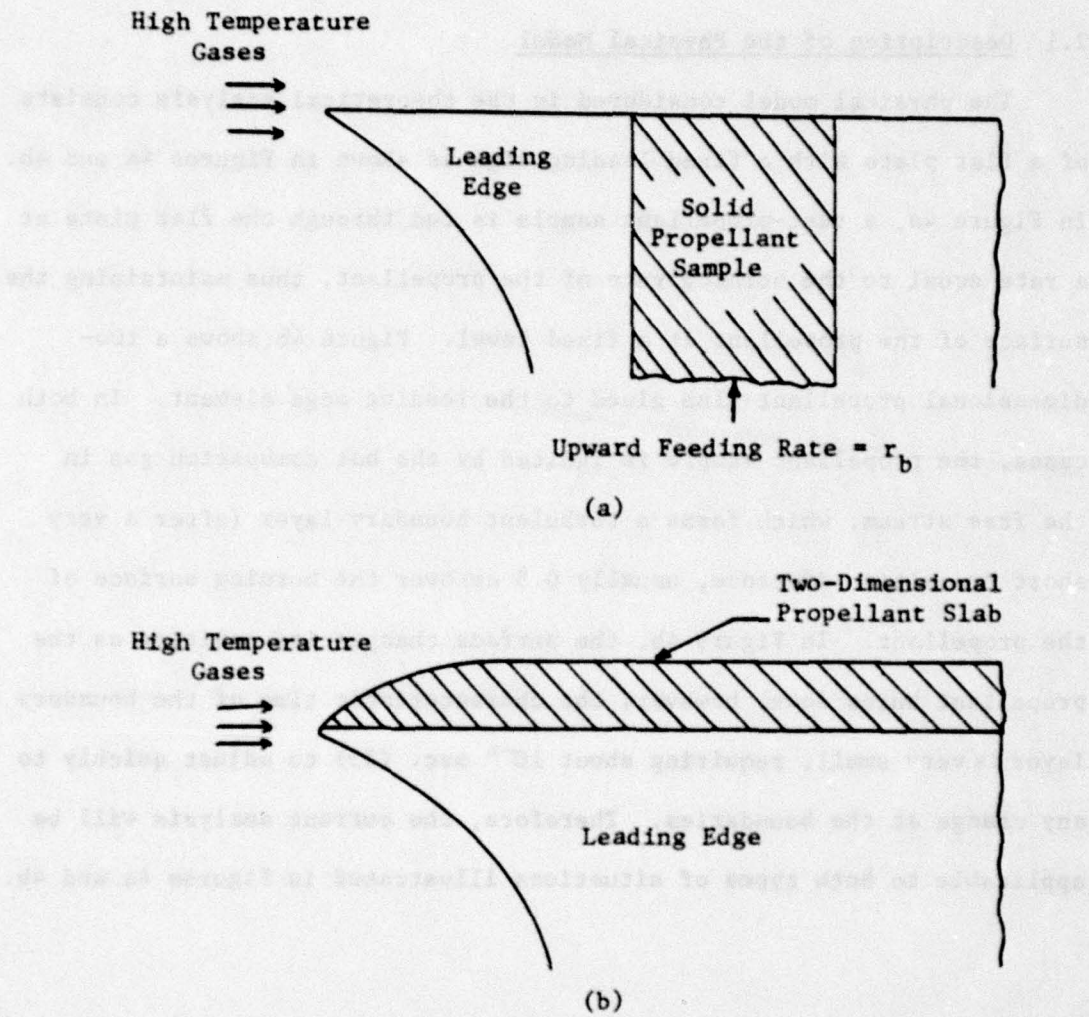


Figure 4 Physical Model Considered in the Theoretical Analysis

2.2 Conservation Equations

To formulate the theoretical model, we begin with the general conservation equations for a reacting compressible fluid flow. These equations are well known and several authors have described their derivation (see, for example, Reference 57). The pertinent details will be presented here, using subscript notations.

The usual assumptions in the derivation of conservation equations are:

- (1) No body force
- (2) No radiation heat transfer
- (3) No diffusion resulting from temperature gradient (Soret effect), no heat flux caused by species gradient diffusion (Dufour effect), and no pressure gradient diffusion
- (4) Stokesian fluid
- (5) Fick's law for diffusion velocity is applicable
- (6) Equal binary diffusion coefficients; this assumption is necessary for Fick's law to be valid.

The conservation equations are:

Mass conservation:

$$\frac{\partial \rho}{\partial t} + (\rho u_i)_{,i} = 0 \quad (1)$$

Momentum conservation:

$$\frac{\partial}{\partial t} (\rho u_i) + (\rho u_i u_j)_{,j} = -p_{,i} + \tau_{ij,j} \quad (2)$$

Species conservation:

$$\frac{\partial}{\partial t} (\rho Y_k) + (\rho Y_k u_i)_{,i} = (\rho D Y_{k,i})_{,i} + \dot{\omega}_k, \quad k = 1, 2, \dots, n \quad (3)$$

Energy conservation:

$$\frac{\partial}{\partial t} (\rho H) + (\rho u_i H)_{,i} - \frac{\partial p}{\partial t} = -q_{i,i} + (u_i \tau_{ij})_{,j} \quad (4)$$

where:

$$H = h + \frac{1}{2} u_i u_i, \quad h = \sum_{k=1}^n Y_k h_k, \quad h_k = \Delta h_{f,k}^o + \int_{T^o}^T C_{p,k} dT \quad (5)$$

$$\tau_{ij} = \mu (u_{i,j} + u_{j,i} - \frac{2}{3} \delta_{ij} u_{l,l}), \quad \delta_{ij} = \begin{cases} 1 & \text{for } i = j \\ 0 & \text{for } i \neq j \end{cases} \quad (6)$$

$$q_i = -\lambda \frac{\partial T}{\partial x_i} - \sum_{k=1}^n \rho D_{h,k} Y_{k,i} \quad (7)$$

Equation of state:

$$p = \rho R_u T / W \quad (8)$$

We now assume that the instantaneous variable can be replaced by the sum of its mean and fluctuating components.

$$\phi = \bar{\phi} + \phi' \quad (9)$$

This is the well-known Reynolds decomposition procedure. Here, ϕ represents the instantaneous value of velocity, enthalpy, species mass fractions, etc. The bar denotes the mean or average value taken over a time period which is sufficiently long compared to the time scale of the turbulent fluctuations. The prime denotes the fluctuating quantity. The averaging process implies that

$$\bar{\phi} \equiv \text{Limit}_{t \rightarrow \infty} \frac{1}{t} \int_0^t \phi dt, \quad \overline{\phi'} = 0, \quad \overline{\bar{\phi}} = \bar{\phi} \quad (10)$$

After applying Equations (9) and (10) to Equations (1) through (4), each equation is time averaged, and the following governing equations for the mean quantities are derived.

Continuity Equation:

$$\frac{\partial \bar{\rho}}{\partial t} + (\bar{\rho} \bar{u}_1 + \overline{\rho' u'_1})_{,1} = 0 \quad (11)$$

Momentum Equation:

$$\begin{aligned} \bar{\rho} \frac{\partial \bar{u}_1}{\partial t} + \frac{\partial}{\partial t} (\overline{\rho' u'_1}) + (\bar{\rho} \bar{u}_j + \overline{\rho' u'_j}) \bar{u}_{1,j} = - \bar{p}_{,1} \\ + (\bar{\tau}_{1j} - \bar{\rho} \overline{u'_1 u'_j} - \bar{u}_j \overline{\rho' u'_1} - \overline{\rho' u'_1 u'_j})_{,j} \end{aligned} \quad (12)$$

Species Equation:

$$\begin{aligned} \bar{\rho} \frac{\partial \bar{Y}_k}{\partial t} + \frac{\partial}{\partial t} (\overline{\rho' Y'_k}) + (\bar{\rho} \bar{u}_1 + \overline{\rho' u'_1}) \bar{Y}_{k,1} = (\bar{\rho} D \bar{Y}_{k,1} \\ + D \overline{\rho' Y'_k})_{,1} - (\overline{\rho u'_1 Y'_k})_{,1} + \bar{\omega}_k \end{aligned} \quad (13)$$

Energy Equation:

$$\begin{aligned} \bar{\rho} \frac{\partial \bar{H}}{\partial t} + \frac{\partial}{\partial t} (\overline{\rho' H'}) + (\bar{\rho} \bar{u}_1 + \overline{\rho' u'_1}) \bar{H}_{,1} - \frac{\partial \bar{p}}{\partial t} \\ = \frac{\partial}{\partial x_j} \left[\frac{\lambda}{C_p} (\bar{H}_{,j} - \frac{1}{2} (\bar{u}_1 \bar{u}_1)_{,j} - \frac{1}{2} (\overline{u'_1 u'_1})_{,j}) \right. \\ \left. - (\overline{\rho u'_j H'}) + \frac{\mu}{Pr} (Le - 1) \sum_{k=1}^n \{ \bar{h}_k \bar{Y}_{k,j} + \overline{h'_k Y'_k} \} \right. \\ \left. + \bar{u}_1 \bar{\tau}_{1j} + \overline{u'_1 \tau'_{1j}} \right] \end{aligned} \quad (14)$$

Another approach for averaging the instantaneous conservation equations, known as Favre averaging (58), has been used by a number of researchers. The procedure is to split the instantaneous quantities into mass-averaged quantities and fluctuating quantities (e.g., any variable $\phi = \tilde{\phi} + \phi''$ where $\tilde{\phi} \equiv \frac{\overline{\phi\rho}}{\bar{\rho}}$, $\phi'' = \phi' - \frac{\rho'\phi'}{\bar{\rho}}$, $\overline{\phi''} \neq 0$ and $\overline{\rho\phi''}=0$). This approach eliminates the explicit appearance of terms involving density correlations in the governing equations. The use of Favre averaging is certainly much simpler as far as computations are concerned. However, using the same models for Favre correlations as for normal correlations (this is the practice followed by those using Favre averaging) may not be physically plausible, as argued by Gosman et. al. (53). Furthermore, the governing equations for the current model can easily be recast into the Favre-averaged equations.

The following assumptions are now introduced into Equations (11) through (14):

- (1) Flow is steady
- (2) Mean flow is two-dimensional
- (3) Molecular Lewis number, Le , and turbulent Lewis number, Le_t , are both unity.
- (4) For the Mach number range of order unity,

$$\overline{\mu \frac{\partial u'}{\partial y}} < < \bar{\mu} \frac{\partial \bar{u}}{\partial y}, \text{ and } \overline{\rho' u' v'} < < \bar{\rho} \bar{u}' v'$$

According to Laufer (59), who based his conclusion on the experimental results of Kistler (60), the density fluctuations have a kinematic rather than a dynamic effect on the turbulence.

- (5) There is no reaction generated turbulence. Wooldridge and Muzzy (61) and Eschenroeder (62) suggest that combustion

affects the intensity of turbulent fluctuations. Kulgein (63), on the other hand, suggests that there is no combustion induced turbulence.

Using these assumptions and following an order-of-magnitude analysis (see Appendix A), dominant terms in Equations (11) through (14) are retained to give the final form of the two-dimensional steady-state equations for a reactive turbulent compressible flow.

Continuity Equation:

$$\frac{\partial}{\partial x} (\bar{\rho} \bar{u}) + \frac{\partial}{\partial y} (\bar{\rho} \bar{v}) = 0 \quad (15)$$

where

$$\bar{\rho} \bar{v} = \bar{\rho} \bar{v} + \overline{\rho' v'} \quad (16)$$

Momentum Equation:

$$\bar{\rho} \bar{u} \frac{\partial \bar{u}}{\partial x} + \bar{\rho} \bar{v} \frac{\partial \bar{u}}{\partial y} = - \frac{d\bar{p}}{dx} + \frac{\partial}{\partial y} \left[\mu \frac{\partial \bar{u}}{\partial y} - \overline{\rho u' v'} \right] \quad (17)$$

Species Equation:

$$\bar{\rho} \bar{u} \frac{\partial \bar{Y}_k}{\partial x} + \bar{\rho} \bar{v} \frac{\partial \bar{Y}_k}{\partial y} = \frac{\partial}{\partial y} \left[\bar{\rho} D \frac{\partial \bar{Y}_k}{\partial y} - (\rho v) \bar{Y}'_k \right] + \bar{\omega}_k \quad (18)$$

Energy Equation:

$$\begin{aligned} \bar{\rho} \bar{u} \frac{\partial \bar{H}}{\partial x} + \bar{\rho} \bar{v} \frac{\partial \bar{H}}{\partial y} = \frac{\partial}{\partial y} \left[\frac{\lambda}{C_p} \frac{\partial \bar{H}}{\partial y} - \bar{\rho} \bar{u} \overline{u' v'} + \mu \left(1 - \frac{1}{Pr} \right) \frac{\partial \bar{u}^2 / 2}{\partial y} \right. \\ \left. - \sum_k \{ \bar{Y}_k \overline{(\rho v) h'_k} + \bar{h}_k \overline{(\rho v) Y'_k} \} \right] \quad (19) \end{aligned}$$

2.3 Turbulence Closure Models

In Equations (15) through (19), a number of unknown correlations have been introduced. These correlations are: Reynolds stress, $\overline{u'v'}$, turbulent mass flux, $\overline{(\rho v)'Y'_k}$, and turbulent heat flux, $\overline{(\rho v)'h'_k}$. In order to close the system of equations, these correlations must be modeled. The correlation between density and velocity, $\overline{\rho'v'}$, need not be modeled as it appears in each equation along with $\overline{\rho'}$, and these two terms can be combined by introducing a new variable $\overline{v^0}$, defined in Equation (16). A "two-equation" turbulence model (64), in which the turbulence is assumed to be characterized by its kinetic energy, K , and its dissipation rate, ϵ , is employed. Therefore, in addition to the governing equations, Equations (15) through (19), two additional equations for K and ϵ are needed.

Turbulent Kinetic Energy Equation:

We define turbulent kinetic energy, K , as $\frac{1}{2} \overline{u'_i u'_i}$. The K equation is derived as follows: Subtract momentum equation for mean quantities, Equation (12), from the momentum equation for instantaneous quantities, Equation (2), and multiply by u'_l . To the resulting equation, add a similar equation with indices i and l interchanged. Then, time average the whole equation and set l equal to i . The resulting equation in steady state form is:

$$\begin{aligned}
 (\overline{\rho} \overline{u'_j} + \overline{\rho' u'_j}) K_{,j} = & - (\overline{\rho} \overline{u'_i u'_j} + \overline{u'_j} \overline{\rho' u'_i} + \overline{\rho' u'_i u'_j}) \overline{u'_{i,j}} \\
 & + \overline{p' u'_{i,i}} - (\overline{\rho} \overline{K' u'_j} - K \overline{\rho' u'_j} + \overline{u'_j} \overline{\rho' K'} + \overline{\rho' u'_j K'}) \\
 & + \overline{p' u'_j}_{,j} + \overline{u'_i \tau'_{ij,j}}
 \end{aligned} \tag{20}$$

Turbulent Dissipation Equation:

We define turbulent dissipation, ϵ , as $\frac{\mu}{\rho} \overline{u'_{1,l} u'_{1,l}}$. The ϵ equation is derived as follows: Subtract momentum equation for mean quantities, Equation (12), from the momentum equation for instantaneous quantities, Equation (2), and differentiate the resulting equation with respect to x_l . Multiply by $u'_{1,l}$ and time average the whole equation. The result in steady state form is as follows:

$$\begin{aligned}
 \bar{u}_j \left(\frac{\bar{\rho} \epsilon}{\bar{\mu}} \right)_{,j} = & -2 \bar{u}_{1,j} (\overline{u'_{1,l} u'_{j,l}} + \overline{u'_{l,j} u'_{l,i}}) \\
 & - \left(\bar{\rho} \frac{\overline{u'_{j,l} \epsilon'}}{\bar{\mu}} \right)_{,j} - 2 \overline{u'_{1,l} u'_{j,l} u'_{1,j}} \\
 & - 2 \bar{u}_{1,jl} \overline{u'_{1,l} u'_{j,l}} + \frac{2}{\bar{\rho}} \overline{u'_{1,l} \tau'_{1j,jl}} - \frac{2}{\bar{\rho}} (\overline{p'_{,l} u'_{1,l}})_{,i} \\
 & - \frac{2}{\bar{\rho}} \left[-\frac{\bar{\rho}^2}{2\bar{\mu}} \overline{\epsilon' u'_{j,j}} - \overline{p'_{,l} u'_{1,l}} + \bar{\rho}_{,l} \bar{u}_j \overline{u'_{1,l} u'_{1,j}} \right. \\
 & + \bar{\rho}_{,l} \bar{u}_{1,j} \overline{u'_{1,l} u'_{j,l}} + \bar{\rho}_{,l} \overline{u'_{1,l} u'_{j,l} u'_{1,j}} \\
 & + (\bar{u}_j \bar{u}_{1,j})_{,l} \overline{u'_{1,l} \rho'} + \bar{u}_j \bar{u}_{1,j} \overline{u'_{1,l} \rho'_{,l}} \\
 & + \overline{u'_{1,l} u'_{1,j} (\rho' u'_{j,l})} + \overline{\rho' u'_{j,l} \left(\frac{\bar{\rho} \epsilon'}{\bar{\mu}} \right)} + \bar{u}_{1,jl} \overline{u'_{1,l} u'_{j,l} \rho'} \\
 & + \bar{u}_{1,j} \overline{u'_{1,l} (\rho' u'_{j,l})} + \bar{u}_j \overline{u'_{1,l} (\rho' u'_{1,j})} \\
 & \left. + \bar{u}_{j,l} \overline{u'_{1,l} u'_{1,j} \rho'} \right] \quad (21)
 \end{aligned}$$

Except for the terms in square brackets, Equation (21) is the same as that in a uniform property flow situation. The part of Equation (21)

in brackets results as a consequence of density fluctuations.

Correlations such as $\overline{(\rho v) Y_k}$ and $\overline{(\rho v) h_k}$ are usually modeled in terms of known variables and some unknown constants. These constants are assumed to be universal, and, in general, are evaluated by matching the theoretical and experimental results. Conservation equations can be developed for these correlations; however, doing so introduces still higher order correlations, and eventually these higher order correlations must also be modeled. In the present approach, excess complexity is avoided in favor of simpler and faster-to-execute formulation. It is understood, also, that chemical reactions in the diffusion flame play an important role in erosive burning. Therefore, it would be more meaningful to describe the effects of turbulence on the chemical reactions in the closure consideration, rather than solve numerous conservation equations for higher-order turbulence correlations. The following closure models and assumptions for various correlations are introduced:

1. Reynolds-stress term, $\overline{u'v'}$, is modeled with the aid of the eddy-viscosity concept (64):

$$-\overline{\rho u'v'} = \mu_t \frac{\partial \bar{u}}{\partial y} \quad (22)$$

$$\mu_t = C_\mu \frac{\bar{\rho} K^2}{\epsilon} \quad (23)$$

where C_μ is a constant. The models of Equations (22) and (23) have been used widely in non-reacting as well as reacting flows with considerable success (52, 53, 55, 56, 64).

2. Turbulent diffusion term in Equation (20) is expressed, following uniform-property-flow practice, as:

$$\begin{aligned}
& - \frac{\partial}{\partial x_j} (\bar{\rho} \overline{K' u'_j} - K \bar{\rho' u'_j} + \bar{u}_j \bar{\rho' K'} + \bar{\rho' u'_j K'} + \bar{p' u'_j}) \\
& = \frac{\partial}{\partial x_j} \left(\frac{\mu_t}{C_1} \frac{\partial K}{\partial x_j} \right) \quad (24)
\end{aligned}$$

3. Mass transfer by turbulent diffusion, $\overline{(\rho v)' Y'_k}$, in Equation (18), and heat transfer by turbulent diffusion, $\overline{(\rho v)' h'_k}$, in Equation (19), are modeled by using Reynold's analogy:

$$\overline{(\rho v)' Y'_k} = \frac{\mu_t}{Sc_t} \frac{\partial \bar{Y}_k}{\partial y} \quad (25)$$

$$\overline{(\rho v)' h'_k} = \frac{\mu_t}{Pr_t} \frac{\partial \bar{h}_k}{\partial y} \quad (26)$$

4. Triple correlation term, $\overline{\rho' u'_i u'_j}$, and the correlation $\overline{p' u'_{i,i}}$ in Equation (20) are assumed negligible. The same assumption has been used in many reacting flow problems by a number of authors (52, 53, 55, 56).
5. The exact form of the ϵ equation for a reacting flow, as represented by Equation (21), is very difficult to model because of the appearance of correlations involving fluctuating velocity gradients and density fluctuations. We use the form of ϵ equation (Equation 32) as applicable to uniform property flow (64). We could modify it by retaining full expression for production of K, which comprises the first three terms, on the right-hand side of Equation (20), as was done by Gosman et. al. (53). They introduced Boussinesq approximation for $\overline{\rho' u'_i}$ in Equation (20). However, their study found that the effect of this modification was negligible on

the solution of mean variables.

It may be mentioned that the modeling of K and ϵ equations is based on the assumption of high local Reynolds number, $Re_t \equiv \bar{\rho} K^2 / \mu \epsilon$; however, this assumption breaks down within the viscous sublayer adjacent to a wall. The treatment of near-wall region is discussed in section 2.6.

We use the models mentioned above in Equations (17) through (20), and perform order-of-magnitude analysis of K equation (see Appendix A) to give the final set of two-dimensional boundary-layer equations:

Continuity Equation:

$$\frac{\partial}{\partial x} (\bar{\rho} \bar{u}) + \frac{\partial}{\partial y} (\bar{\rho} \bar{v}) = 0 \quad (27)$$

Momentum Equation:

$$\bar{\rho} \bar{u} \frac{\partial \bar{u}}{\partial x} + \bar{\rho} \bar{v} \frac{\partial \bar{u}}{\partial y} = \frac{\partial}{\partial y} [\mu_{\text{eff}} \frac{\partial \bar{u}}{\partial y}] - \frac{d\bar{p}}{dx} \quad (28)$$

Species Equation:

$$\bar{\rho} \bar{u} \frac{\partial \bar{Y}_k}{\partial x} + \bar{\rho} \bar{v} \frac{\partial \bar{Y}_k}{\partial y} = \frac{\partial}{\partial y} [(\frac{\mu}{Sc})_{\text{eff}} \frac{\partial \bar{Y}_k}{\partial y}] + \bar{\omega}_k \quad (29)$$

Energy Equation:

$$\bar{\rho} \bar{u} \frac{\partial \bar{H}}{\partial x} + \bar{\rho} \bar{v} \frac{\partial \bar{H}}{\partial y} = \frac{\partial}{\partial y} [(\frac{\mu}{Pr})_{\text{eff}} \frac{\partial \bar{H}}{\partial y}] + (\mu_{\text{eff}} - (\frac{\mu}{Pr})_{\text{eff}}) \frac{\partial \bar{u}^2/2}{\partial y} \quad (30)$$

Turbulent Kinetic Energy Equation:

$$\bar{\rho} \bar{u} \frac{\partial \bar{K}}{\partial x} + \bar{\rho} \bar{v} \frac{\partial \bar{K}}{\partial y} = \frac{\partial}{\partial y} [(\mu + \frac{\mu_t}{C_1}) \frac{\partial \bar{K}}{\partial y}] + \mu_t (\frac{\partial \bar{u}}{\partial y})^2 - \bar{\rho} \epsilon \quad (31)$$

Turbulent Dissipation Equation:

$$\bar{\rho} \bar{u} \frac{\partial \epsilon}{\partial x} + \bar{\rho} \bar{v} \frac{\partial \epsilon}{\partial y} = \frac{\partial}{\partial y} [(\mu + \frac{\mu_t}{C_2}) \frac{\partial \epsilon}{\partial y}] + C_3 [\mu_t (\frac{\partial \bar{u}}{\partial y})^2] \frac{\epsilon}{K} - C_4 \bar{\rho} \frac{\epsilon^2}{K} \quad (32)$$

Equation of State:

$$\bar{p} = \bar{\rho} R_u \bar{T} / W \quad (33)$$

In addition to the conservation equations for the gas phase, Equations (27) through (33), heat conduction equation in the solid phase is needed to relate the heat flux to the solid propellant in terms of its surface temperature and the initial propellant temperature.

Heat Conduction Equation in the Solid Phase:

It is assumed that heat conduction into the solid propellant is dominant in a direction normal to the burning surface. In a coordinate system attached to the burning surface, the temperature distribution in the solid propellant at a given x location along the surface is governed by:

$$\lambda_s \frac{\partial^2 T_p}{\partial y^2} = \rho_s C_s r_b \frac{\partial T_p}{\partial y}, \quad -\infty < y \leq 0^- \quad (34)$$

Integrating Equation (34) and applying the boundary conditions for the solid phase

$$T_p|_{y \rightarrow -\infty} = T_{pi} \quad (\text{initial propellant temperature}) \quad (35)$$

$$\frac{\partial T_p}{\partial y} \bigg|_{y \rightarrow -\infty} = 0 \quad (36)$$

we get an expression for the heat flux to solid propellant

$$\lambda_s \frac{\partial T_p}{\partial y} \bigg|_{0^-} = \rho_s C_s r_b (T_{ps} - T_{pi}) \quad (37)$$

2.4 Modeling of Gas-Phase Chemical Reactions

The set of equations (27) through (33), with appropriate boundary conditions, can be solved provided $\bar{\omega}_k$ in Equation (29) is known. When a composite solid propellant burns, solid fuel and oxidizer particles transform into gases. The gases may react in several steps. However, in the present work, the following single-step chemical reaction is assumed:



where O and F represent the oxidizer and the fuel gases respectively, and P represents the product gases. How the oxidizer and fuel gases are identified for the combustion of ammonium perchlorate based propellants, is discussed in section 5.2.

A possible expression for the instantaneous global reaction rate is:

$$\dot{\omega}_k = -W_k k_s \prod_{k=1}^n \left(\frac{\rho Y_k}{W_k} \right)^{\nu_k} \quad (39)$$

where $k = O, F$ and the specific reaction rate constant, k_s , is given by the Arrhenius law: $k_s = A_g \exp \left(-\frac{E_{ag}}{R_u T} \right)$. The time-averaging of Equation (39) represents one of the central difficulties of combustion modeling. One can choose to replace the exponential term by its series expansion, thereby introducing correlations such as $\overline{Y_O Y_F}$, $\overline{Y_O T}$, $\overline{Y_F T}$, $\overline{T^2}$, etc. Additional conservation equations must be solved for these correlations; this procedure, however, reduces the economy significantly.

Many researchers (52, 53, 55) have used, with some success, the concept of probability density function (pdf) to describe the mass

fraction distribution in chemically reacting flow problems. Such a method has been used mostly in turbulent jets in which oxidizer and fuel streams mix and react in a diffusion flame, or in a premixed fuel-oxidizer stream reacting in a turbulent jet. The situation in the erosive-burning problem is quite different; viz., fuel and oxidizer gases from burning propellant enter transversely into the turbulent boundary layer formed over the propellant surface. After reviewing existing literature of the pdf method and its possible use in the erosive-burning problem, it was concluded that the application of this method would not be adequate.

One other approach, first proposed by Spalding (56), is the eddy-break-up (EBU) model. In this model, gases in a turbulent premixed flame, at high Reynolds numbers, are considered as lumps or eddies of unburned gas and fully burned gas. Spalding assumed that the rate of burning depended upon the rate at which fragments of unburned gas (eddies) were broken into still smaller fragments by the action of turbulence. This rate was assumed to be proportional to the rate of decay of turbulence energy. Spalding's initial version of the EBU model was based on the mixing-length hypothesis (56), and Mason and Spalding (65) introduced the EBU model based on a two-equation model of turbulence to solve the problem of confined turbulent flames.

The idea of the EBU concept can be used to model the gas-phase reaction rate for the erosive-burning problem in which gaseous fuel issues as pockets (eddies) from the burning surface of a composite solid propellant according to GDF theory (45). Furthermore, it is reasonable to assume that high lateral shear in the boundary layer aids the formation of these fuel eddies.

We might, then, follow the EBU concept as well as the arguments of Lockwood (66): in a diffusion controlled reaction, the rate of consumption of fuel is proportional to the rate of dissipation of the fuel-containing eddies, as characterized by the rate of diminution of the energy of the fluctuations, $g_F \equiv \overline{Y_F'^2}$. This rate can be equated to the rate of supply of energy from the large scale motion of turbulence, which can be taken as proportional to the quantity of energy involved and to the reciprocal of the eddy time scale characterized by ϵ/K .

$$\overline{\dot{\omega}}_F = -C_{EBU} \overline{\rho} \sqrt{g_F} \frac{\epsilon}{K} \quad (40)$$

This equation can be used, provided g_F is known. The conservation equation of g_F can be written as (see Reference 64):

$$\overline{\rho} \overline{u} \frac{\partial g_F}{\partial x} + \overline{\rho} \overline{v} \frac{\partial g_F}{\partial y} = \frac{\partial}{\partial y} \left(\frac{\mu_t}{\sigma_g} \frac{\partial g_F}{\partial y} \right) + C_{g1} \mu_t \left(\frac{\partial \overline{Y}_F}{\partial y} \right)^2 - C_{g2} \overline{\rho} \frac{\epsilon}{K} g_F \quad (41)$$

Equation (41) along with Equation (40) can be used to determine reaction rate of fuel gas. However, we can simplify the analysis by assuming the production and dissipation terms (last two terms on the right hand side) of Equation (41) to be dominant (see Reference 64). This assumption is particularly valid at high Reynolds numbers in the near-wall region, which in the present problem is where most of the chemical reactions take place. Therefore, when equating the production and dissipation terms of Equation (41), we arrive at

$$g_F \approx \frac{\mu_t}{\overline{\rho}} \frac{K}{\epsilon} \left(\frac{\partial \overline{Y}_F}{\partial y} \right)^2 \quad (42)$$

From Equations (40), (42) and (23), we get

$$\overline{\dot{\omega}}_F = -C_{\omega} \overline{\rho} \sqrt{K} \left| \frac{\partial \overline{Y}_F}{\partial y} \right| \quad (43)$$

where C_ω is a constant. In the current theoretical analysis, it is assumed that the chemical kinetics is very fast and that the reaction rate is diffusion limited, since the gaseous reactions in propellant combustion take place under high pressures (a favorable condition for this assumption). It may be noted that the gas phase in the combustion of a composite solid propellant is heterogeneous because of the existence of small fuel pockets dispersed in an atmosphere of oxidizer gases. The present theoretical model, however, considers the homogeneous gas phase in the sense that the species mass fractions in Equation (29) are defined as the local average values over a period of time which is much longer than the characteristic time of turbulence. In order to solve a heterogeneous problem, one would have to specify the pocket-size distribution of the fuel gases, which is an unknown. Even though the treatment of the gas phase is homogeneous, the process of chemical reactions in the gas phase is still diffusion controlled. Therefore, Equation (43) (which is based on the diffusion controlled process) is used along with Equation (29) to solve species distribution in the gas phase. No separate reaction rate formula is necessary for oxidizer species. With the assumption of Equation (38),

$$\bar{\omega}_O = \frac{v_O W_O}{v_F W_F} \bar{\omega}_F \quad (44)$$

we can now introduce a new variable \bar{Y}_{OF} , defined as

$$\bar{Y}_{OF} \equiv \bar{Y}_O - \frac{v_O W_O}{v_F W_F} \bar{Y}_F \quad (45)$$

The conservation equation for \bar{Y}_{OF} is obtained by subtracting $\frac{v_O W_O}{v_F W_F}$ times the species mass fraction equation for fuel, $k = F$ in Equation (29), from the species mass fraction equation for oxidizer, $k = O$ in Equation

(29), and using Equations (44) and (45). The result is

$$\bar{\rho} \bar{u} \frac{\partial \bar{Y}_{OF}}{\partial x} + \bar{\rho} \bar{v} \frac{\partial \bar{Y}_{OF}}{\partial y} = \frac{\partial}{\partial y} \left[\left(\frac{\mu}{Sc} \right)_{eff} \frac{\partial \bar{Y}_{OF}}{\partial y} \right] \quad (46)$$

The choice of the variable \bar{Y}_{OF} eliminates the nonlinear source terms in Equation (46). No separate conservation equation for \bar{Y}_p is needed because by definition of mass fraction $\sum_{k=1}^n Y_k = 1$. Therefore

$$\bar{Y}_p = 1 - \bar{Y}_O - \bar{Y}_F \quad (47)$$

2.5 Burning Rate Equation

Burning rate of a solid propellant is a function of the surface temperature, and can be expressed by the Arrhenius law of surface pyrolysis

$$r_b = A_s \exp \left(- \frac{E_{as}}{R_u T_{ps}} \right) \quad (48)$$

where A_s is the pre-exponential factor and E_{as} is the activation energy of the solid propellant. Surface temperature, T_{ps} , is the unknown. Because of the coupling nature of conditions of the propellant surface, and the fact that the process must be self-sustaining, the case of a constant surface temperature is unrealistic. Experimentally, it is known that the surface temperature is related to the burning rate by Equation (48) (see Reference 57). It is the surface temperature, T_{ps} , which provides the link between the burning rate and the gas dynamics. The surface temperature depends on the heat flux from gas to solid phase, and heat flux is evaluated by solving the gas-phase conservation equations.

2.6 Boundary Conditions

To complete the formulation of the theoretical model, boundary conditions must be specified at the gas-solid interface as well as at the free stream. The interface mass and energy balances, illustrated by Figure 5, are obtained by considering the flux balance in a thin control volume around the solid-gas interface.

Mass Balance at the Propellant Surface:

The mass balance of k^{th} species at the propellant surface (see Figure 5a) can be written as

$$(\bar{\rho} \bar{v} \bar{Y}_k)_{0+} = \rho_s r_b Y_{k0-} + (\bar{\rho} D \frac{\partial \bar{Y}_k}{\partial y})_{0+} \quad (49)$$

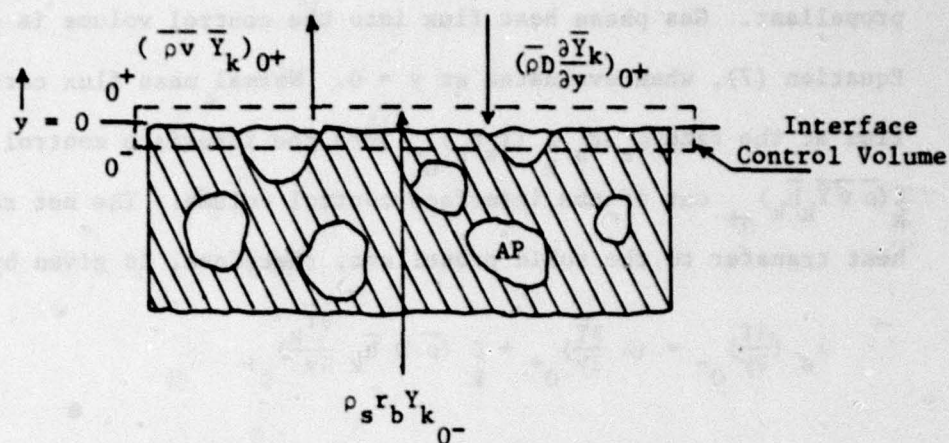
This equation for the solid-gas interface represents the component k transported from the gas to solid by diffusion at the rate $(\bar{\rho} D \frac{\partial \bar{Y}_k}{\partial y})_{0+}$. At the same time, the component k is transported away from the interface by normal velocity at the rate $(\bar{\rho} \bar{v} \bar{Y}_k)_{0+}$ and $\rho_s r_b Y_{k0-}$ in the vaporizing solid surface. It is assumed that there are no reactions at the propellant surface and, therefore, there is no production of species at the surface.

Equation (49) can be written for fuel and oxidizer species in terms of total flux at the inner boundary (I), which corresponds to the surface of the propellant (see Appendix B)

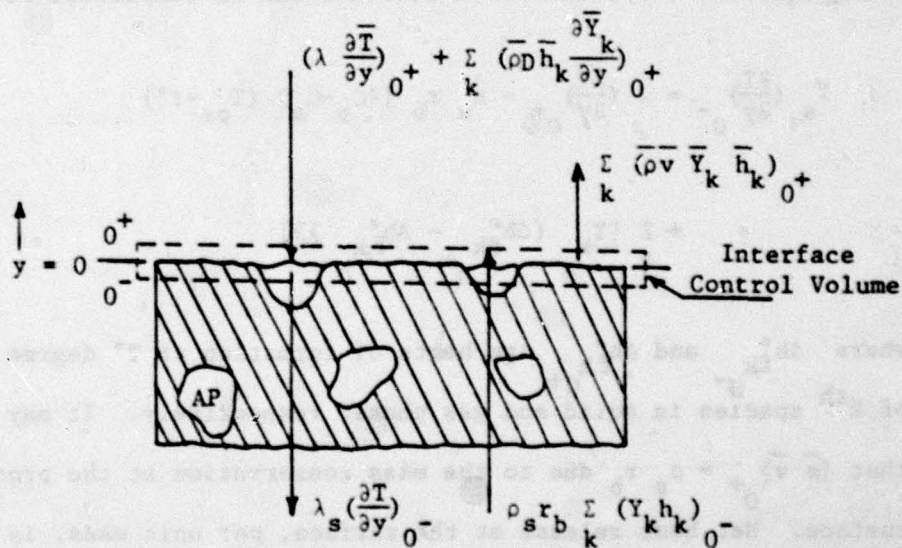
$$J_{\text{tot}, Y_F, I} \equiv \rho_s r_b \bar{Y}_{F0+} - (\frac{\mu}{Sc} \frac{\partial \bar{Y}_F}{\partial y})_{0+} = \rho_s r_b Y_{FS} \quad (50)$$

$$J_{\text{tot}, Y_O, I} \equiv \rho_s r_b \bar{Y}_{O0+} - (\frac{\mu}{Sc} \frac{\partial \bar{Y}_O}{\partial y})_{0+} = \rho_s r_b Y_{OS} \quad (51)$$

Energy Balance at the Propellant Surface:



(a) Mass Balance at the Propellant Surface



(b) Energy Balance at the Propellant Surface

Figure 5 Interface Mass and Energy Balances at the Propellant Surface

Figure 5b illustrates the interface conservation of energy necessary to calculate the net rate of heat transfer to the solid propellant. Gas phase heat flux into the control volume is given by Equation (7), when evaluated at $y = 0$. Normal mass flux carries energy flux at the rate $\rho_s r_b \sum_k (Y_k h_k)_{0^-}$ into the interface control volume and $\sum_k (\bar{\rho} \bar{v} \bar{Y}_k \bar{h}_k)_{0^+}$ out of the interface control volume. The net rate of heat transfer to the solid propellant, therefore, is given by

$$\lambda_s \left(\frac{\partial T}{\partial y} \right)_{0^-} = \left(\lambda \frac{\partial \bar{T}}{\partial y} \right)_{0^+} + \sum_k (\bar{\rho} D \bar{h}_k \frac{\partial \bar{Y}_k}{\partial y})_{0^+} + (\bar{\rho} \bar{v})_{0^+} \sum_k \{ (Y_k h_k)_{0^-} - (\bar{Y}_k \bar{h}_k)_{0^+} \} \quad (52)$$

Using Equation (49), the above equation can be simplified to

$$\lambda_s \left(\frac{\partial T}{\partial y} \right)_{0^-} = \lambda \left(\frac{\partial \bar{T}}{\partial y} \right)_{0^+} - \rho_s r_b [(C_p - C_s) (T_{ps} - T^\circ) + \sum_k \{ Y_k (\Delta h_{f,k}^\circ - \Delta h_{f,k}^\circ) \}] \quad (53)$$

where $\Delta h_{f,k}^\circ$ and $\Delta h_{f,k}^\circ$ are heats of formation at T° degree Kelvin of k^{th} species in solid and gas phases respectively. It may be noted that $(\bar{\rho} \bar{v})_{0^+} = \rho_s r_b$ due to the mass conservation at the propellant surface. Net heat release at the surface, per unit mass, is given by

$$Q_s(T_{ps}) \equiv (C_p - C_s) (T_{ps} - T^\circ) + \sum_k \{ Y_k (\Delta h_{f,k}^\circ - \Delta h_{f,k}^\circ) \} \quad (54)$$

Define net surface heat release (negative for exothermic reactions) at a reference temperature, \bar{T}_{ps} , as:

$$\bar{Q}_s(\bar{T}_{ps}) \equiv (C_p - C_s) (\bar{T}_{ps} - T^\circ) + \sum_k \{ Y_k (\Delta h_{f,k}^\circ - \Delta h_{f,k}^\circ) \} \quad (55)$$

Subtracting Eq. (55) from Equation (54), we get

$$Q_s(T_{ps}) = \bar{Q}_s + (C_p - C_s)(T_{ps} - \bar{T}_{ps}) \quad (56)$$

Substituting Equations (37) and (56) in Equation (52), we finally get

$$\left(\lambda \frac{\partial T}{\partial y}\right)_{0+} = \rho_s r_b \{C_p T_{ps} - C_s T_{pi} + \bar{Q}_s + (C_s - C_p) \bar{T}_{ps}\} \quad (57)$$

Equation (57) can be transformed in terms of total flux of total enthalpy, H , at the inner boundary (see Appendix B).

$$\begin{aligned} J_{tot,H,I} &\equiv \rho_s r_b \bar{H}_{0+} - \left(\frac{\mu}{Pr} \frac{\partial \bar{H}}{\partial y}\right)_{0+} \\ &= \rho_s r_b \{\Delta h_{f,F}^{Y_{FS}} + \Delta h_{f,O}^{Y_{OS}} - C_p T^{\circ} + C_s T_{pi} \\ &\quad - \bar{Q}_s - (C_s - C_p) \bar{T}_{ps}\} \end{aligned} \quad (58)$$

How the surface values of \bar{Y}_O , \bar{Y}_F , \bar{T} , and \bar{H} are evaluated is discussed in Appendix B.

Near-Wall Boundary Conditions for K and ϵ :

Boundary conditions for K and ϵ are applied near the wall rather than at the wall. This avoids the low turbulent Reynolds number region near the wall, where closure models in K and ϵ equations are not valid. Near a wall, production and dissipation terms of K equation (last two terms on the right hand side of Equation 31) are equated (a reasonable approximation), therefore

$$\epsilon = \frac{\mu_t}{\rho} \left(\frac{\partial \bar{u}}{\partial y}\right)^2 \quad (59)$$

Turbulent viscosity, μ_t , close to the wall is calculated from Van Driest's formula (68)

$$\mu_t = \bar{\rho} (kDy)^2 \frac{\partial \bar{u}}{\partial y} \quad (60)$$

where the damping coefficient, D , is given by

$$D = 1 - \exp\left(-\frac{y\sqrt{\bar{\rho}}}{A+\mu}\right) + \exp\left(-\frac{60y}{A+R_h}\right) \quad (61)$$

In Equation (61), τ is the local shear stress, R_h is the surface roughness height, and A^+ (=26) is a constant. The formula given in Equation (60), is particularly useful in including the effects of surface roughness on erosive burning.

From Equations (23), (59), and (60), we can find expressions for K and ϵ , as

$$K = \frac{(kDy)^2}{\sqrt{C_u}} \left(\frac{\partial \bar{u}}{\partial y} \right)^2 \quad (62)$$

$$\epsilon = (kDy)^2 \left(\frac{\partial \bar{u}}{\partial y} \right)^3 \quad (63)$$

Equations (62) and (63) give values of K and ϵ consistent with their distribution in the near-wall region; this can be seen if one uses the log law of the wall for velocity in these equations (see References 64, 69). Chambers and Wilcox (69), recommend that near-wall boundary conditions should be applied at y_+ less than 20. In the present study these boundary conditions were applied at $y_+ = 15$.

Other boundary conditions which are considered in the formulation are given below.

At the Propellant Surface:

$$\bar{u}(x, 0^+) = 0 \quad (64)$$

$$\bar{v}(x, 0^+) = \frac{\rho_s r_b(x)}{\bar{\rho}(x, 0^+)} \quad (65)$$

$$\bar{T}(x, 0^+) = T_{ps}(x) \quad (66)$$

At the Free Stream:

$$\bar{u}(x, \infty) = U_{\infty}(x) \quad (67)$$

$$\bar{T}(x, \infty) = T_{\infty}(x) \quad (68)$$

$$\bar{Y}_O(x, \infty) = 0 \quad (69)$$

$$\bar{Y}_F(x, \infty) = 0 \quad (70)$$

$$\left. \frac{\partial K}{\partial y} \right|_{\infty} = 0 \quad (71)$$

$$\left. \frac{\partial \epsilon}{\partial y} \right|_{\infty} = 0 \quad (72)$$

Governing equations, Equations (27) through (33), with boundary conditions, Equations (48) through (72), complete the theoretical formulation. Partial differential equations are parabolic in nature and are solved numerically.

CHAPTER 3

NUMERICAL METHOD

3.1 Numerical Scheme

The system of coupled nonlinear simultaneous partial differential equations, Equation (27) through Equation (32), are parabolic in nature, and due to their complexity, they must be solved numerically. One can find a number of numerical techniques in literature to solve parabolic partial differential equations; however, several researchers (52, 53, 55, 65) have used the numerical scheme proposed by Patankar and Spalding (70). The same numerical scheme is used in this study. It offers a computational economy, particularly for flows in which the field of interest grows rapidly in thickness (e.g., wall boundary layer in the present study). Patankar and Spalding (70) introduced a transformation of coordinates in which grid points always fit the boundary-layer region even though the thickness of this region is changing.

The following coordinate transformations are introduced for the governing equations:

$$x = x \quad (73)$$

$$\omega = \frac{\psi - \psi_I}{\psi_E - \psi_I} \quad (74)$$

The stream function ψ is defined by

$$\frac{\partial \psi}{\partial x} = -\bar{\rho} \bar{v}^o, \quad \frac{\partial \psi}{\partial y} = \bar{\rho} \bar{u} \quad (75)$$

$$\frac{d\psi_I}{dx} = -\dot{m}_I, \quad \frac{d\psi_E}{dx} = -\dot{m}_E \quad (76)$$

where the subscripts I and E represent inner (wall) and external (free-stream) boundaries of the flow field, respectively. ψ_I and ψ_E are the stream functions at the I and E boundaries of the flow: thus ω equals zero at the I boundary and unity at E. Equation (76) is obtained from the definition of stream function and shows the dependence of ψ_I and ψ_E on x . \dot{m}_I and \dot{m}_E are the rates of mass transfer (mass entrainment rates) across the I and E surfaces. Numerical integration of Equation (76) gives the values of ψ_I and ψ_E , and the way in which mass entrainment rates are computed is discussed in Appendix C.

With the transformations defined by Equations (73) through (76), all governing Equations (27) through (32), are transformed into the following general form:

$$\frac{\partial \phi}{\partial x} + (\hat{a} + \hat{b}\omega) \frac{\partial \phi}{\partial \omega} = \frac{\partial}{\partial \omega} \left\{ \frac{\bar{\rho} \bar{u} \Gamma}{(\psi_E - \psi_I)^2} \frac{\partial \phi}{\partial \omega} \right\} + \hat{d} / \bar{\rho} \bar{u} \quad (77)$$

where ϕ represents any dependent variable (e.g., \bar{u} , \bar{H} , \bar{Y}_k , K , etc.), and the continuity equation, Equation (27) is automatically satisfied by the definition of stream function and need not be used in the solution of Equation (77). Various symbols introduced in Equation (77) are defined below:

$$\hat{a} \equiv \dot{m}_I / (\psi_E - \psi_I) \quad (78)$$

$$\hat{b} \equiv (\dot{m}_E - \dot{m}_I) / (\psi_E - \psi_I) \quad (79)$$

The effective transport coefficient, Γ , for each equation is defined as:

$$\Gamma \equiv \left\{ \begin{array}{ll} \mu_{\text{eff}} & \text{for momentum equation, Equation (28)} \\ (\frac{\mu}{Sc})_{\text{eff}} & \text{for species equation, Equation (29)} \\ (\frac{\mu}{Pr})_{\text{eff}} & \text{for energy equation, Equation (30)} \\ (\mu + \frac{\mu_t}{C_1}) & \text{for K equation, Equation (31)} \\ (\mu + \frac{\mu_t}{C_2}) & \text{for } \epsilon \text{ equation, Equation (32)} \end{array} \right\} \quad (80)$$

The source term parameter, \hat{d} , for each equation is defined as:

$$\hat{d} \equiv \left\{ \begin{array}{ll} -\frac{d\bar{p}}{dx} & \text{for momentum equation, Equation (28)} \\ \dot{\omega}_F & \text{for fuel mass fraction equation, Equation (29)} \\ \frac{\partial}{\partial y} \left[(\mu_{\text{eff}} - (\frac{\mu}{Pr})_{\text{eff}}) \frac{\partial \bar{u}^2/2}{\partial y} \right] & \text{for energy equation, Equation (30)} \\ \mu_t \left(\frac{\partial \bar{u}}{\partial y} \right)^2 - \bar{\rho} \epsilon & \text{for K equation, Equation (31)} \\ C_3 \frac{\epsilon}{K} \mu_t \left(\frac{\partial \bar{u}}{\partial y} \right)^2 - C_4 \frac{\bar{\rho} \epsilon^2}{K} & \text{for } \epsilon \text{ equation, Equation (32)} \end{array} \right\} \quad (81)$$

It may be noted that the source terms defined by \hat{d} in Equation (81) are not written in transformed coordinate system; this is because of the way in which the source terms are evaluated (see Appendix C).

The general partial differential Equation (77) is solved by a finite difference procedure described in Appendix C. The values of ϕ

are solved at discrete values of ω for one value of x ; the task is to obtain the values of ϕ at the same value of ω , but for a slightly greater value of x . By stepwise repetition of this basic operation, the whole flow field of interest is covered. Finite difference equations are obtained by integrating Equation (77) in a small region (control volume) of the flow field (Appendix C). The integration in regions at the boundaries is treated in a special manner; for example, Couette flow analysis is used near the wall boundary. Details of this analysis are given in Appendix B. The final form of the finite difference equations can be put into a tri-diagonal matrix form represented by the following equation:

$$\phi_{1,j} = A_j \phi_{1,j+1} + B_j \phi_{1,j} + C_j \quad (82)$$

Coefficients A_j , B_j , and C_j for various equations are evaluated in terms of grid size, flow properties, and variables at the upstream location. The expressions for the coefficients are given in Appendix C.

61

3.2 Procedure in the Development of the Computer Code

Equation (82) represents six finite difference equations for six variables, \bar{u} , \bar{H} , \bar{Y}_O , \bar{Y}_{OF} , K , and ϵ . These finite difference equations were solved on the 370/168 IBM computer. A computer code was developed for this purpose. The code was developed in such a way that it can solve the following six types of boundary-layer situations:

- 1) laminar incompressible non-reacting,
- 2) laminar compressible non-reacting,
- 3) laminar compressible with surface blowing or suction,
- 4) turbulent incompressible non-reacting,
- 5) turbulent compressible non-reacting, and
- 6) turbulent compressible reacting.

This provision was built into the computer code to solve simpler cases, in order to test the workability both of the code and the numerical scheme. A general layout of the computer program is shown in Figure 6.

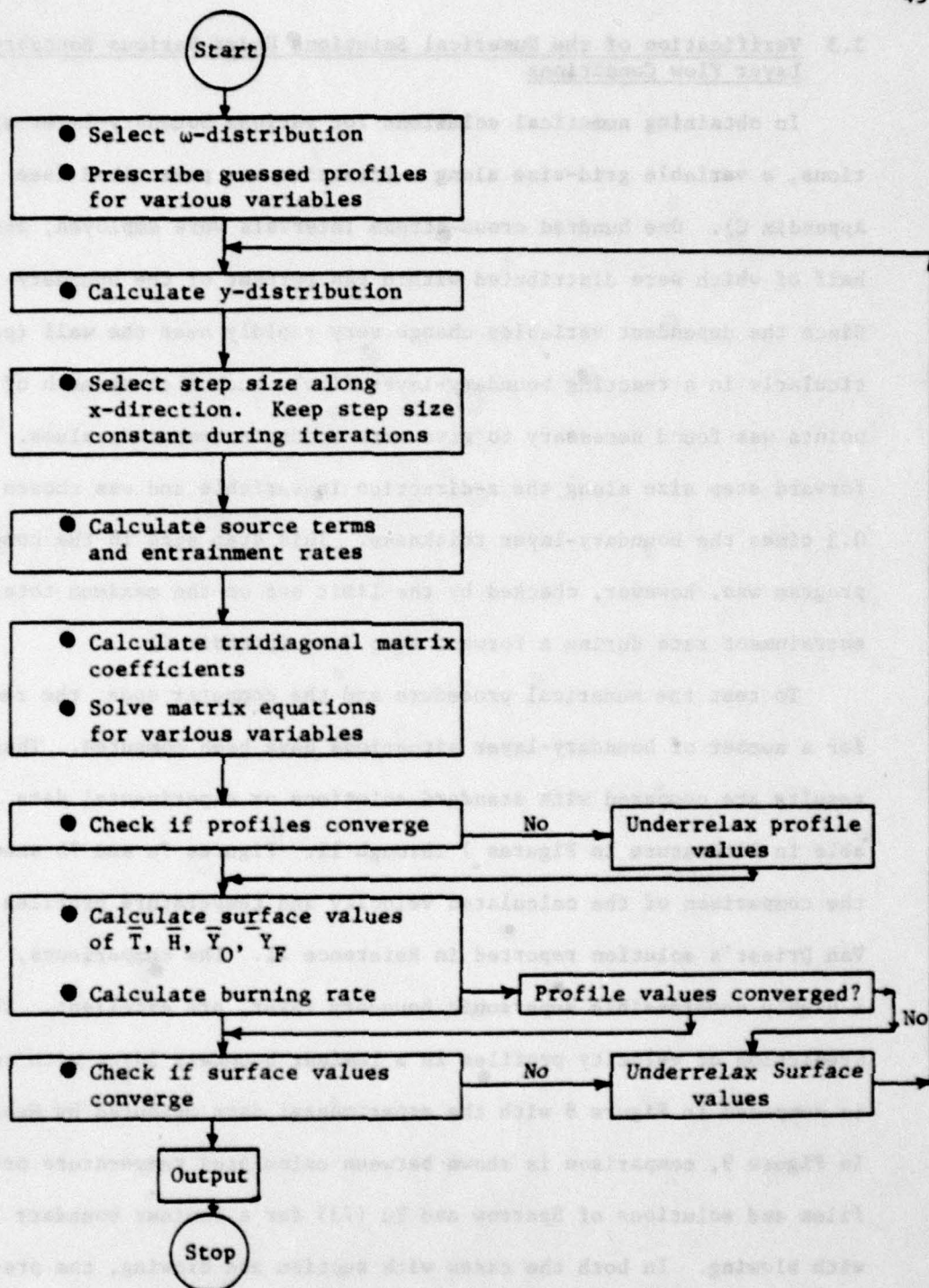


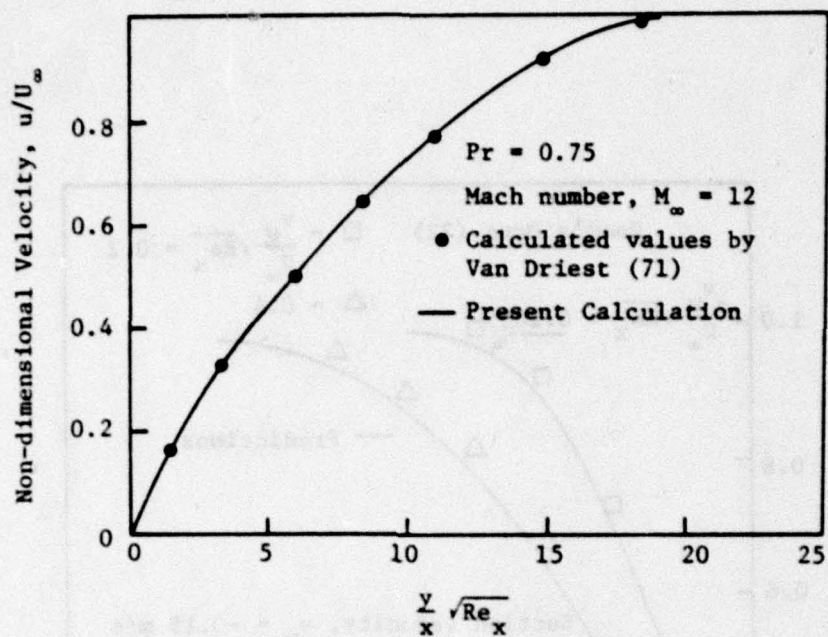
Figure 6 General Layout of the Computer Program

3.3 Verification of the Numerical Solutions Under Various Boundary-Layer Flow Conditions

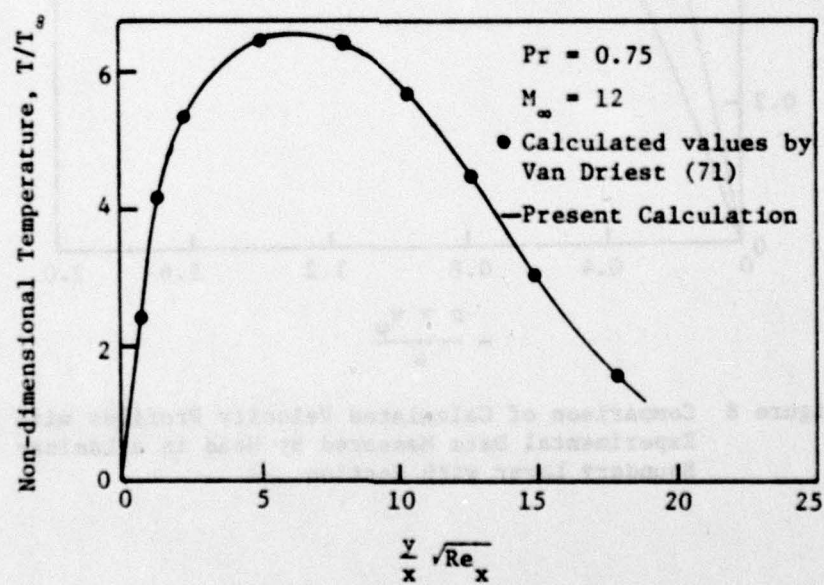
In obtaining numerical solutions for various boundary-layer situations, a variable grid-size along ω -direction was prescribed (see Appendix C). One hundred cross-stream intervals were employed, about half of which were distributed within ten percent of the boundary layer. Since the dependent variables change very rapidly near the wall (particularly in a reacting boundary-layer flow), such a close mesh of grid points was found necessary to give more accurate computed values. The forward step size along the x-direction is variable and was chosen as 0.3 times the boundary-layer thickness. This step size in the computer program was, however, checked by the limit set on the maximum total mass entrainment rate during a forward step (see Appendix C).

To test the numerical procedure and the computer code, the results for a number of boundary-layer situations have been computed. These results are compared with standard solutions or experimental data available in literature in Figures 7 through 11. Figures 7a and 7b show the comparison of the calculated velocity and temperature profiles with Van Driest's solution reported in Reference 71. The comparisons, for a highly compressible supersonic boundary layer, are excellent. The prediction of velocity profiles in a laminar boundary layer with suction is compared in Figure 8 with the experimental data measured by Head (72). In Figure 9, comparison is shown between calculated temperature profiles and solutions of Sparrow and Yu (73) for a laminar boundary layer with blowing. In both the cases with suction and blowing, the predictions are very good.

Because of experimental difficulties, there is very little experimental data in literature on various turbulence quantities (e.g.,



(a) Velocity Distribution



(b) Temperature Distribution

Figure 7 Comparison of Calculated Velocity and Temperature Profiles with Van Driest's Solution for a Highly Compressible Supersonic Boundary Layer

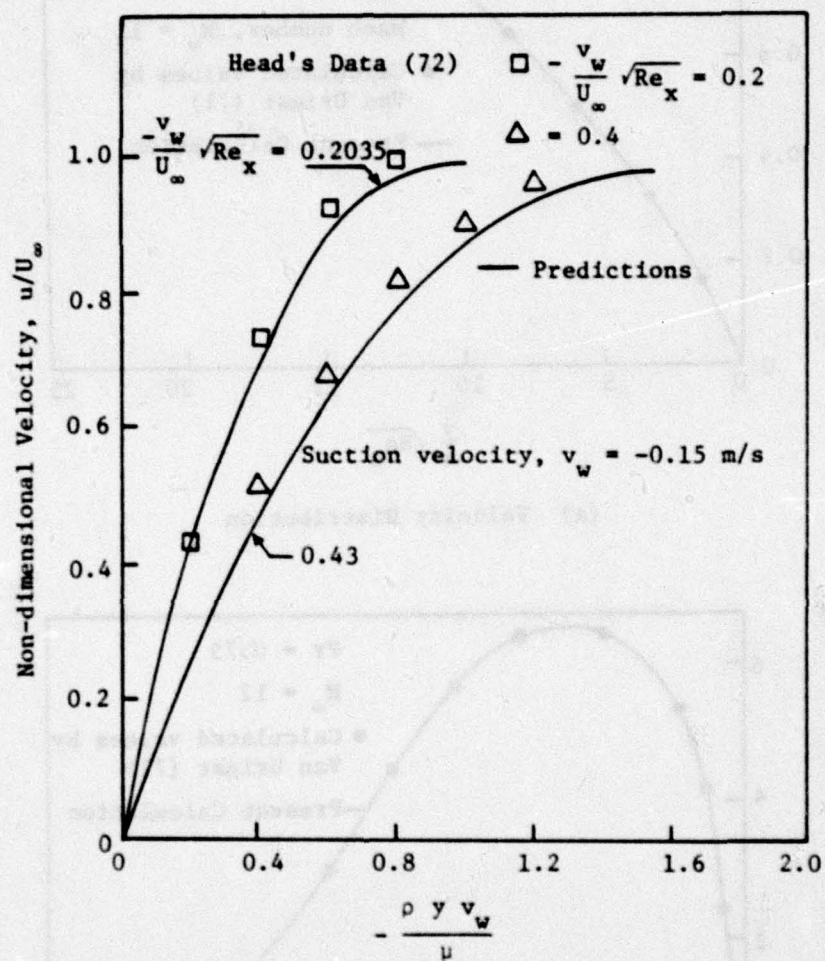


Figure 8 Comparison of Calculated Velocity Profiles with the Experimental Data Measured by Head in a Laminar Boundary Layer with Suction

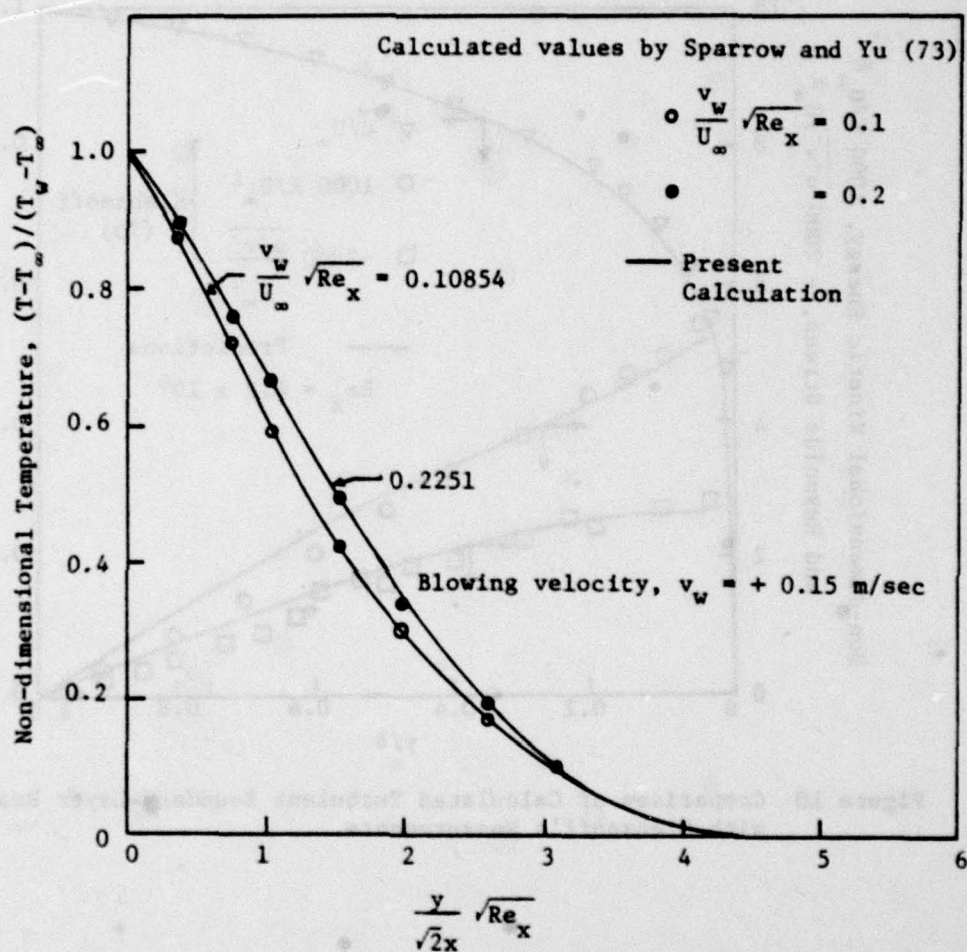


Figure 9 Comparison of Calculated Temperature Profiles with Solutions of Sparrow and Yu for a Laminar Boundary Layer with Blowing

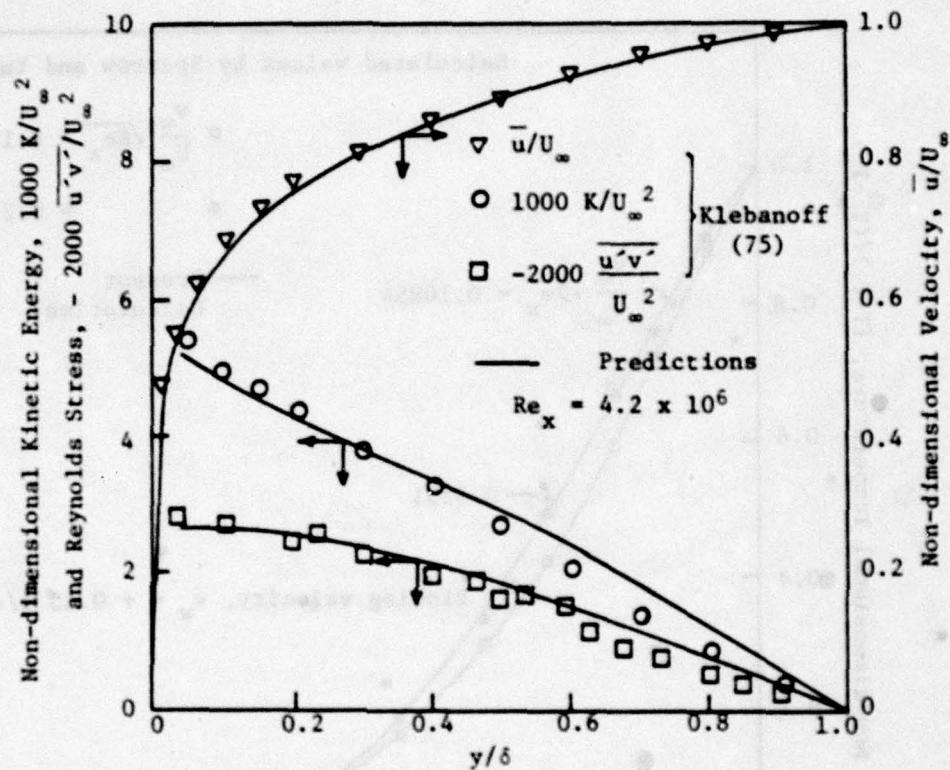


Figure 10 Comparison of Calculated Turbulent Boundary-Layer Results with Klebanoff's Measurements

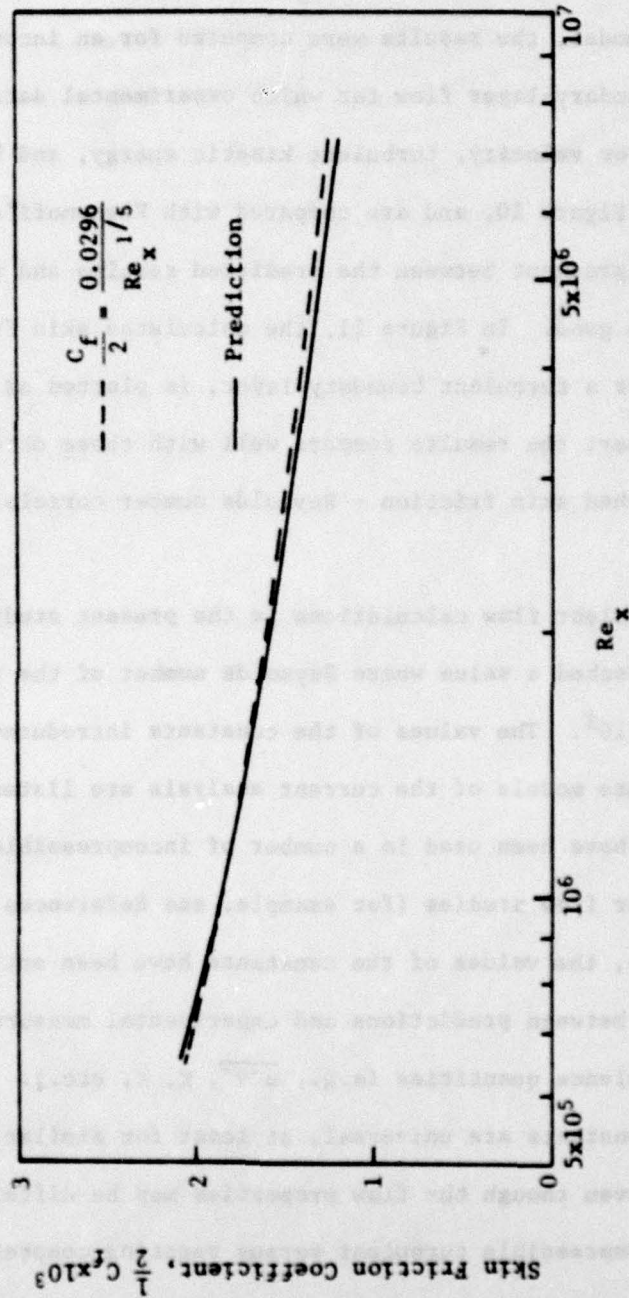


Figure 11 Calculated Skin Friction Coefficient for Incompressible Turbulent Boundary Layer over a Flat Plate

$\overline{u'v'}$, K , ϵ) for a chemically reacting turbulent boundary-layer flow over an ablating propellant surface. However, to test the validity of the turbulence models and the near-wall treatment of K and ϵ equations in the present model, the results were computed for an incompressible turbulent boundary-layer flow for which experimental data is available. The results for velocity, turbulent kinetic energy, and Reynolds stress are shown in Figure 10, and are compared with Klebanoff's (75) measurements. The agreement between the predicted results and the experimental data is quite good. In Figure 11, the calculated skin friction coefficient, for a turbulent boundary layer, is plotted as a function of Reynolds number; the results compare well with those obtained from a well-established skin friction - Reynolds number correlation shown in Figure 11.

All turbulent flow calculations in the present study were begun when x had reached a value where Reynolds number of the free stream was equal to 10^5 . The values of the constants introduced in the turbulence closure models of the current analysis are listed in Table 2. These values have been used in a number of incompressible turbulent boundary-layer flow studies (for example, see References 64 and 74). In these studies, the values of the constants have been optimized to obtain a good match between predictions and experimental measurements of various turbulence quantities (e.g., $\overline{u'v'}$, K , ϵ , etc.). It is presumed that these constants are universal, at least for similar types of flow situations, even though the flow properties may be different; for example, incompressible turbulent versus reacting compressible turbulent boundary layers. This presumption has been made, with good results, in a number of reactive flow studies (52, 53, 55). The results of some

Table 2

Values of the Constants Used in Turbulence Modeling

Constant	Present Study	Flow Situations of Other Studies with Same Values
C_1	1.0	Diffusional Reacting Flow, Refs.: 52, 53, 55
C_2	1.3	Diffusional Reacting Flow, Refs.: 52, 53, 55
C_3	1.57	Diffusional Reacting Flow, Refs.: 53
C_4	2.0	Diffusional Reacting Flow, Ref. 55
C_{EBU}	0.53*	Premixed Reacting Flow, Ref. 65
C_{g1}	2.8*	Diffusional Reacting Flow, Ref. 52, 53, 55
C_{g2}	1.789*	Diffusional Reacting Flow, Ref. 52
C_ω	0.18	Estimated from C_{EBU} , C_{g1} , and C_{g2}
C_u	0.09	Diffusional Reacting Flow, Refs. 52, 53, 55
σ_g	0.7	Diffusional Reacting Flow, Refs.: 52, 53, 55

*Constants used in the estimation of C_ω

71

of these reactive flow boundary-layer studies have also compared well with measured experimental data (52, 53, 55, 65).

Flow dimensionless at inlet Reynolds number	Reynolds number	Flow dimensionless at inlet Reynolds number
0.1	0.1	0.1
0.2	0.2	0.2
0.3	0.3	0.3
0.4	0.4	0.4
0.5	0.5	0.5
0.6	0.6	0.6
0.7	0.7	0.7
0.8	0.8	0.8
0.9	0.9	0.9
1.0	1.0	1.0
1.1	1.1	1.1
1.2	1.2	1.2
1.3	1.3	1.3
1.4	1.4	1.4
1.5	1.5	1.5
1.6	1.6	1.6
1.7	1.7	1.7
1.8	1.8	1.8
1.9	1.9	1.9
2.0	2.0	2.0
2.1	2.1	2.1
2.2	2.2	2.2
2.3	2.3	2.3
2.4	2.4	2.4
2.5	2.5	2.5
2.6	2.6	2.6
2.7	2.7	2.7
2.8	2.8	2.8
2.9	2.9	2.9
3.0	3.0	3.0
3.1	3.1	3.1
3.2	3.2	3.2
3.3	3.3	3.3
3.4	3.4	3.4
3.5	3.5	3.5
3.6	3.6	3.6
3.7	3.7	3.7
3.8	3.8	3.8
3.9	3.9	3.9
4.0	4.0	4.0
4.1	4.1	4.1
4.2	4.2	4.2
4.3	4.3	4.3
4.4	4.4	4.4
4.5	4.5	4.5
4.6	4.6	4.6
4.7	4.7	4.7
4.8	4.8	4.8
4.9	4.9	4.9
5.0	5.0	5.0
5.1	5.1	5.1
5.2	5.2	5.2
5.3	5.3	5.3
5.4	5.4	5.4
5.5	5.5	5.5
5.6	5.6	5.6
5.7	5.7	5.7
5.8	5.8	5.8
5.9	5.9	5.9
6.0	6.0	6.0
6.1	6.1	6.1
6.2	6.2	6.2
6.3	6.3	6.3
6.4	6.4	6.4
6.5	6.5	6.5
6.6	6.6	6.6
6.7	6.7	6.7
6.8	6.8	6.8
6.9	6.9	6.9
7.0	7.0	7.0
7.1	7.1	7.1
7.2	7.2	7.2
7.3	7.3	7.3
7.4	7.4	7.4
7.5	7.5	7.5
7.6	7.6	7.6
7.7	7.7	7.7
7.8	7.8	7.8
7.9	7.9	7.9
8.0	8.0	8.0
8.1	8.1	8.1
8.2	8.2	8.2
8.3	8.3	8.3
8.4	8.4	8.4
8.5	8.5	8.5
8.6	8.6	8.6
8.7	8.7	8.7
8.8	8.8	8.8
8.9	8.9	8.9
9.0	9.0	9.0
9.1	9.1	9.1
9.2	9.2	9.2
9.3	9.3	9.3
9.4	9.4	9.4
9.5	9.5	9.5
9.6	9.6	9.6
9.7	9.7	9.7
9.8	9.8	9.8
9.9	9.9	9.9
10.0	10.0	10.0

3.4 Iteration Procedure for Burning Rate Calculation

The burning rate given by Equation (48) is an exponential function of the propellant surface temperature and, therefore, is very sensitive to changes in surface temperature. The surface temperature is found from the interface energy balance, Equation (57). However, gas-to-solid heat flux, needed in Equation (57), must be calculated from the solution of the temperature distribution in the boundary layer. Therefore, calculations were started with a guessed value of surface temperature; iterations of the boundary-layer profiles and the surface temperature were found necessary to achieve a good convergence. During the iterations, under-relaxation of boundary-layer profiles, surface temperature, and surface mass fractions were found necessary for achieving stability (see Figure 6). Except for the first few stations, the number of iterations rarely exceeded 2. The convergence criteria for surface temperature was set at 0.05% and that for boundary layer-profiles was set at 0.1%.

CHAPTER 4

EXPERIMENTAL WORK

The objective of the experimental work was to measure the burning rate of a composite solid propellant under erosive-burning conditions. A number of erosive-burning experiments have been conducted in previous studies (see section 1.2.1); however, none of those experiments were designed to be compatible for a boundary-layer type of theoretical analysis. Although Marklund and Lake's data (26) is useful in comparing a boundary-layer solution of erosive burning, their data is restricted to low free-stream velocities. In most of the previous work, the free-stream velocities have been limited to low values and, therefore, there is a need for erosive-burning data at higher velocities.

The present experiments were designed for verification purposes, so that erosive-burning rates measured at various free-stream velocities and pressures can be compared with the theoretical predictions. In an actual rocket motor the propellant grain is usually cylindrical in shape. The present experiments, however, were designed for a flat test propellant geometry consistent with the theoretical model. A theoretical model can be developed for the burning of a cylindrical type of solid propellant; however, it is difficult to get direct erosive-burning rate measurements in a real rocket grain. Instead, the erosive effect has to be indirectly computed from the pressure-time traces of the rocket motor firings. Erosive-burning data in the present experiments were obtained directly, and the theoretical analysis after verification with experimental data can be extended easily to a cylindrical shaped propellant geometry.

In the design consideration, two requirements were imposed on the structure of the experimental apparatus: (a) experiments should be compatible with the theoretical model, and (b) conditions of test propellant burning should be similar to that surrounding combustion of a typical solid propellant motor. Therefore, a turbulent boundary layer should be formed over a flat test propellant surface by the flow of a high-velocity gas and the propellant should burn at typical rocket pressures of 50-100 atm.

4.1 Burning Rate Measurement

The experimental apparatus was designed to measure the burning rate of a test propellant sample by two methods: Laser-photodiode servomechanism and high-speed motion picture.

4.1.1 Laser-Photodiode Servomechanism Method

The basic components for this method consist of: a 2 mw, 6328 Å He-Ne Laser, a 10 Å width band-pass filter, a light-sensitive photodiode, a control amplifier, a recording system, and a high-torque stepper motor with maximum feeding rate of 900 pulses/sec at 1.8° per pulse.

A schematic diagram of the Laser-Photodiode servomechanism technique is shown in Figure 12. As the surface of the burning solid propellant sample recedes, the laser beam (previously blocked by the propellant) passes through a band-pass filter to restrict any light from the combustion zone. The beam is detected by the photodiode which generates a small current signal. This signal is amplified in the control amplifier and supplied to the stepper motor, which advances the propellant sample counter to the receding propellant surface. If the stepper motor advances the propellant too quickly, the laser beam is blocked, the signal to the motor discontinues, and propellant-strip feeding stops. Thus, feeding rate is controlled by burning rate. The feeding rate by the stepper motor is recorded by the recording system at all times during the experiment, thus giving the instantaneous burning rate of a propellant sample.

The function of the Laser-photodiode servomechanism was tested for strand burning of a sample propellant. However, when used in the erosive-burning test chamber, the combustion gases deposited carbon particles

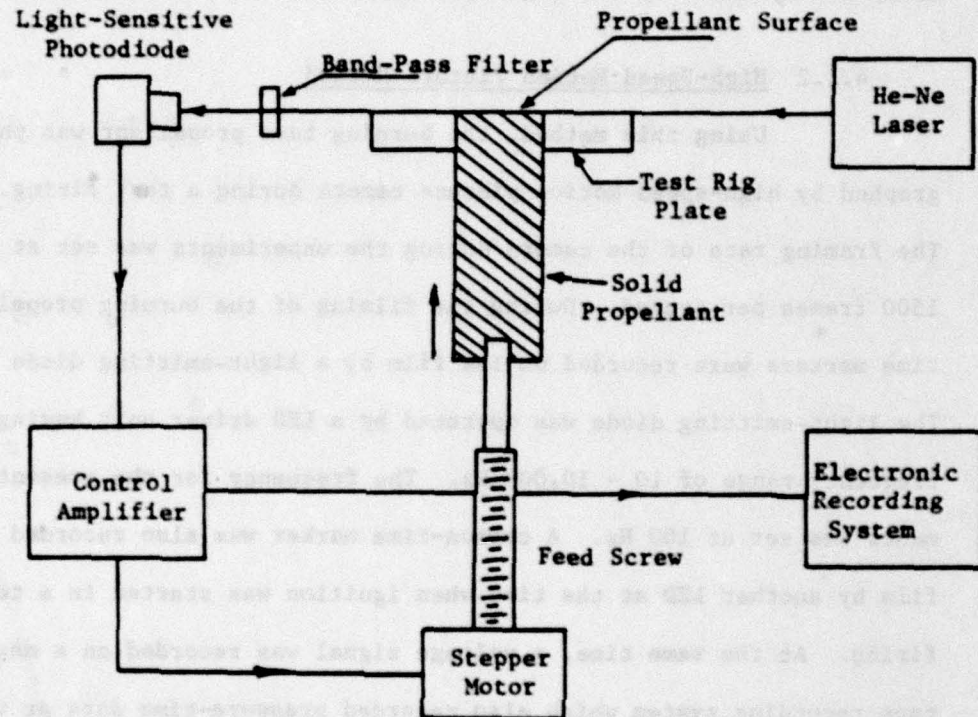


Figure 12 Schematic Diagram of Laser-Photodiode Servomechanism

and other product gases on the transparent plexiglass windows of the chamber, thus blocking the laser beam from passing over the propellant surface. Considerable effort was made to solve this problem (see section 6.3 for recommended remedies in using the Laser-Photodiode servomechanism). The erosive-burning data measured in the present study was obtained by the high-speed motion picture method only.

4.1.2 High-Speed Motion Picture Method

Using this method, the burning test propellant was photographed by high-speed motion picture camera during a test firing. The framing rate of the camera during the experiments was set at about 1500 frames per second. During the filming of the burning propellant, time markers were recorded on the film by a light-emitting diode (LED). The light-emitting diode was operated by a LED driver unit having a frequency range of 10 - 10,000 Hz. The frequency for the present experiments was set at 100 Hz. A common-time marker was also recorded on the film by another LED at the time when ignition was started in a test firing. At the same time, a voltage signal was recorded on a magnetic tape recording system which also recorded pressure-time data at various locations of the test rig. In this way burning rate versus time data was correlated with pressure versus time data. The film was analyzed, frame by frame, on a motion analyzer designed to calculate the distance burnt in a known time period. Further description of the test firing procedure and data acquisition system is given in the following sections.

4.2 Erosive-Burning Test-Rig Design

The design of various components of the test rig depends on the gas-dynamic operating conditions (pressure, temperature, and velocity). Basic equations used for the design of the test rig, and a parametric study for the effects of various geometric inputs of the test rig on the solutions of these equations are presented in Appendix D. Various materials and dimensions of the test rig were selected on the basis of the parametric study and the requirements of high-pressure and high-temperature gas flow. A schematic diagram of the test rig is shown in Figure 13, and a photograph of the assembled erosive-burning test rig is shown in Figure 14. Description and function of each important component is given below.

4.2.1 Driving Motor

A high-pressure, high-velocity, hot-combustion gas flow is needed to simulate actual rocket conditions. Such a gas flow was generated in the driving motor by burning a 30 cm long and 11.96 cm outer diameter, 8-point star-shaped solid-propellant grain. The propellant grain (N-4) is the same as that used in the sidewinder 1A motor, and has neutral burning characteristics (constant mass burning rate) which help to maintain a steady-state pressure in the test chamber after a short ignition transient interval. Various properties of the N-4 solid propellant grain are given in Table 3. The driving motor was made of 304 stainless steel, and it has a length of 30 cm, an inner diameter of 12 cm, and an outer diameter of 17.8 cm. A photograph of the driving motor is shown in Figure 15.

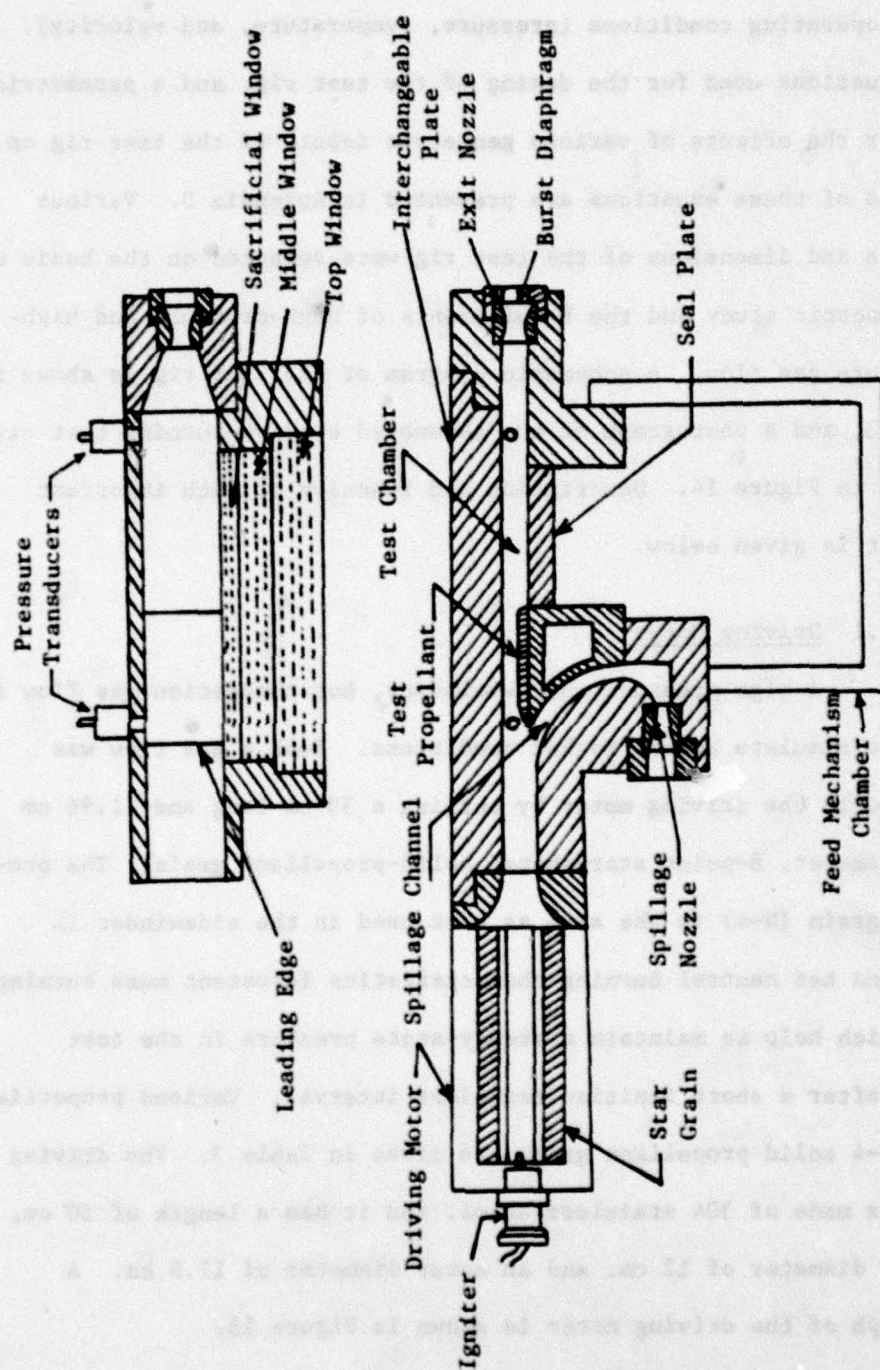


Figure 13 Schematic Diagram of the Erosive-Burning Test Rig

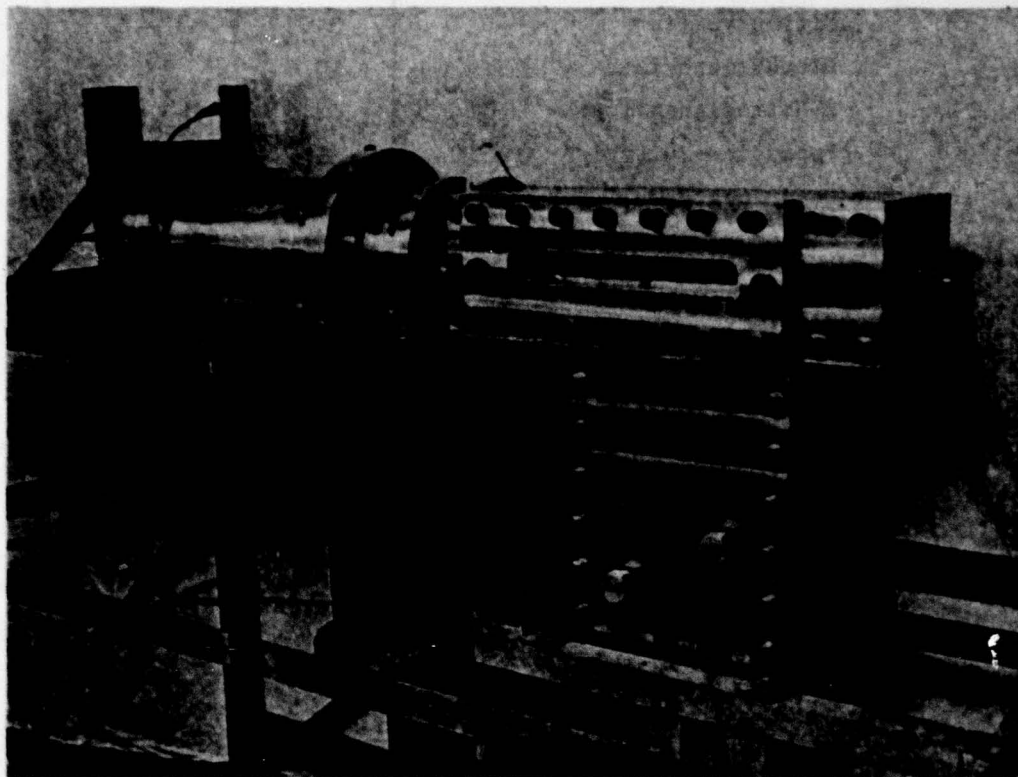


Figure 14 Assembly View of the Erosive-Burning Test Rig

Table 3

Properties of N-4 Solid Propellant Grain

<u>CONSTITUENTS</u>	<u>% BY WEIGHT</u>
Nitrocellulose (12.6% N)	51.0
Nitroglycerin	34.3
Diethylphthalate	10.6
2-Nitrodiphenylamine	2.0
Potassium Sulfate	1.5
Lead Stearate	0.5
Carbon Black	0.1
<u>EXHAUST-GAS COMPOSITION</u>	<u>% MOLE</u>
CO	45.03
H ₂ O	18.11
H ₂	16.80
N ₂	11.07
CO ₂	8.96
H	0.03
<u>PROPELLANT DATA</u>	
Initial surface -to-length ratio	32.1 cm
Length	30.0 cm
Propellant density	1570 Kg/m ³
Temperature of combustion gases	2258 K
Average molecular weight of combustion gases	23.5 Kg/Kmole
a* (for a pressure range of 3.45 - 20.7 MPa)	0.3323 cm/s/(MPa) ^{n*}
n*	0.542

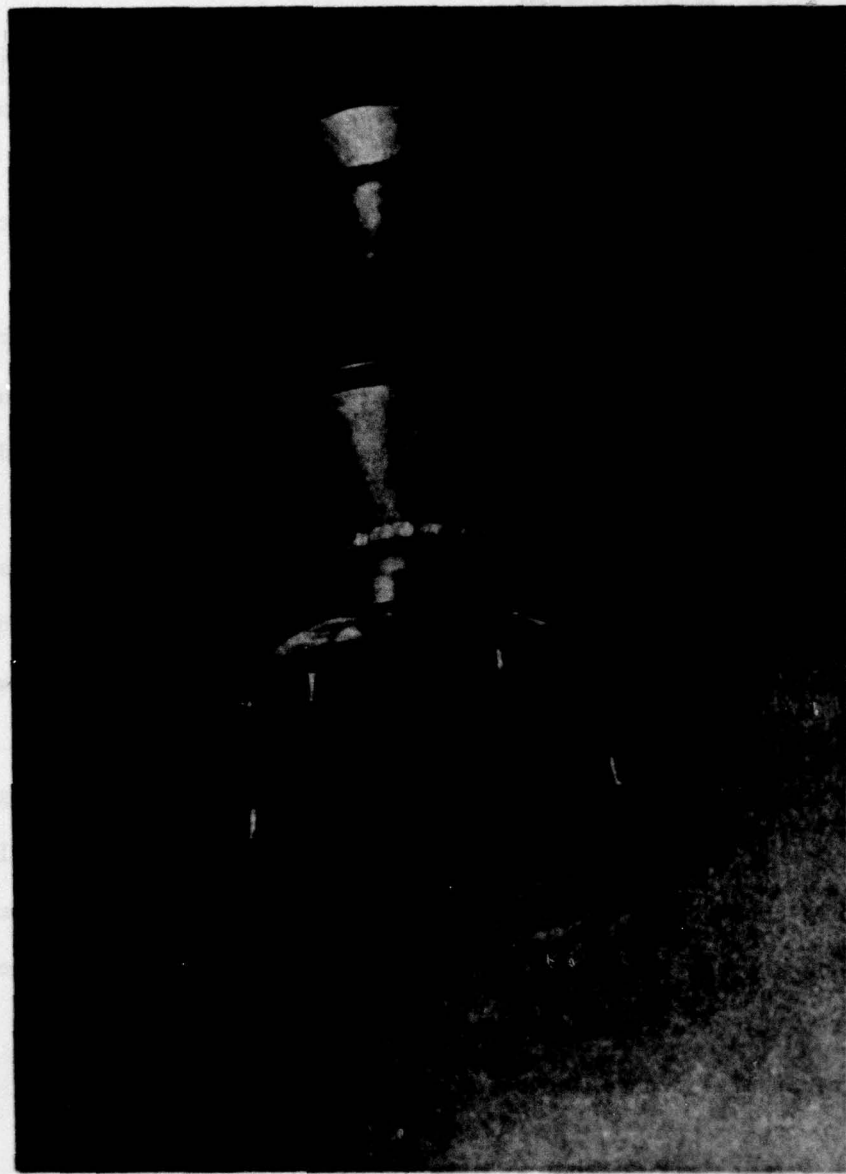


Figure 15 Assembly View of the Driving Motor and the Rectangular Convergent Nozzle

4.2.2 Igniter System

To ignite the propellant charge in the driving motor, a pyrotechnic igniter (Redstone Arsenal, MK 125 MOD 5), which contains a mixture of black powder and magnesium, was used. The igniter was set off by an electric squib which was operated by a remotely controlled ignition circuit discussed in section 4.3.5. The igniter was supplied with a 50 volts AC and 5 amperes of current through an igniter wire. One end of the igniter wire was connected to the igniter through an insulated electrode gland feedthrough (Nanmac Corporation, model A-501-Cu (ss)), and the other end was connected to the test rig body which served as a common ground. The pyrotechnic igniter was held in a stainless igniter holder threaded into a flange attached at a head-end of the driving motor. A photograph of the pyrotechnic igniter system is shown in Figure 16.

After the ignition of the propellant grain, the product gases flow out of the driving motor into the test chamber through a nozzle. This nozzle constructed of 304 stainless steel, was designed to converge from a square cross section (42.3 cm^2) at the end of the driving motor (see Figure 15) to a rectangular cross section (7 cm x 2.54 cm) at the entrance of a test chamber.

4.2.3 Test Chamber

Several important elements were designed to form the 39 cm long test chamber made of 304 stainless steel with a rectangular cross section of 7 cm x 2.54 cm. These elements are described below:

- (a) An interchangeable wedge-shaped stainless steel leading edge was attached to a stainless steel flat plate. A photograph showing the leading edge in the test chamber is shown in

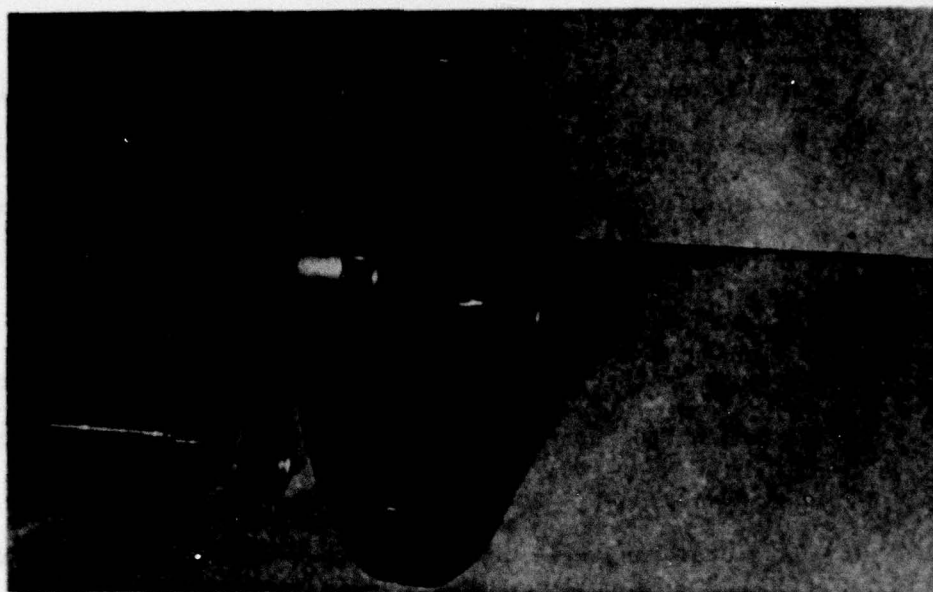


Figure 16 Pyrotechnic Igniter System

Figure 17. The length of the leading edge was 10.8 cm and its width was equal to 7.5 cm. A test-propellant sample was glued with an epoxy to the top flat surface of the leading edge. The length of the leading edge allowed most of the propellant to have a turbulent boundary layer over it. It may be mentioned that the seal plate (see Figure 13) must be removed when the Laser-Photodiode servomechanism technique is used in order for a propellant sample to be fed upwards into the test chamber.

- (b) A spillage channel was provided. Through this channel a small amount of the product gases flowed out of the test chamber, enabling the boundary layer to develop from the beginning of the leading edge.
- (c) An interchangeable top plate was designed to vary the channel height in the test section to change gas velocity. Pressure gradient can also be controlled by using a tapered top plate.
- (d) A convergent-divergent interchangeable exit nozzle, made of stainless steel, was designed to control the mass flow and gas velocity in the test chamber. Various nozzles were used with throat diameters of 1.93 cm, 2.08 cm, and 2.42 cm. The exit-nozzle assembly contained a burst diaphragm designed to rupture at a given critical pressure (450 psia). A small nozzle with a throat diameter of 0.65 cm was used at the end of the spillage channel. To ensure that the spillage channel remained open during the test firing, the burst diaphragm was not used in the small nozzle.

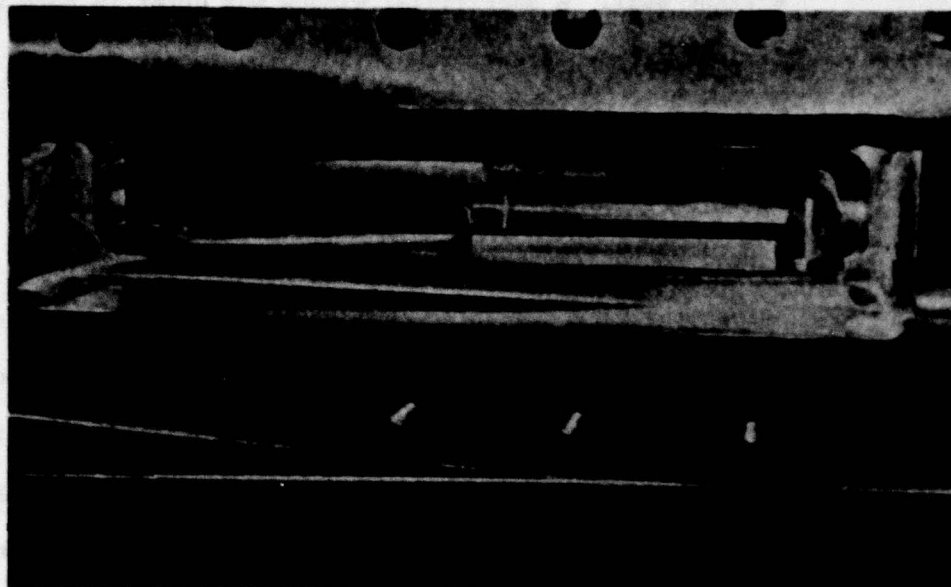


Figure 17 Close-Up View of the Test Section
and the Leading Edge

- (e) A transparent plexiglass window assembly composed of an inner sacrificial plexiglass window (25.4 cm x 3.81 cm x 1.27 cm), a middle window (25.4 cm x 3.81 cm x 2.54 cm), and a top window (27.94 cm x 6.35 cm x 3.81 cm) was used. Rubber O-rings between the middle and top windows were used to achieve a tight seal. A sacrificial window was burnt in each test firing, and replaced for each subsequent test firing. The test-propellant sample was clearly visible through the plexiglass window assembly.

4.2.4 Feed Mechanism and Pressure Equalizer Chamber

Both the feed mechanism chamber and the pressure equalizer were made for the Laser-photodiode servomechanism technique. The feed mechanism chamber was designed to house a feeding mechanism consisting of a feed screw through which rotational motion is converted to linear vertical motion of a rectangular element by means of a threaded nut. The propellant test sample is carried by the rectangular element. A ball feed screw (1/2 inch double threaded having a 1/2 inch lead) is used to feed the propellant sample. The torque requirement of the stepper motor depends on the total load on the motor and the friction and efficiency of the feed screw. To minimize the torque requirement of the stepper motors, the pressure difference between the test chamber and the feed mechanism chamber should be kept minimal. This is achieved by means of the pressure equalizer chamber which consists of a piston and a cylinder. The piston is connected with a spring and a damper to reduce oscillations of the piston. The chamber is connected to the test chamber and to the feed mechanism chamber. Higher pressure in the test chamber pushes down the piston, compressing the gas below it,

and thus increasing the pressure in the feed mechanism chamber. Consequently, as predicted by the parametric study given in Appendix D, the pressure difference between the test chamber and the feed mechanism chamber is reduced substantially.

In this study, as already mentioned, the burning rate was measured by the high-speed motion picture method. Therefore, the pressure equalizer chamber was disconnected from the test rig and a seal plate was kept between the test chamber and the feed mechanism chamber, as shown in Figure 13.

4.3 Instrumentation

4.3.1 Pressure Measuring Equipment

The pressure measuring system consists of Piezo-electric quartz transducers, charge amplifiers, and a recording system. Pressure was measured at three locations: 1) near the inlet to the rectangular convergent nozzle at the exit of the driver motor, 2) near the leading edge, and 3) near the exit nozzle.

The pressure transducers (Kistler Model 601B), with a pressure range up to 1,000 atm, were used. These transducers were equipped with water-cooled adapters (Kistler Model 628C) which protected the transducers from excessive heating by the high temperature gases. The charge signal which is proportional to the pressure signal was amplified through a charge amplifier (Kistler Model 504E) and recorded on a tape recorder.

Calibrations of pressure measurements were made through the charge amplifiers. The pressure transducers used in the experiments were calibrated by the manufacturer in terms of a charge (pc) produced per unit of pressure (psi). The procedure followed in calibrating the pressure measurements was to apply a DC voltage equal to the transducer sensitivity, S (pc/psi), to the charge amplifier. The output from the charge amplifier, which represents the measured pressure in terms of voltage, was then recorded. The output voltage from the charge amplifier can be calculated from the following formula:

$$V_{\text{output}} = - \frac{V_{\text{input}} (\text{volts}) \times 1000 (\text{pf})}{R \left(\frac{\text{psi}}{\text{volt}} \right) \times S \left(\frac{\text{pc}}{\text{psi}} \right)} \quad (83)$$

where R is the range multiplier setting (2000 psi/volt in most of the test firings). This calibration procedure was checked periodically by

measuring a known pressure (using high pressure nitrogen) with the same transducers as those used in the present experiments.

4.3.2 Camera System

A 16 mm high-speed motion picture camera (400-foot capacity Hycam Model K20S4E-115) was used. This camera operates up to a maximum framing rate of 11,000 pictures per second. A 200-foot Kodak chrome color film was used in each test firing. The camera was equipped with two red light-emitting diodes, one for the common-time marker and the other for generating timing signals at a pre-selected frequency, as mentioned in section 4.1.2. The light-emitting diodes were operated by a timing light generator (LED driver), which was fabricated at The Pennsylvania State University Electronics Services and has a frequency range of 10 Hz to 10,000 Hz. A telescopic lens (Elgeet Rochester Co., 6 inch, f 3.8, Cine Navitar No. A2305) was also used with the camera.

4.3.3 Motion Analyzer

The Vanguard motion analyzer (M-16GD Serial No. 772 projection head, C-11D Serial No. 773 Projection case) was used to analyze the film. The motion analyzer projects a four-times magnified picture on a screen. The screen has two crosshairs which can be moved in x and y directions. The distance moved by these crosshairs is obtained from two micrometer dials, accurate to a thousandth of an inch. A frame counter is also provided to record the number of frames moved between readings. The analyzer can advance film a single frame at a time or at a faster rate. The readings taken from the analyzer were the y-distances (propellant surface location) at a fixed x location, and the frame dial readings between each reading. Readings were taken

91

approximately 100 frames apart. The number of frames between each reading were recorded from the dial readings and the time interval was calculated from the number of time markers between the dial readings. To convert the y-dial readings recorded from the magnified image to the actual readings, each y-dial reading was multiplied by a scale factor. The scale factor is defined as the ratio between actual object thickness (measured propellant thickness before ignition) to the projected image thickness (y-dial reading of the propellant before ignition).

4.3.4 Data Acquisition System

Figure 18 illustrates the components of the data acquisition system used in the present study for pressure measurements. It consists of pressure transducers, charge amplifiers (Kistler Model 504E), a 14-channel tape recorder (Hewlett Packard Model 3924 Tape system), a 4-channel transient wave form digitizer (Biomation Model 1015), an oscilloscope (Tektronix type 535A), an x-y plotter (Hewlett-Packard 7044A), a high-speed movie camera, an LED driver unit, and a motion analyzer. A pressure transducer produces a small electric charge proportional to the pressure in the test chamber. This charge is carried by an insulated high impedance cable to the charge amplifier, which after amplification converts it into voltage output proportional to the pressure. The output of the charge amplifier is recorded on an FM channel of the tape recorder. Output of the tape recorder is connected to the Biomation digitizer which converts the data from analogue to digital form. The data can be displayed on an oscilloscope or plotted on the x-y plotter for a hard copy. The burning rate data is obtained through the use of high-speed motion picture camera and motion analyzer.

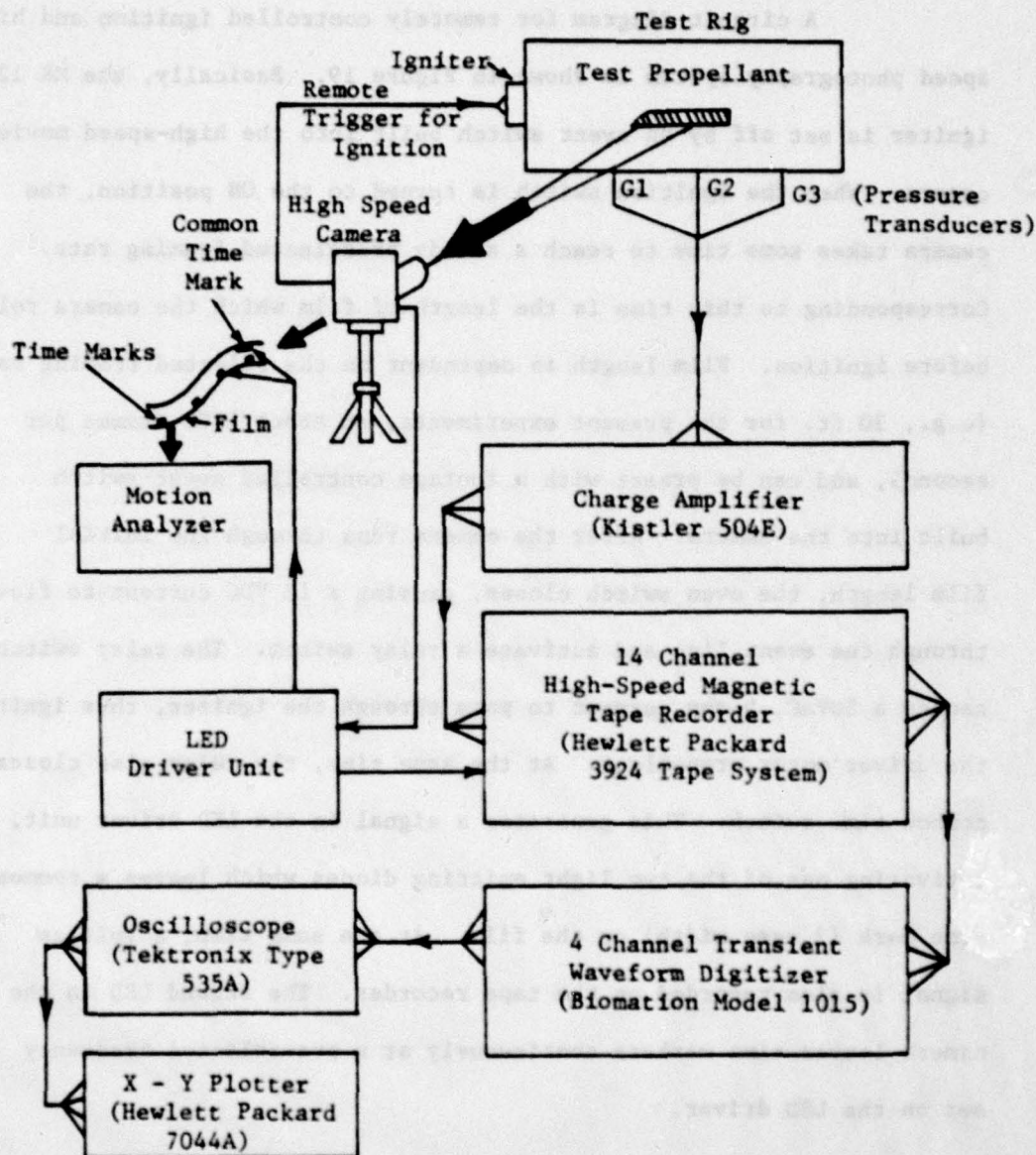


Figure 18 Schematic Diagram of Data-Acquisition System

4.3.5 Remotely Controlled Ignition System

A circuit diagram for remotely controlled ignition and high-speed photography system is shown in Figure 19. Basically, the MK 125 igniter is set off by an event switch built into the high-speed movie camera. When the Ignition switch is turned to the ON position, the camera takes some time to reach a steady preselected framing rate. Corresponding to this time is the length of film which the camera rolls before ignition. Film length is dependent on the selected framing rate (e.g., 30 ft. for the present experiments, at about 1500 frames per second), and can be preset with a footage controlled event switch built into the camera. After the camera runs through the initial film length, the even switch closes, causing a 13 VDC current to flow through the event line and activate a relay switch. The relay switch causes a 50VAC, 5 amp current to pass through the igniter, thus igniting the driver motor propellant. At the same time, the relay also closes a common time switch. This generates a signal in the LED driver unit, activating one of the two light emitting diodes which leaves a common time mark (2 msec width) on the film. At the same time, a voltage signal is also recorded on the tape recorder. The second LED in the camera leaves time markers continuously at a pre-selected frequency set on the LED driver.

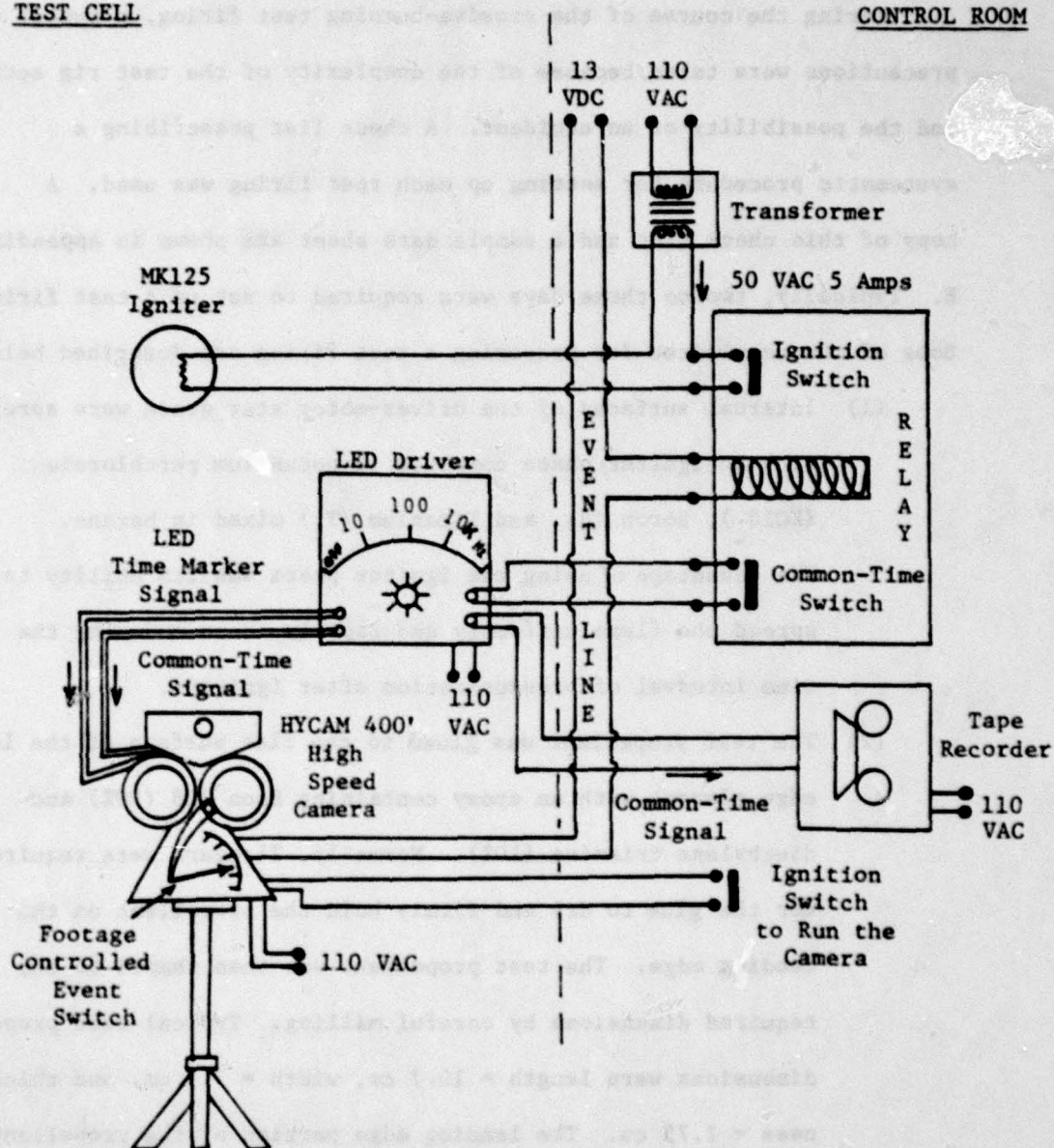
TEST CELLCONTROL ROOM

Figure 19 Circuit Diagram for Remotely Controlled Ignition and High-Speed Photography System

AD-A077 351

ATLANTIC RESEARCH CORP ALEXANDRIA VA
TURBULENT BOUNDARY-LAYER ANALYSIS AND EXPERIMENTAL INVESTIGATION--ETC(U)
MAR 79 M K RAZDAN , K K KUO

F/G 21/9.2

F49620-78-C-0016

UNCLASSIFIED

AFOSR-TR-79-1155

NL

2 OF 3

AD-A077351



4.4 Procedure Used in Conducting Erosive-Burning Test Firings

During the course of the erosive-burning test firing, a number of precautions were taken because of the complexity of the test rig setup and the possibility of an accident. A check list prescribing a systematic procedure for setting up each test firing was used. A copy of this check list and a sample data sheet are shown in Appendix E. Typically, two to three days were required to set up a test firing. Some of the requisites for preparing a test firing are described below.

- (1) Internal surfaces of the driver-motor star grain were spread with an igniter paste composed of potassium perchlorate (KClO_4), Boron (B), and Titanium (T_1) mixed in hexane. The advantage of using the igniter paste was its ability to spread the flame uniformly and rapidly, thus reducing the time interval of pressurization after ignition.
- (2) The test propellant was glued to the flat surface of the leading edge element with an epoxy containing Epon 828 (90%) and diethylene triamine (10%). Normally, 24 hours were required for the glue to dry and firmly hold the propellant on the leading edge. The test propellant was then shaped to the required dimensions by careful milling. Typical test propellant dimensions were length = 10.7 cm, width = 7.3 cm, and thickness = 1.75 cm. The leading edge portion of the propellant was tapered to ensure smooth development of a boundary layer. The trailing edge portion of the propellant was also tapered slightly to avoid any flow separation effect in the vicinity of the trailing edge. A little extra width beyond that of the leading edge width, was left for the propellant sample.

This was necessary in order to have good compression between the sacrificial plexiglass window and the propellant (see Appendix E). In this way, no combustion gases were able to penetrate between the propellant and the plexiglass window.

- (3) A thin layer of flame retardant (chloroflourocarbon, Halocarbon 25-5S) was also applied to the propellant's front and back surfaces which were in contact with the plexiglass window and the test chamber wall, respectively. The propellant compression and the use of flame retardant are essential to the experiment in order to prevent flame spreading between the contact surfaces. In a few of the earlier test firings, it was found that the high-temperature high-velocity combustion gases lifted off a small portion of the propellant from the leading edge (stagnation region); eventually, the resulting small crack became larger due to rapid flame-penetration of the crack. A small portion of the propellant leading edge was also covered with the flame retardant layer to avoid development of cracks.
- (4) A silicon-rubber insulation material was used to protect the transducer diaphragms from the hot gases. In addition to the water cooling, this gave additional thermal insulation to the transducers. Transducers were not mounted flush with the inner surface of the test chamber but were slightly recessed from it to provide additional thermal protection.
- (5) The contact surfaces of various components of the test rig were sealed by applying a layer of rubber based adhesive sealant (Permatex, No. 6BR). This was found to be very effective in achieving a good seal.

- (6) A pre-ignition test was made just before every actual test firing. A fuse wire was connected to the igniter wire, the high-speed movie camera was loaded with a dummy film, and various control switches were then activated in the same sequence as in an actual test firing. If the setup was appropriate, the fuse wire would burn, thus confirming the proper function of remotely controlled ignition circuit.
- (7) Four camera lights (two 1000-watts and two 650-watts) were used to illuminate the window and the propellant in the test chamber.
- (8) A 16 mm, 200-foot color film was used in each test firing. The film used was Kodak, Eastman Ektrachrome 7250 with ASA No. 400 Tungsten. The F-stop was set at 8.0 on the telescopic lens for all the tests conducted, and it was not necessary to push any F-stops during film processing.

CHAPTER 5

DISCUSSION OF RESULTS

5.1 Experimental Results

Before conducting erosive-burning test firings, a series of cold flow tests were performed to check the uniformity of the flow out of the rectangular convergent nozzle. Measurements were made with pitot-static probes at the exit plane of the convergent nozzle. The results of these measurements are plotted in Figure 20. This figure shows the measured velocity at various locations at the exit plane. The data consistently indicates the uniformity of the flow within the potential core over the major portion of the nozzle exit plane. The data also indicates that the velocity profile is independent of z coordinate; this implies that the nozzle geometry is adequate for providing a two-dimensional flow.

5.1.1 Discussion of Erosive-Burning Data

During each erosive-burning test firing, static pressure versus time measurements were recorded at three locations in the test rig. These locations were in the vicinity of the driver motor exit, leading edge, and exit nozzle. The photographic record of each test firing and pressure traces were synchronized, as discussed in section 4.1.2, by employing separate event markers (common time markers) to record the activation of the igniter circuit. In this way, the burning rate of the propellant sample and the chamber pressure were coordinated.

Typical pressure-time traces measured during the test firings with different exit-nozzle throat diameters are shown in Figures 21 through 23. Figure 21 shows the pressure-time record of the test firing

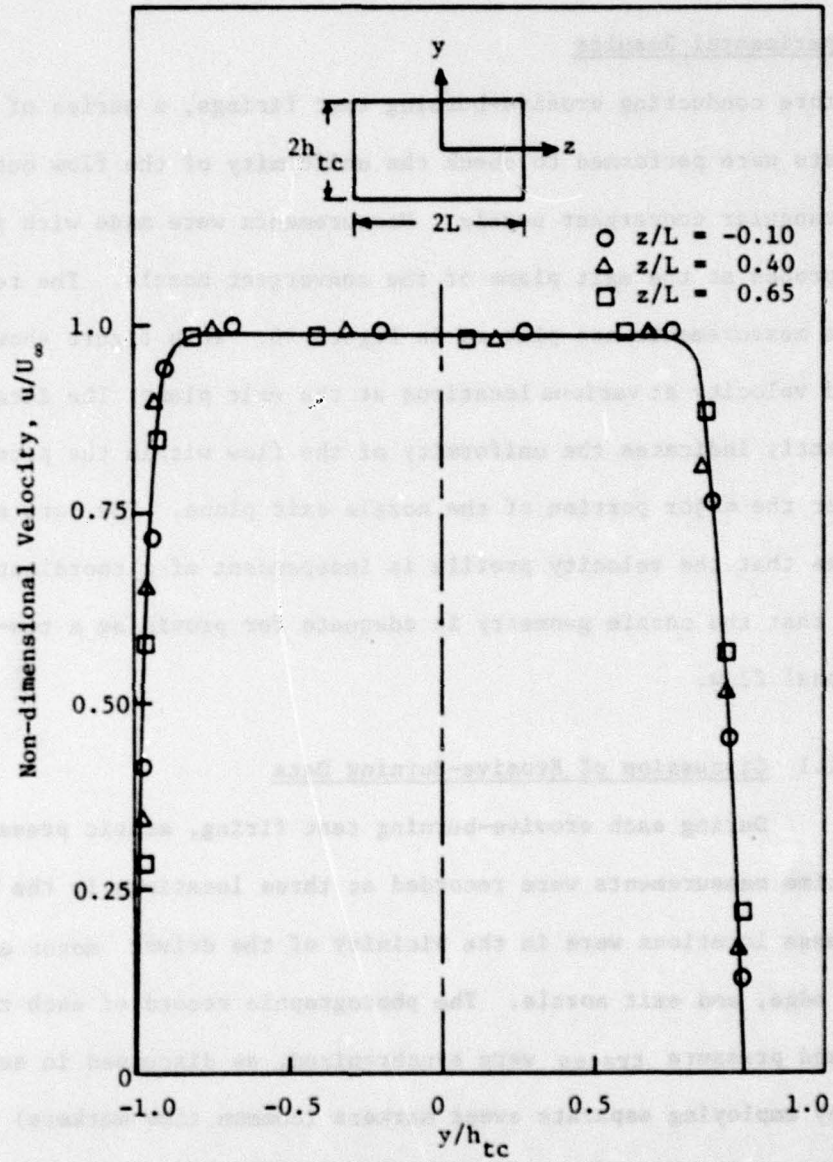


Figure 20 Cold Flow Test Results to Check the Uniformity of the Flow Out of the Rectangular Nozzle

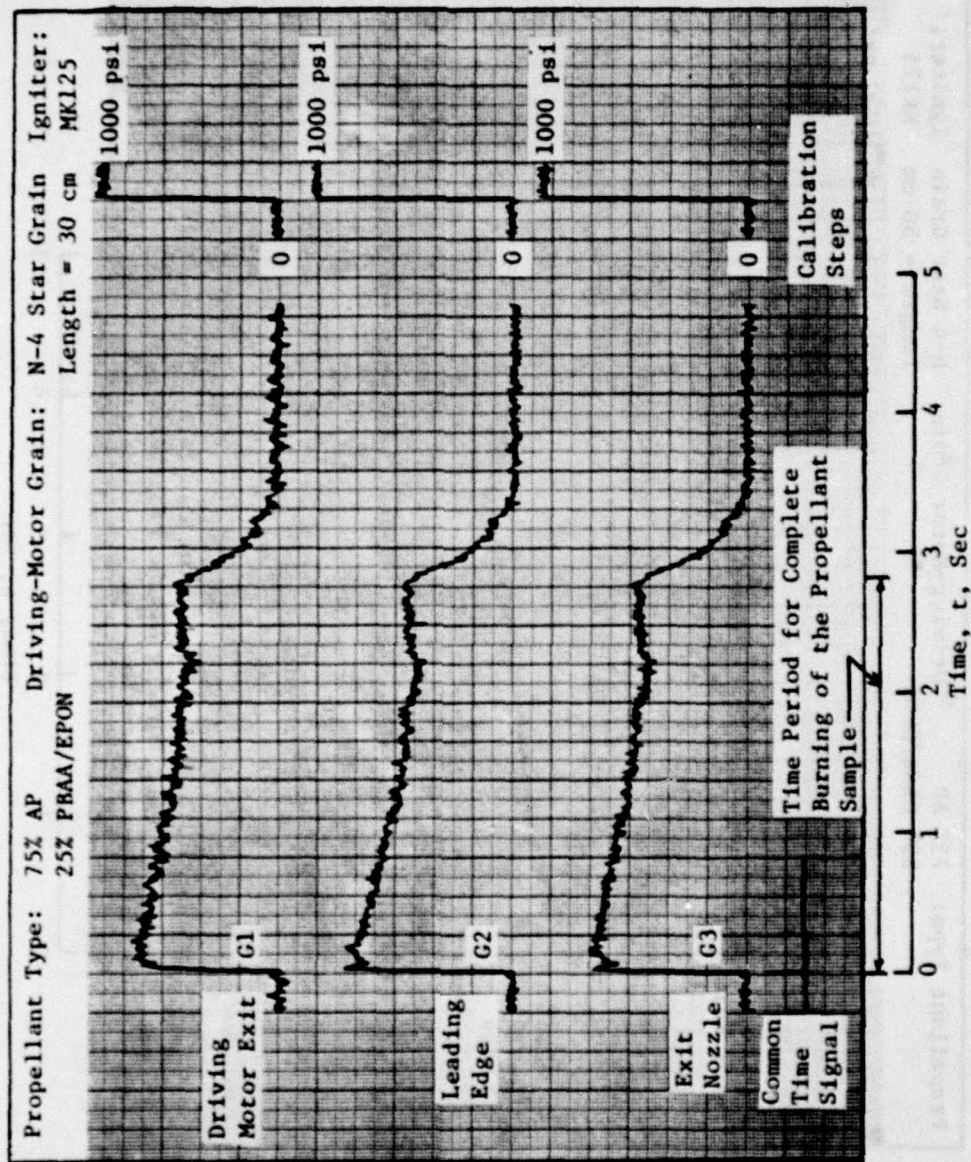


Figure 21 Measured Pressure-Time Traces in a Typical Erosive-Burning Test Firing with Exit-Nozzle Throat Diameter of 2.08 cm

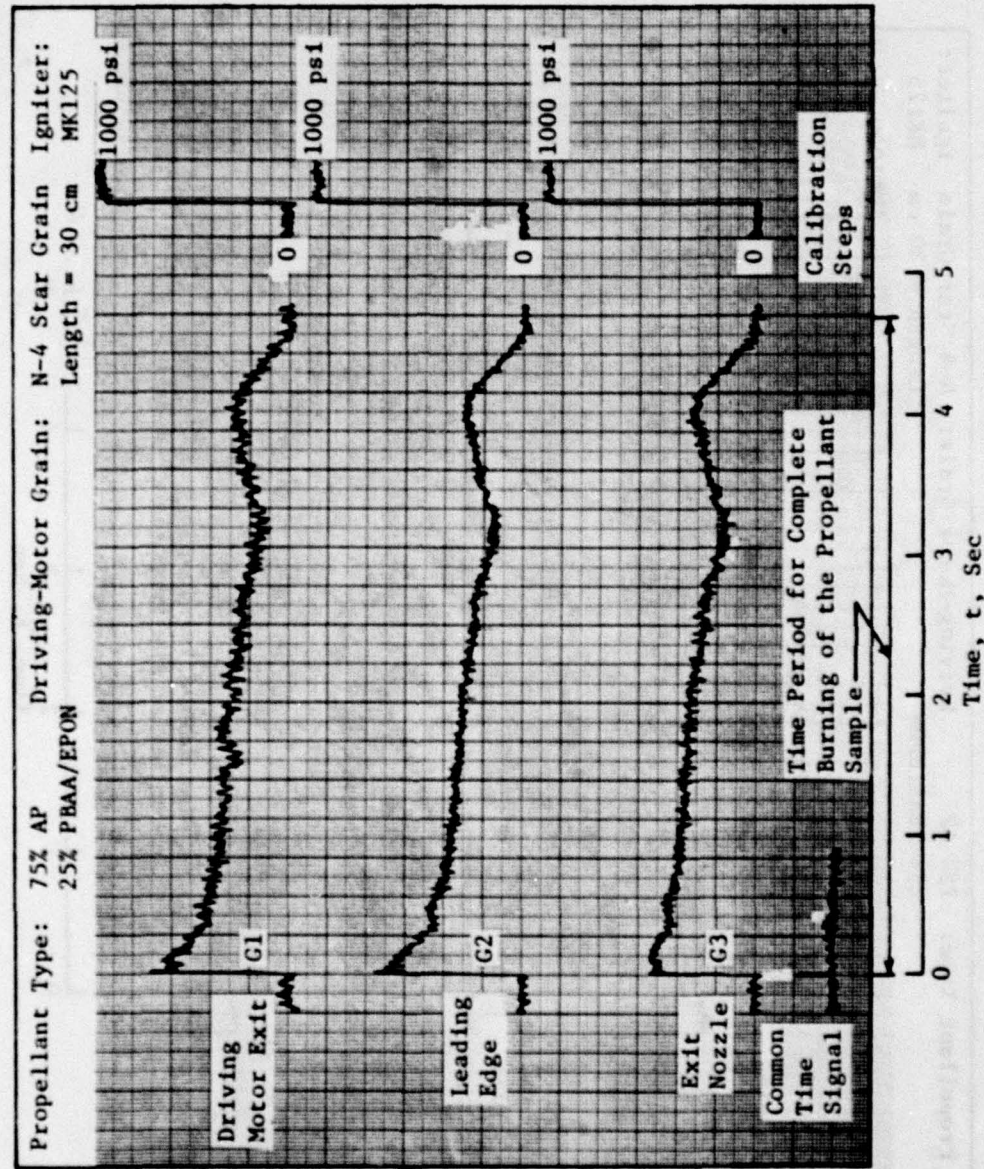


Figure 22 Measured Pressure-Time Traces in an Erosive-Burning Test Firing with Exit-Nozzle Throat Diameter of 2.42 cm

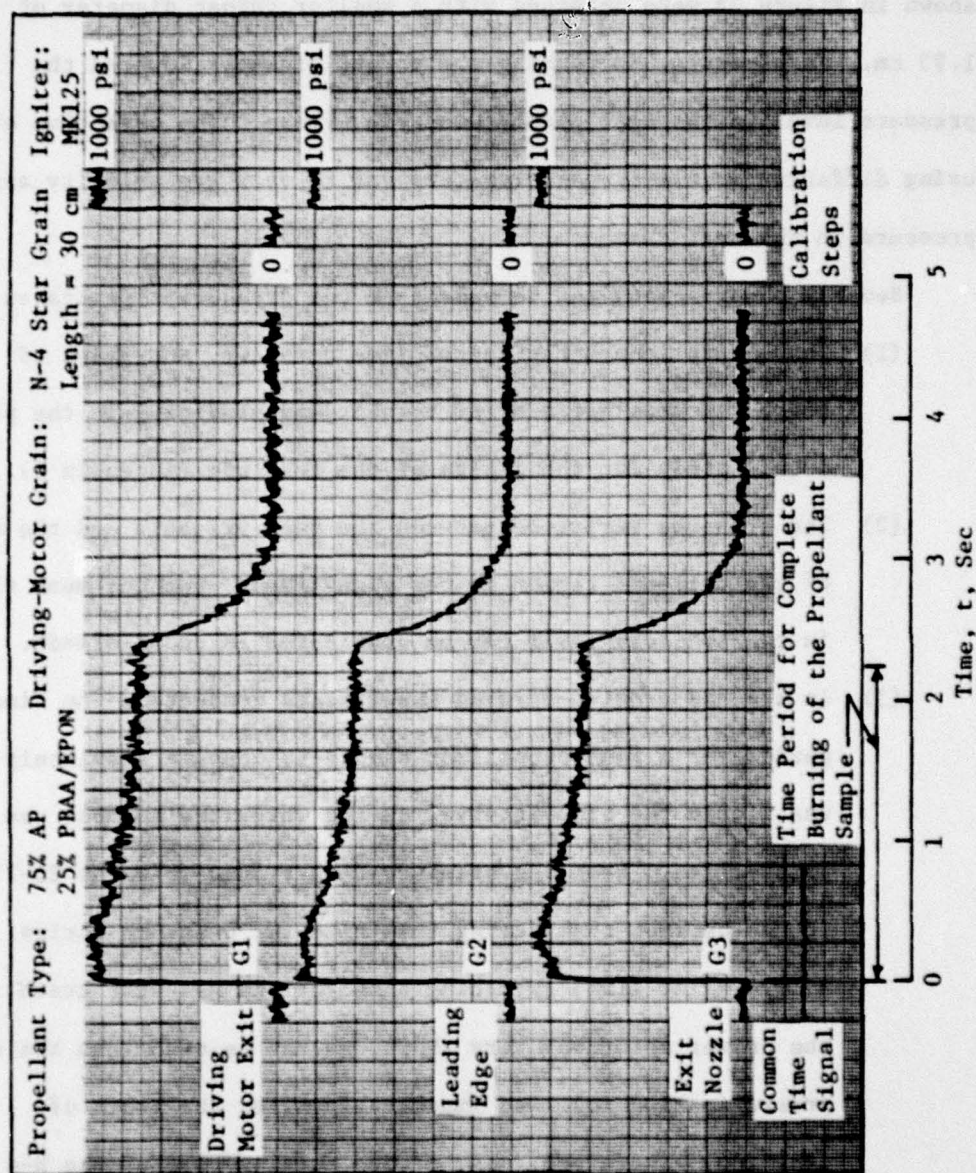


Figure 23 Measured Pressure-Time Traces in an Erosive-Burning Test Firing with Exit-Nozzle Throat Diameter of 1.93 cm

in which an exit nozzle with a medium throat diameter of 2.08 cm was used. Pressure-time traces shown in Figure 22 were obtained with an exit nozzle having a larger throat diameter of 2.42 cm, while those shown in Figure 23 were obtained with a smaller throat diameter of 1.93 cm. As expected, increasing the throat diameter lowered the pressure level in the test chamber and vice versa. The objective of using different nozzle-throat diameters was to vary gas velocity and pressure in the test chamber.

Several observations can be made from the pressure-time traces.

- (1) The general characteristics, time duration, and shape of the p-t traces are similar to what was predicted in the parametric study for the design of the test rig (Appendix D).
- (2) The pressure variation between the peak pressure and the start of the tail-off region is not significant, and the mean flow in the boundary layer can be considered as quasi-steady.
- (3) In all the erosive-burning experiments conducted, the time period for a test propellant sample to consume completely was within the time interval during which the chamber was pressurized. From the pressure-time traces (Figures 21-23), it can be seen that during this time the pressure varies slowly. The flame spreading time for the N-4 star grain in the driver motor was very short, as can be seen from the sharp pressurization followed immediately after the onset of ignition. Therefore, most of the burning time of the N-4 star grain was adequately utilized during the test run.
- (4) Common time signals shown in Figures 21-23 represent the instant at which remotely controlled ignition takes place.

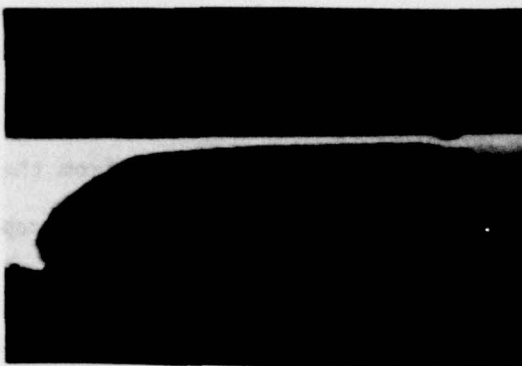
This time always coincides with the first discernible pressure rise in the test rig.

Erosive burning-rate data was obtained from the photographic record of a test firing. The AP/PBAA-EPON test propellant used in the present test firings had the following composition: 75% AP (average particle size 76 μm), 16.93% R-45M, 3.69% Diactyl Azelate, 3.38% Dimeryl Diisocyanate, and 1% graphite. Readings of instantaneous locations, y , of the burning test-propellant surface were obtained from the motion analyzer, as discussed in section 4.3.3. Three photographs showing the location of the test-propellant surface during a test firing at various times are shown in Figure 24. For each y reading, the corresponding time, t , was computed from the number of time markers on the film. A least-square polynomial fit through $y - t$ data was conducted to obtain an equation for $y(t)$. A typical case is shown in Figure 25, and this corresponds to a test firing for which the pressure-time traces are shown in Figure 23. The sum of squares of errors for this fit was very small (3.64×10^{-3}). The burning rate was calculated by differentiating the polynomial equation with respect to time. In this way, burning rate versus burning time data was obtained from all the test firings corresponding to pressure versus time data recorded from the pressure transducers.

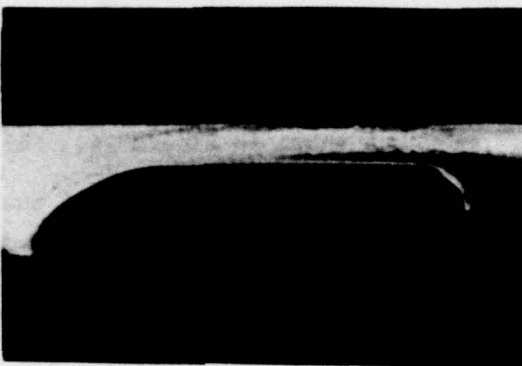
Average gas velocity in the test section, U_{ts} , over the propellant surface was found from the following equation (see Appendix F).

$$U_{ts} = \left(\frac{A_{th}}{A_{ts}} \right) \sqrt{T_0} \left(\gamma R \left(\frac{2}{\gamma+1} \right)^{\frac{\gamma+1}{\gamma-1}} \right)^{1/2} \left(1 + \frac{\gamma-1}{2} M_{ts}^2 \right)^{\frac{1}{\gamma-1}} \quad (84)$$

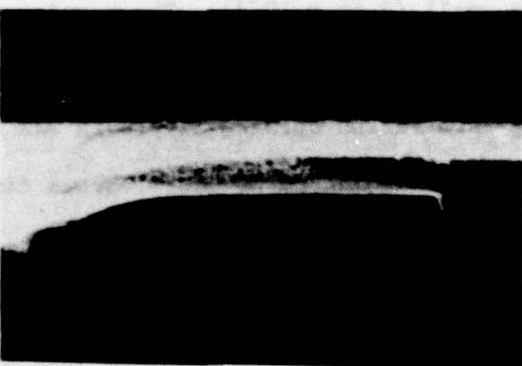
where A_{ts} is the flow cross-sectional area over the propellant test sample, A_{th} is the throat area of the exit nozzle, γ is the ratio of



Time = 0 Sec



Time = 1.0 Sec



Time = 1.87 Sec

Figure 24 Photographs Showing the Location of the Test-Propellant Surface at Various Times During a Test Firing

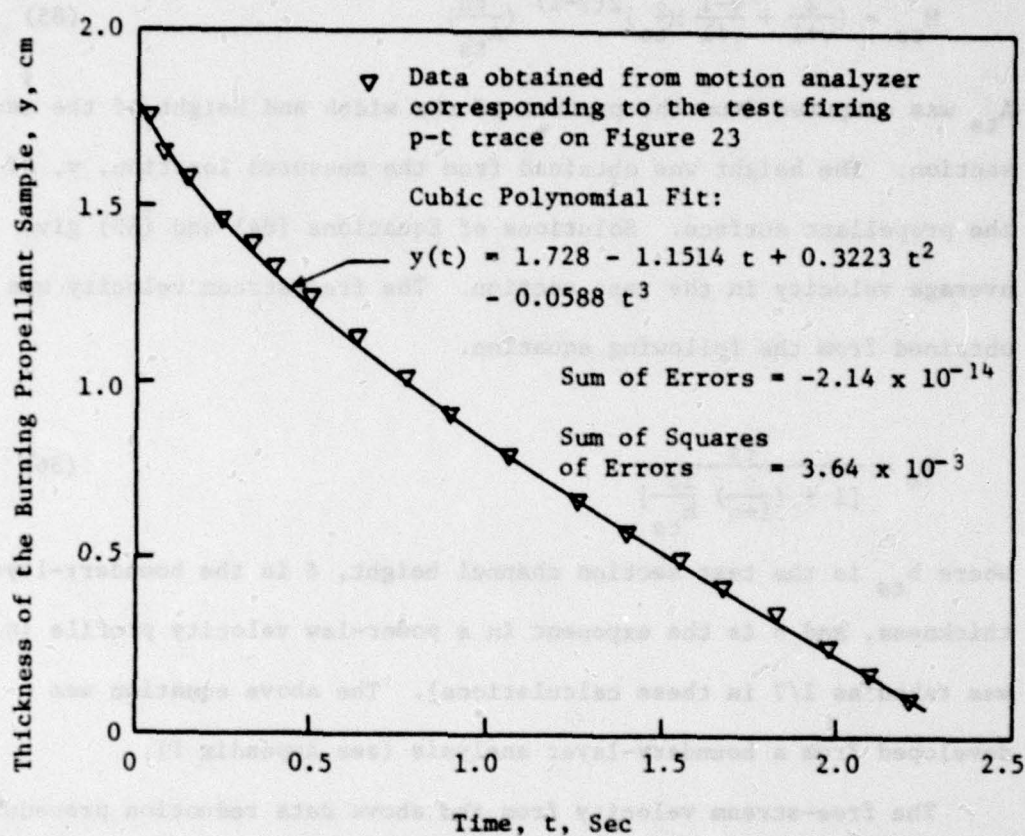


Figure 25 Least-Square Polynomial Fit to the Measured y versus t Data

specific heats, R is the gas constant of the combustion gases, M_{ts} is the average Mach number of the combustion gases in the test section, and T_0 is the stagnation temperature of the combustion gases. The Mach number was calculated from the following equation (see Appendix F).

$$M_{ts} = \left(\frac{2}{\gamma+1} + \frac{\gamma-1}{\gamma+1} M_{ts}^2 \right)^{\frac{\gamma+1}{2(\gamma-1)}} \left(\frac{A_{th}}{A_{ts}} \right) \quad (85)$$

A_{ts} was computed from the product of the width and height of the test section. The height was obtained from the measured location, y , of the propellant surface. Solutions of Equations (84) and (85) give average velocity in the test section. The free-stream velocity was obtained from the following equation.

$$U_{\infty} = \frac{U_{ts}}{\left[1 + \left(\frac{\eta}{1+\eta} \right) \frac{2\delta}{h_{ts}} \right]} \quad (86)$$

where h_{ts} is the test section channel height, δ is the boundary-layer thickness, and η is the exponent in a power-law velocity profile (η was taken as $1/7$ in these calculations). The above equation was developed from a boundary-layer analysis (see Appendix F).

The free-stream velocity from the above data reduction procedure, the burning rate obtained through a polynomial fit, and the measured pressure for the erosive test firings are tabulated in Appendix G.

It may be pointed out that the accuracy of the measured burning rate depends on the accuracy of the measurement of the location of the burning propellant surface. The measurements were taken with a motion analyzer capable of measuring line resolution to within 0.001 inch and at an average time interval of 0.01 seconds. The error introduced in evaluating the burning rate is less than 3%. No error is expected

in the calculation of the time interval between the film readings because the time markers were put on the film at a precisely known frequency.

The effect of radiation on the erosive burning-rate was assumed negligible (assumption 2 in section 2.2). An estimate of the radiation from the propellant surface was found to be about 2% of the convective gas-to-solid heat flux (assuming the emissivity of 0.75 and surface temperature of 1000 K). An estimate was also made of the gas radiation flux to the propellant surface. The major gas components in this calculation were CO , CO_2 and H_2O , which correspond to the exhaust-gas composition of the N-4 star grain (see Table 3). The values of emissivities of these components at a pressure of 60 atm and a temperature of 2258 K were taken from Reference 76. The mean path length for this calculation was assumed equal to the height of the test section above the test-propellant sample. The contribution of the gas radiation was estimated at 6% of the convective gas-to-solid heat flux obtained from the boundary-layer calculation at a free-stream velocity of 400 m/s. This contribution, however, diminishes as the free-stream velocity increases.

5.1.2 Comparison of Theoretical Results with Experimental Data

In order to calculate burning rates from the theoretical model, pressure and free-stream velocity must be supplied as an input. For this purpose, a number of average values of pressures were taken over short intervals of time from the pressure-time traces of the test firings. At each pressure, a number of computer calculations were performed at various free-stream velocities. The velocity range was obtained from the burning rate and pressure-velocity data (Appendix G).

The results of the calculations are plotted in Figure 26, which shows the variation of total burning rate with free-stream velocity at pressures of 7.24, 4.6 and 3.0 MPa. A number of experimental data points are also shown in Figure 26. The agreement between the predicted and measured burning rates is very good for all the pressures considered. The slope of the burning rate versus velocity curves decreases with the decrease in pressure. At the same time, the burning rate at lower pressure changes very slowly at low velocities (close to 200 m/sec).

A comparison of the theoretically calculated burning rates with the experimental data of Marklund and Lake (26) was also made. They measured the burning rates of AP/Polysulfide propellant samples located in a rectangular channel. The pressure pickup method was used to measure the burning rates at pressures of 50 and 100 atmospheres. Figure 27 shows the predicted burning rates for AP/Polysulfide propellant at pressures of 50 atm and 100 atm, and the results are compared with Marklund and Lake's data. The results were computed at the same Reynolds number as in the experiments described by Marklund and Lake (26). The comparison indicates that the agreement between the theoretical and experimental results is very close, except at low velocities. Lengellé's (33) predictions (using an integral method) also did not match well with Marklund and Lake's (26) data at low velocities.

A number of values of measured total burning rates are shown for different pressures and velocities in Figure 28. Because of the large variations in pressures and velocities, grouping the data points within certain pressure ranges (as given in the form of Figure 28) is not desirable. Consequently, a correlation of the burning rate as a

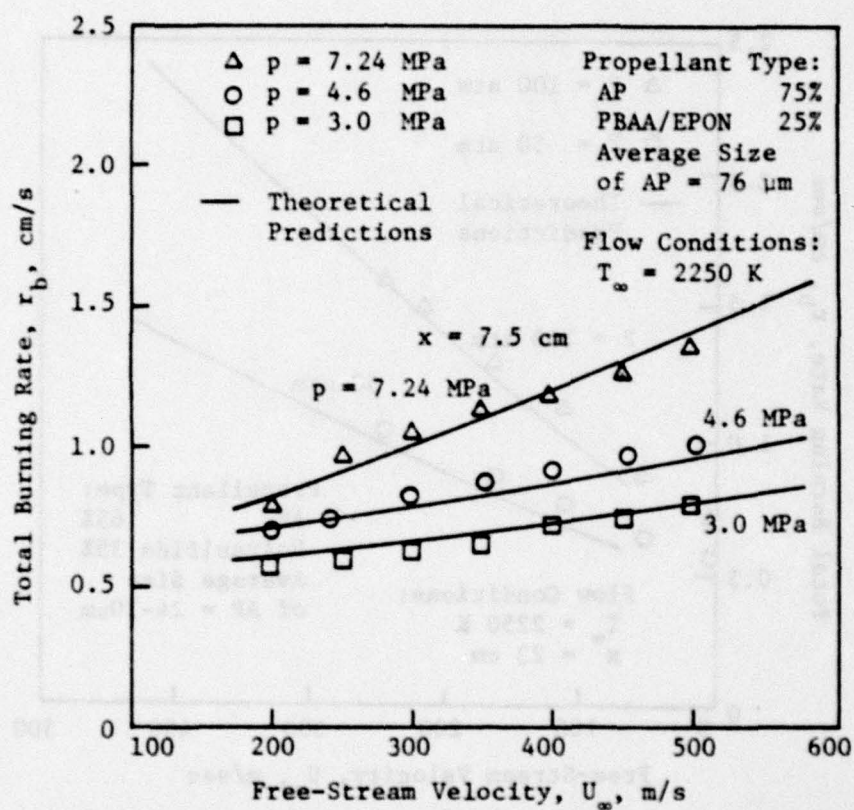


Figure 26 Comparison of the Predicted Burning Rates with the Experimental Data at Various Pressures and Free-Stream Velocities

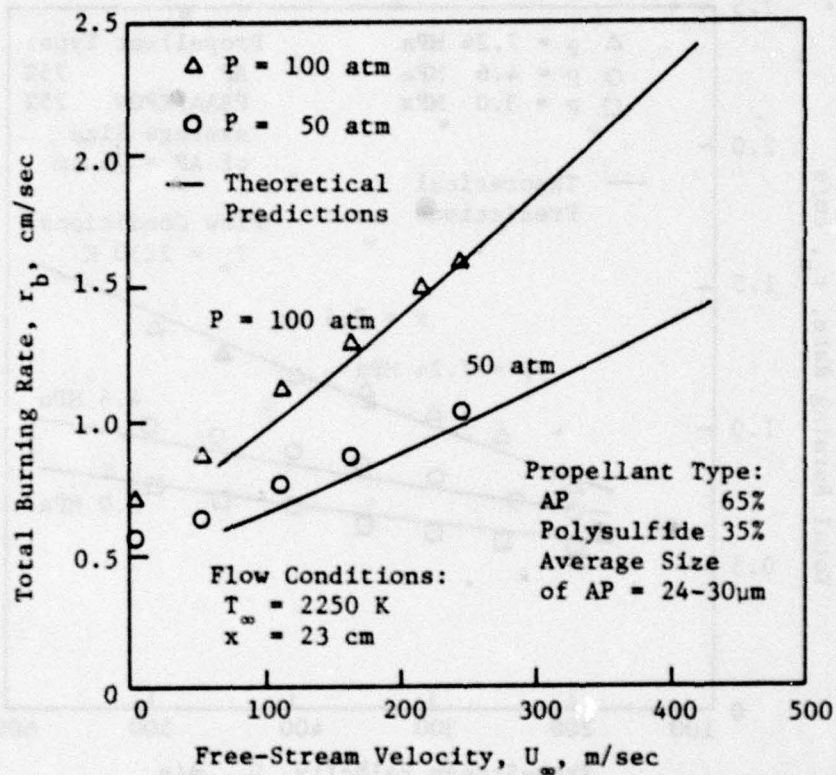


Figure 27 Comparison of the Predicted Burning Rates with the Experimental Data of Marklund and Lake

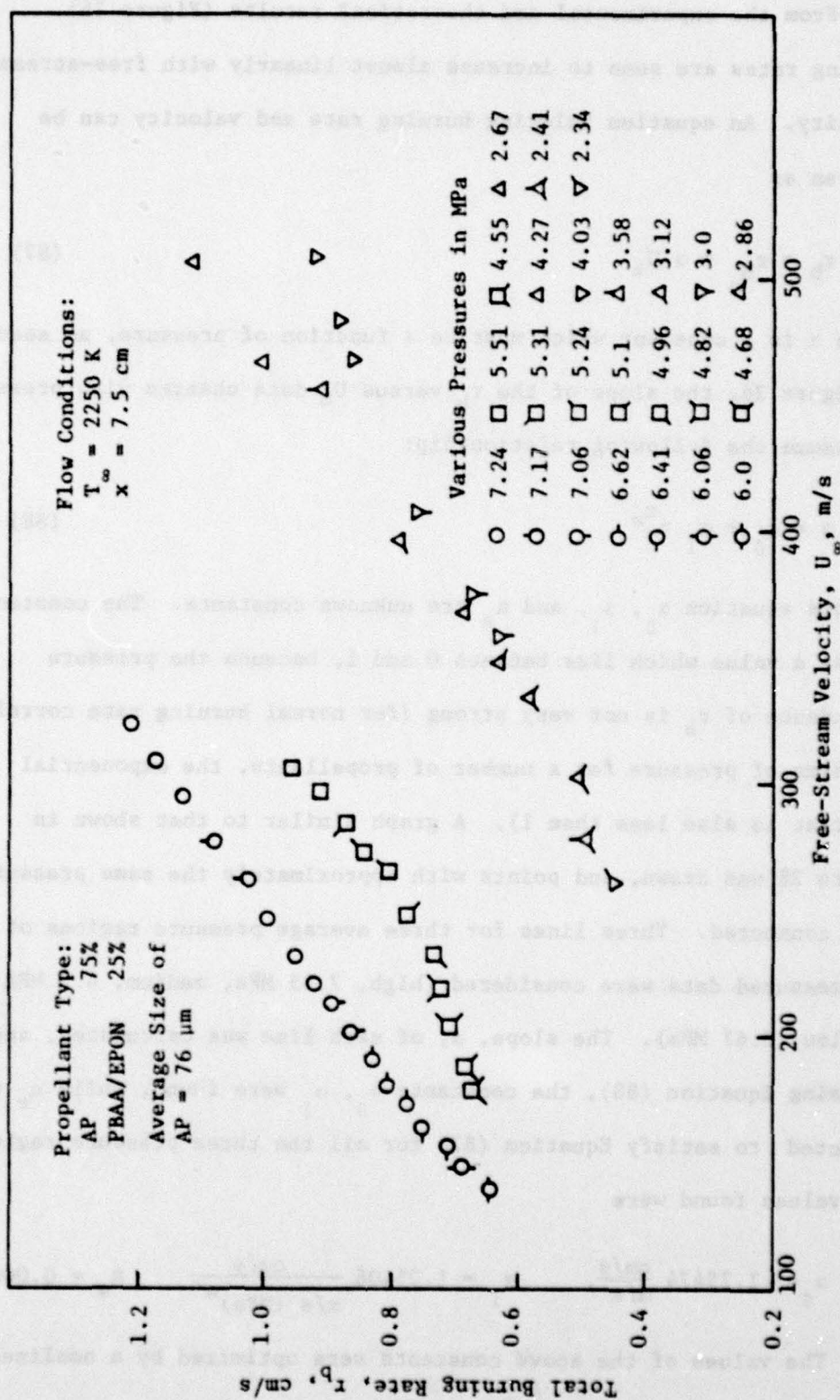


Figure 28 Experimental Data for Total Burning Rates at Various Pressures and Free-Stream Velocities

function of pressure and free-stream velocity was developed as follows.

From the experimental and theoretical results (Figure 26), burning rates are seen to increase almost linearly with free-stream velocity. An equation relating burning rate and velocity can be written as

$$r_b = r_{b_0} + \alpha U_\infty \quad (87)$$

Where α is a constant which must be a function of pressure, as seen in Figure 26, the slope of the r_b versus U_∞ data changes with pressure. We assume the following relationship:

$$\alpha = \alpha_0 + \alpha_1 p^{n_e} \quad (88)$$

In this equation α_0 , α_1 , and n_e are unknown constants. The constant n_e has a value which lies between 0 and 1, because the pressure dependence of r_b is not very strong (for normal burning rate correlations in terms of pressure for a number of propellants, the exponential constant is also less than 1). A graph similar to that shown in Figure 28 was drawn, and points with approximately the same pressures were connected. Three lines for three average pressure regions of the measured data were considered (high, 7.15 MPa, medium, 4.5 MPa, and low, 2.67 MPa). The slope, α , of each line was calculated, and then by using Equation (88), the constants α_0 , α_1 were found, while n_e was selected to satisfy Equation (87) for all the three pressure regions. The values found were

$$\alpha_0 = -1.25474 \frac{\text{cm/s}}{\text{m/s}}, \quad \alpha_1 = 1.25406 \frac{\text{cm/s}}{\text{m/s (MPa)}^{n_e}}, \quad n_e = 0.001$$

The values of the above constants were optimized by a nonlinear

regression analysis of the experimental data for burning rate, free-stream velocity, and pressure. The regression analysis was performed with the NLIN2 computer program of the Share Program Library. The model supplied to the NLIN2 program was represented by the following correlation:

$$r_e = \alpha_0 U_\infty + \alpha_1 U_\infty p^{n_e} \quad (89)$$

This equation is obtained from Equations (87) and (88), while r_e is the erosive-burning rate component of the total burning rate, r_b , of a solid propellant. The optimized constants obtained from the regression analysis are

$$\alpha_0 = -1.25463 \text{ (cm/s)/(m/s)}$$

$$\alpha_1 = 1.25417 \text{ (cm/s)/(m/s)/(MPa)}^{n_e}$$

$$n_e = 0.000871$$

Using the strand-burning-rate law, $r_{b_o} = a' p^{n'}$, and Equations (87) and (88), the correlation represented by Equation (89) can be written in the following convenient form:

$$\frac{r_b}{r_{b_o}} = 1 + \left[\frac{K_1 + K_2 p^{n_e}}{p^{n'}} \right] U_\infty \quad (90)$$

where

$$K_1 = -5.11737 \text{ (MPa)}^{n'} / \text{(m/s)}$$

$$K_2 = 5.11547 \text{ (MPa)}^{n'-n_e} / \text{(m/s)}$$

$$a' = 0.2452 \text{ (cm/s)/(MPa)}^{n'}$$

$$n' = 0.41$$

The correlation given by Equation (90) represents, within limits of available data, the effect of free-stream velocity and pressure on the burning rate of the AP/PBAA-EPON propellant studied. This correlation is represented by a 45° line on a $\frac{r_b}{r_{b0}}$ versus $1 + \left(\frac{K + K p^{n_e}}{p^n} \right) U_\infty$ plot in Figure 29. The close agreement between the data points and their trend with the 45° line in Figure 29 indicates that the correlation shown by Equation (90) is suitable to represent the burning-rate data obtained in this study.

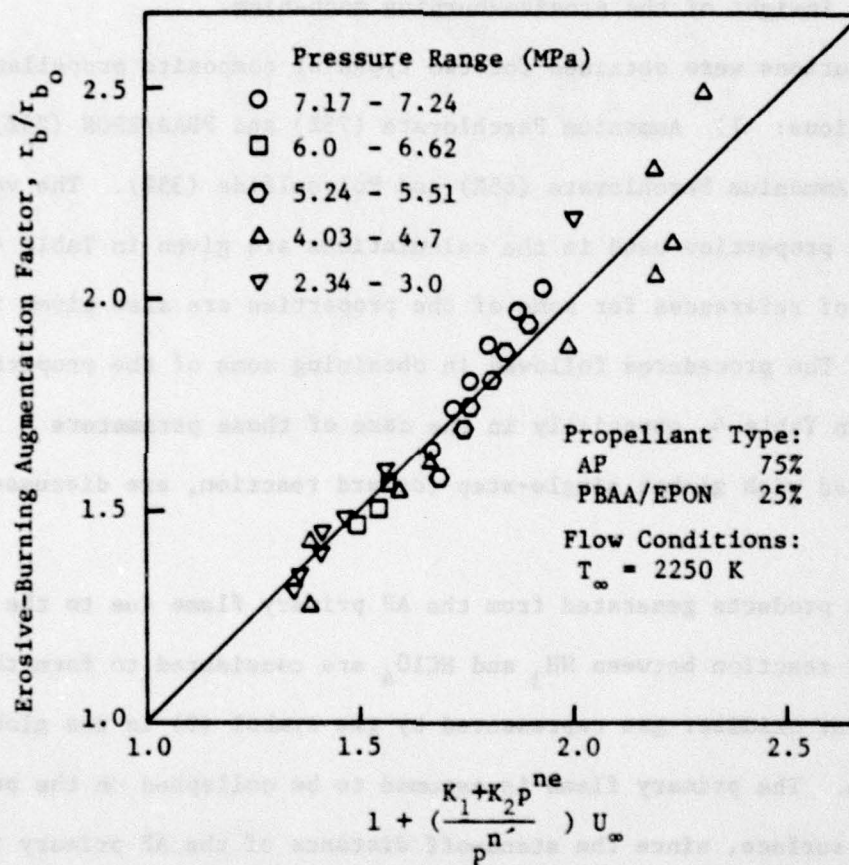


Figure 29 Experimental Data for Erosive-Burning Augmentation Factor Correlated with Pressure and Free-Stream Velocity

5.2 Boundary-Layer Solutions of the Theoretical Model

The purpose in presenting the boundary-layer solutions of various variables (\bar{u} , \bar{Y}_O , \bar{Y}_F , \bar{T} , K , etc.) is to further understand and identify a possible erosive-burning mechanism. There is no experimental data available for the distribution of these variables in a chemically reacting turbulent boundary layer; theoretical solutions help to provide a better insight of the erosive-burning mechanism.

Solutions were obtained for two types of composite propellant compositions: 1) Ammonium Perchlorate (75%) and PBAA/EPON (25%), and 2) Ammonium Perchlorate (65%) and Polysulfide (35%). The various physical properties used in the calculations are given in Table 4. Sources of references for some of the properties are also given in Table 4. The procedures followed in obtaining some of the properties listed in Table 4, especially in the case of those parameters associated with global single-step forward reaction, are discussed below.

The products generated from the AP primary flame due to the chemical reaction between NH_3 and HClO_4 are considered to form the equivalent oxidizer gas represented by the symbol (O) in the global reaction. The primary flame is assumed to be collapsed on the propellant surface, since the stand-off distance of the AP primary flame is extremely small (in the order of 1 μm) at normal rocket operating pressures. The heat of formation of the equivalent oxidizer gas was obtained from the chemical equilibrium calculation using the CEC72 program (79). The inputs necessary for this calculation are the heat of formation of the solid AP (-70, 690 cal/mole) and the gas pressure.

It is assumed that the equivalent gaseous fuel, represented by the

Table 4

Properties Used in Theoretical Calculations

Property	Dimensions	Propellant Type:			
		AP	75%	AP	65%
		PBAA/EPON	25%	Polysulfide	35%
a'	$\text{cm/s}/(\text{MPa})^{n'}$	0.2452		0.3642	
A_s	m/s	5.65		25289.0	
A^+	-----	26		26	
C_s	Kcal/Kg-K	0.3		0.38	
C_p	Kcal/Kg-K (all species)	0.3		0.3	
E_{as}	Kcal/mole-K	15		30	
$\Delta h^\circ_{f,F}$	Kcal/Kg	55.93		-0.42	
$\Delta h^\circ_{f,O}$	Kcal/Kg	-942.0		-936.6	
$\Delta h^\circ_{f,P}$	Kcal/Kg	-1137.3		-1310.5	
k	-----	0.41		0.41	
n'	-----	0.41		0.276	
Pr	-----	$\frac{\gamma}{1.77\gamma - 0.45}$ (Svehla's Eq., Ref. 77)		Same Equation	
Pr_t	-----	0.9 (Ref. 78)		0.9	
\bar{Q}_s	Kcal/Kg	-250.0 (Ref. 77)		-240.0	
$Sc=Pr$	-----	0.708		0.708	

Table 4 (continued)

Property	Dimensions	Propellant Type:	
		AP PBAA/EPON	75% 25% AP Polysulfide 65% 35%
$Sc_t = Pr_t$	-----	0.9	0.9
T_{pi}	K	298	298
\bar{T}_{ps}	K	800	800
W_F	Kg/Kmole	30	30
W_O	Kg/Kmole	27.893	27.949
W_P	Kg/Kmole	20.381	25.69
Y_{FS}	-----	0.25	0.35
Y_{OS}	-----	0.75	0.65
γ	-----	1.26	1.26
λ	Kcal/m-s-K	$C_p \mu / Pr$	same equation
μ_k	Kg/m-s	$8.7 \times 10^{-8} \sqrt{W_k} T^{0.65}$	same equation
ν_F	moles	1	1
ν_O	moles	3.2266	1.9935
ν_P	moles	5.888	3.3366
ρ_s	Kg/m ³	1600	1660

symbol (F), is formed by the ablation of the solid fuel-binder due to random scission/systematic unzipping of the polymer chain, as discussed in reference 44. The heat of formation of the equivalent fuel gas was calculated from the difference between the heat of formation of the solid fuel binder and the heat of decomposition. The heat of formation for PBAA-EPON ($C_{6.88} H_{10.1} O_{0.27} N_{0.26}$) is -12,000 cal/mole, and for Polysulfide ($C_5 H_{10} O_2 S_2$) is -88,080 cal/mole. The heat of formation of the equivalent product gases, represented by symbol (P), was obtained from the overall chemical equilibrium calculation of AP and fuel-binder combustion. The average molecular weight of the product gases was also determined from this calculation. The stoichiometric coefficients v_O , v_F , and v_P were determined from the mass balance of the global reaction for a given propellant of known initial oxidizer-to-fuel ratio.

The procedure used to calculate the pre-exponential factor in the Arrhenius law of surface pyrolysis, A_s , is as follows: 1) Adopt the values of the activation energy, E_{as} (typical values of 15 and 30 Kcal/mole as suggested in Reference 44); 2) find the normal burning rate, r_{b_o} , from the formula based on GDF theory (44) or a $p^{n'}$ relation; 3) from GDF calculations, find the value of surface temperature, T_{ps} , which depends on the pressure under which the propellant combustion takes place; and find A_s from Equation (48) after utilizing E_{as} , r_{b_o} and T_{ps} .

Figure 30 shows the calculated distributions over the propellant surface of turbulent kinetic energy, Reynolds stress, and time-averaged velocity in the chemically reacting turbulent boundary layer considered. The velocity profile near the wall (solid propellant surface) is less

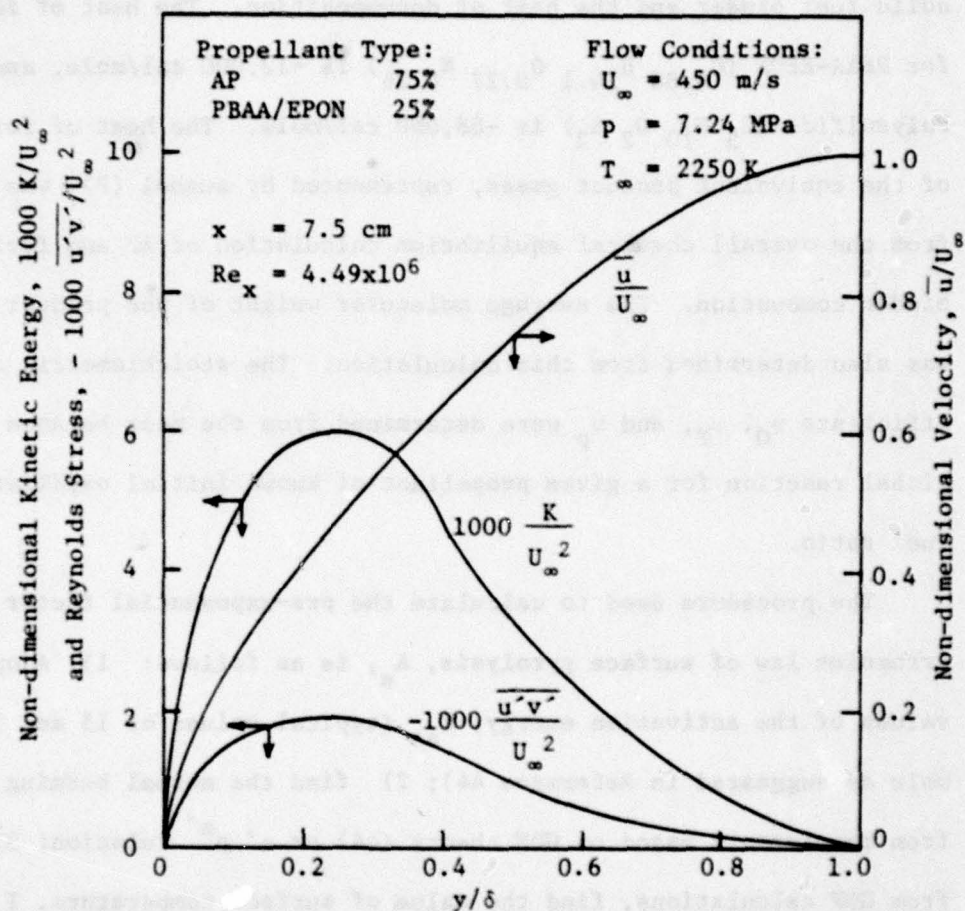


Figure 30 Calculated Distributions of Turbulent Kinetic Energy, Reynolds Stress and Velocity

steep than that in a conventional flat-plate turbulent boundary layer (Figure 10); this is due to the strong surface blowing rates caused by the burning of the solid propellant. Turbulent kinetic energy, K , peaks near $y/\delta = 0.25$. This location is farther from the wall than that in a conventional boundary layer. Again, this can be attributed to strong surface blowing and also to the decrease in mean velocity-profile gradient which is responsible for the production of K . In most of the boundary layer, the Reynolds stress is about one-third the value of turbulent kinetic energy. This is a general characteristic of most flat-plate turbulent boundary layers.

Calculated temperature distributions for different free-stream velocities of the boundary layer are shown in Figure 31, and for the near-wall region in Figure 32. The temperature rises rapidly from its value at the propellant surface and then gradually approaches the free-stream gas temperature at the edge of the boundary layer. The temperature distribution also humps at a location close to the propellant surface. Both the rapid rise and hump in the temperature distribution are believed to be caused by high rates of chemical reactions occurring close to the propellant surface. This is evident from the results plotted in the near-wall region in Figure 33 for the distributions of gas-phase heat generation rate, and mass fractions of oxidizer and fuel species. The heat generation rate in the gas phase peaks close to the wall around $20 \mu\text{m}$, indicating that the reaction region is close to the propellant surface. This is also consistent with results in the same figure, which show a rapid drop in the average mass fractions of oxidizer and fuel species. From the results of Figures 31 and 32, we notice that the temperature gradient becomes steeper at the surface

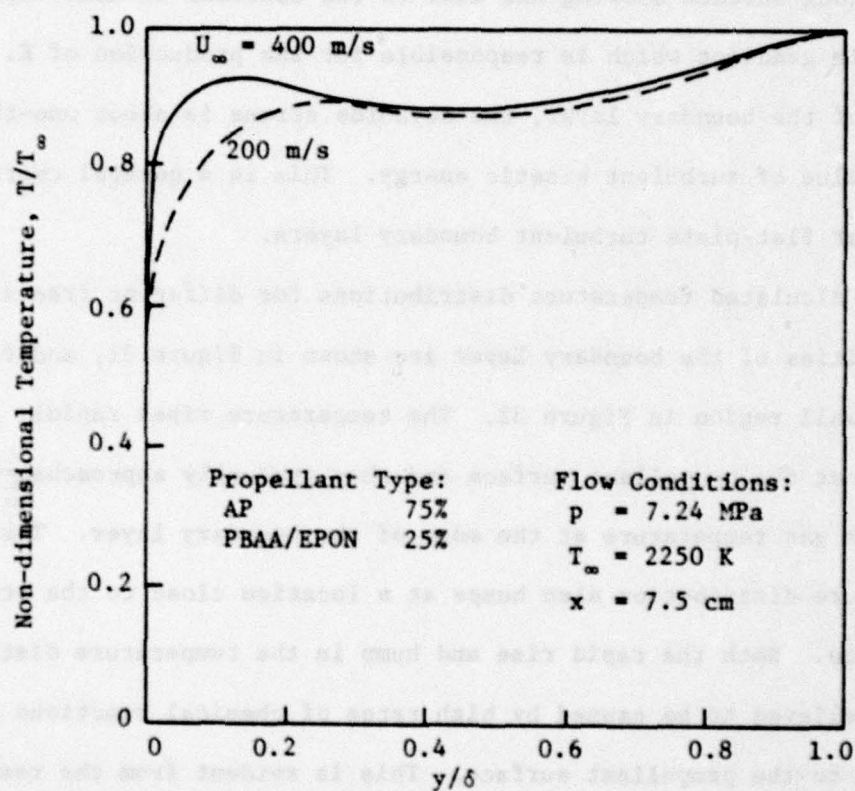


Figure 31 Calculated Temperature Distributions for Different Free-Stream Velocities

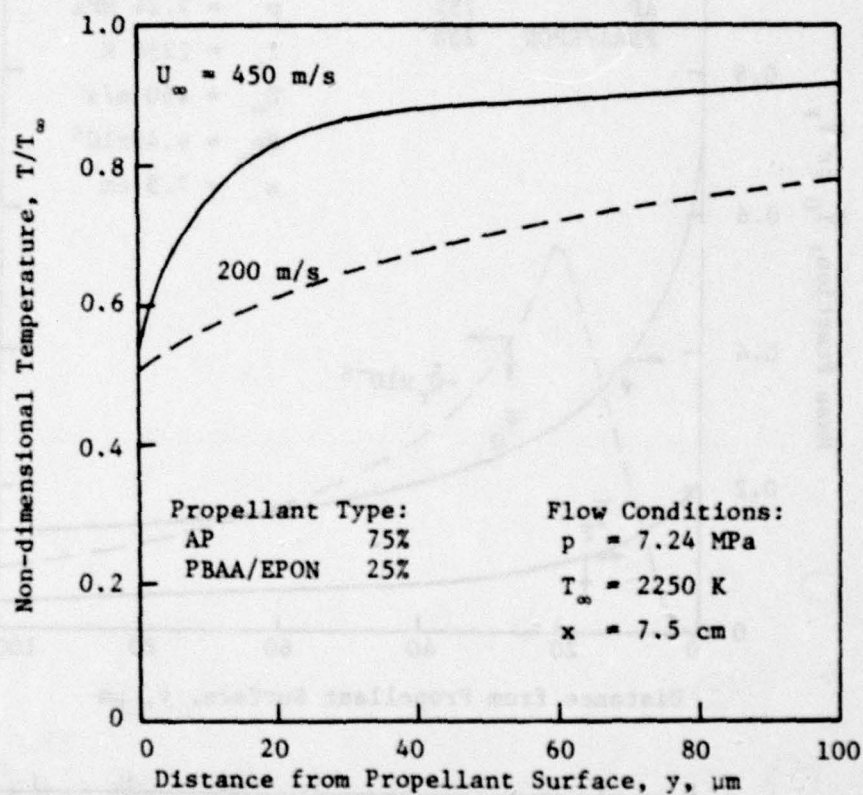


Figure 32 Calculated Temperature Distributions for Different Free-Stream Velocities in the Near-Wall Region

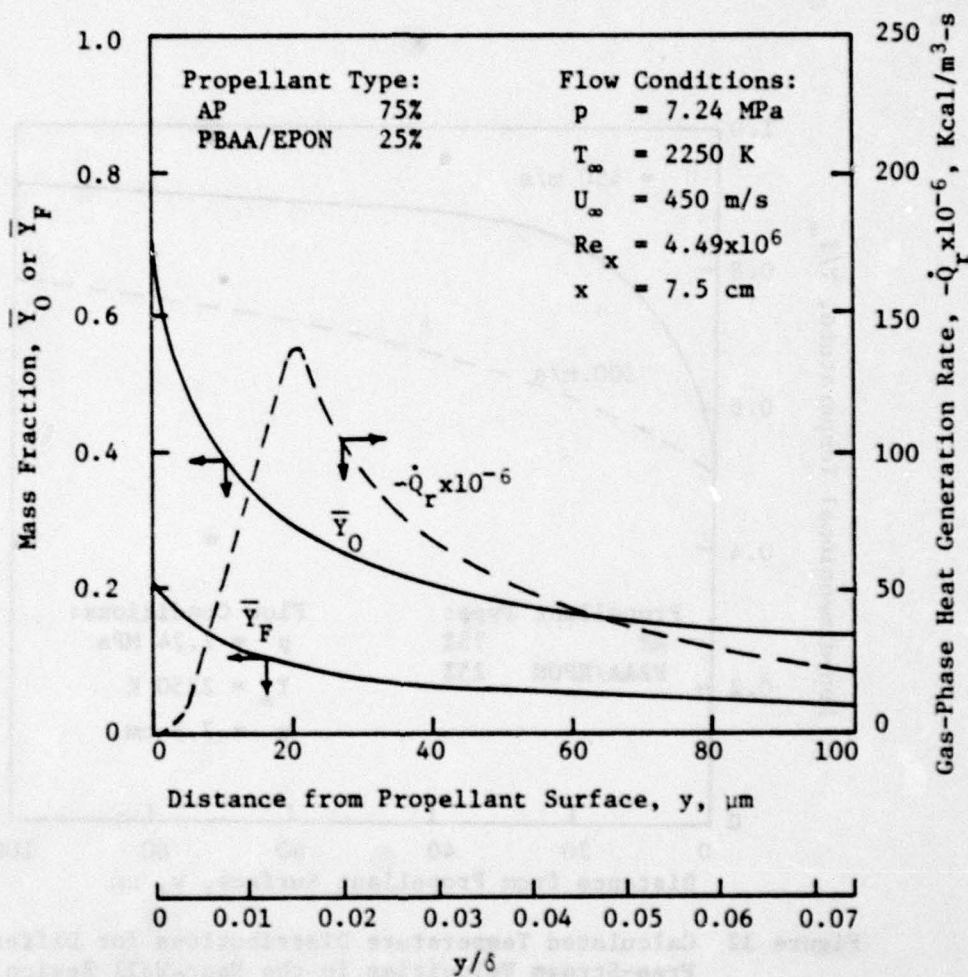


Figure 33 Calculated Distributions of Oxidizer and Fuel Mass Fractions, and the Gas-Phase Heat Generation Rate in the Near-Wall Region

as the free-stream velocity increases from 200 m/s to 450 m/s. This effect can be explained by the results plotted in Figure 34 which shows the effect of free-stream velocity on the location of the peak turbulence intensity and on the gas-to-solid heat flux. The increase in free-stream velocity brings the location of the peak turbulence intensity closer to the propellant surface. This has a significant effect on the flow field near the propellant surface. The closeness of the peak turbulence intensity to propellant surface means that the turbulent eddies with high frequencies also come closer to the propellant surface. This causes an increase in the mixing rate of oxidizer and fuel species, therefore increasing the gas-phase reaction rate and bringing it closer to the propellant surface. As shown in Figure 35, the peak value of the rate of heat generation in the gas phase, due to chemical reactions, increases with increasing velocity, and the location of this peak becomes closer to the propellant surface. Therefore, the level of temperature distribution increases, which in turn increases the gas-to-solid heat flux as plotted in Figure 34. The increased heat flux eventually increases the erosive-burning augmentation factor (r_b/r_{b_0}), as shown in Figure 35.

Increase in the free-stream velocity also increases the turbulent heat flux in the gas phase; this result is shown in Figure 36. The increase is caused by the increase in turbulent viscosity and temperature gradient, as can be seen from Equation (26). Turbulent viscosity distribution plotted in Figure 37 also increases with the increase in free-stream velocity. Therefore, the gas-to-solid heat transfer rate can also increase (see Figure 34) due to the increase in turbulence heat flux. It may be pointed out that negative values of

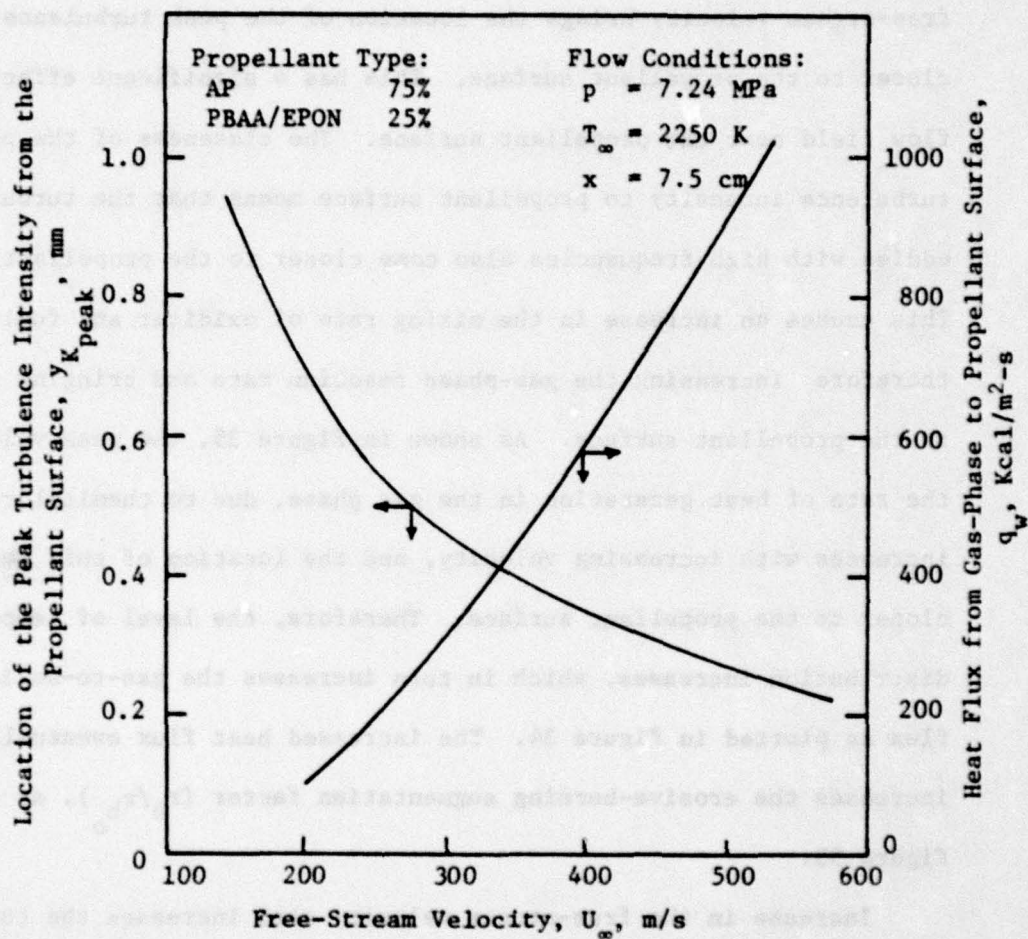


Figure 34 Effect of Free-Stream Velocity on the Location of the Peak Turbulence Intensity and the Gas-to-Solid Heat Flux

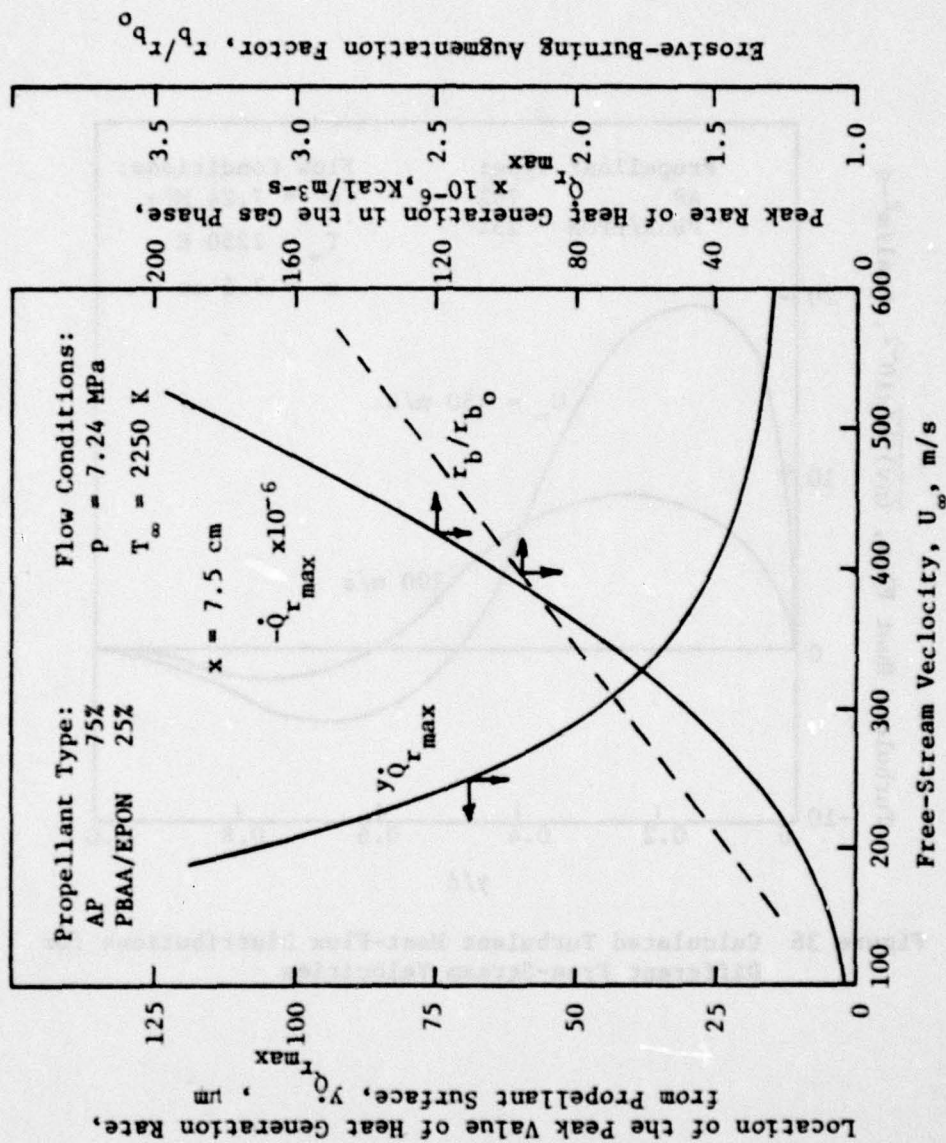


Figure 35 Effect of Free-Stream Velocity on the Peak Rate of Heat Generation in the Gas Phase, its Location from the Propellant Surface, and the Erosive-Burning Augmentation Factor

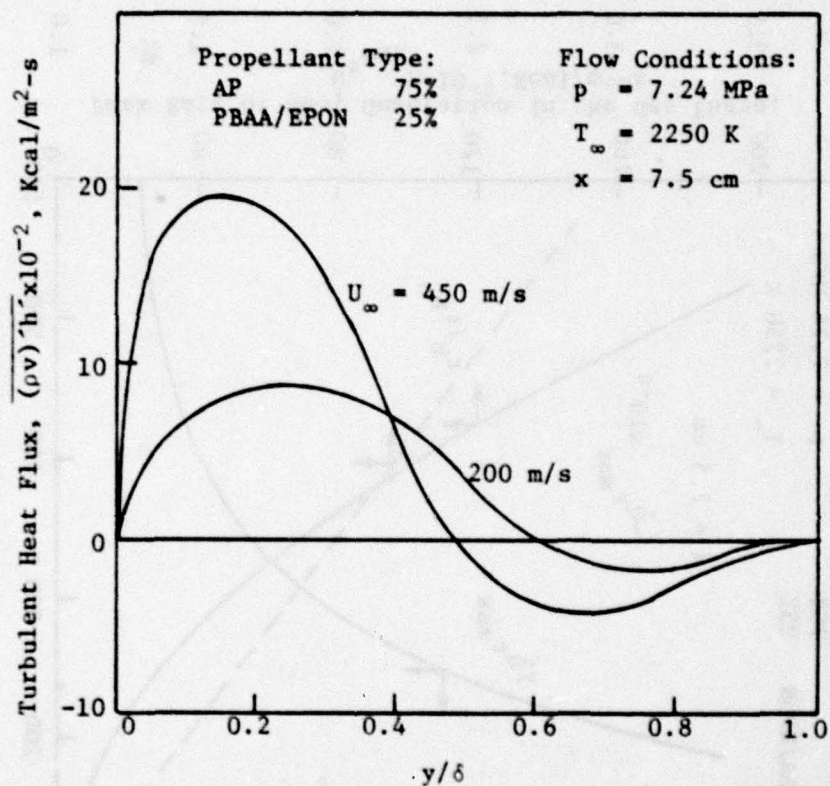


Figure 36 Calculated Turbulent Heat-Flux Distributions for Different Free-Stream Velocities

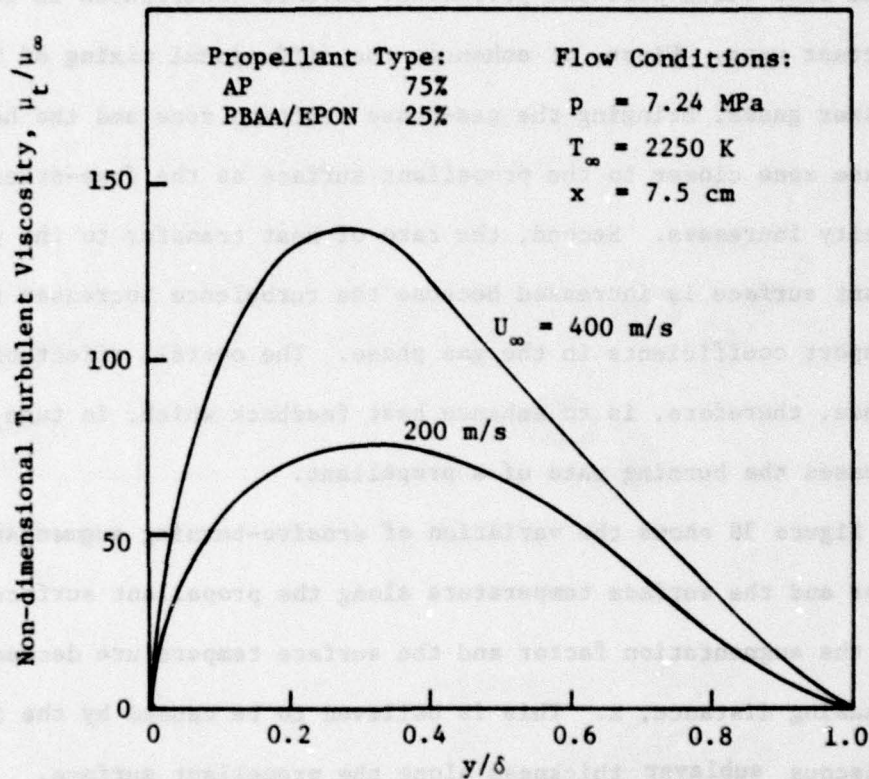


Figure 37 Calculated Turbulent Viscosity Distributions for Different Free-Stream Velocities

151

$(\rho v)'h'$, the turbulent heat flux, (see Figure 36) are found in the outer portion of the boundary layer because of the fact that the heat is transported away from the reaction zone, toward both the propellant surface and the free stream.

From the above discussion, it is seen that the turbulent nature of the flow field over the propellant surface contributes in two important ways. First, it enhances the diffusional mixing of fuel and oxidizer gases, bringing the gas-phase reaction zone and the heat release zone closer to the propellant surface as the free-stream velocity increases. Second, the rate of heat transfer to the propellant surface is increased because the turbulence increases the transport coefficients in the gas phase. The overall effect of turbulence, therefore, is to enhance heat feedback which, in turn, increases the burning rate of a propellant.

Figure 38 shows the variation of erosive-burning augmentation factor and the surface temperature along the propellant surface. Both the augmentation factor and the surface temperature decrease with increasing distance, x . This is believed to be caused by the increase in viscous sublayer thickness along the propellant surface.

Figure 39 shows the effect of normal burning rate on the erosive-burning augmentation factor. The AP/Polysulfide propellant (type 2), with a lower value of normal burning rate, is found to be more sensitive to the erosive burning effect than that of the AP/PBAA-EPON propellant (type 1), which has a higher value of normal burning rate. This observation is consistent with the experimental findings of Green (25) and that of Marklund and Lake (26).

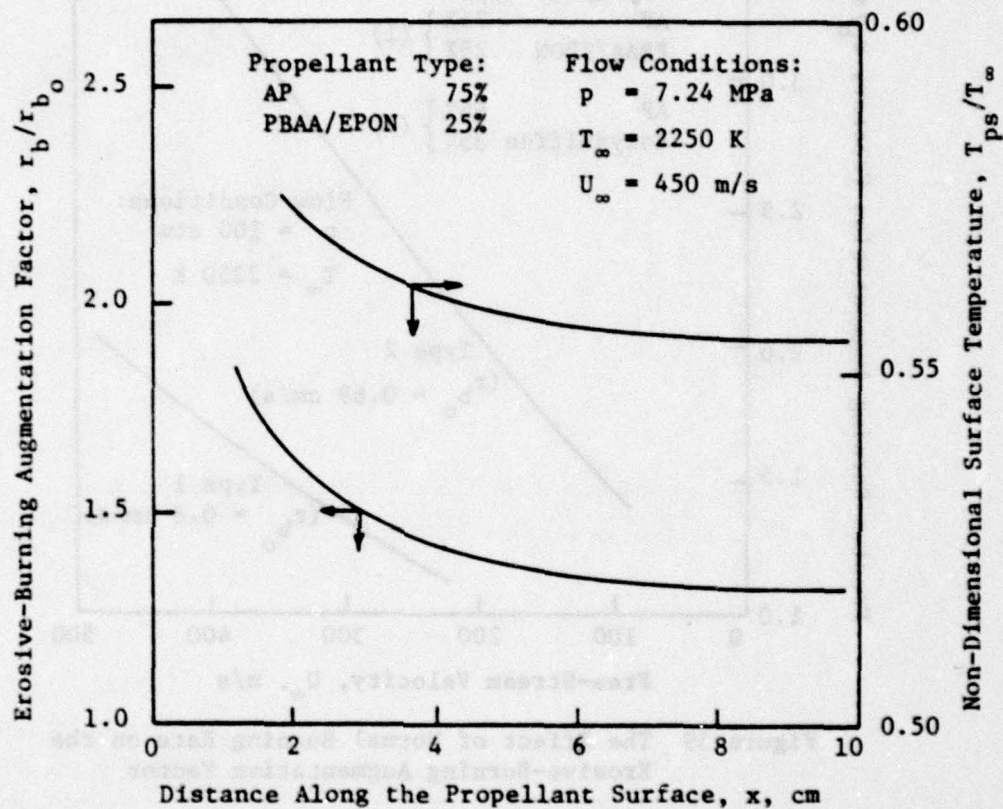


Figure 38 Variation of Erosive-Burning Augmentation Factor and the Propellant-Surface Temperature Along the Propellant Surface

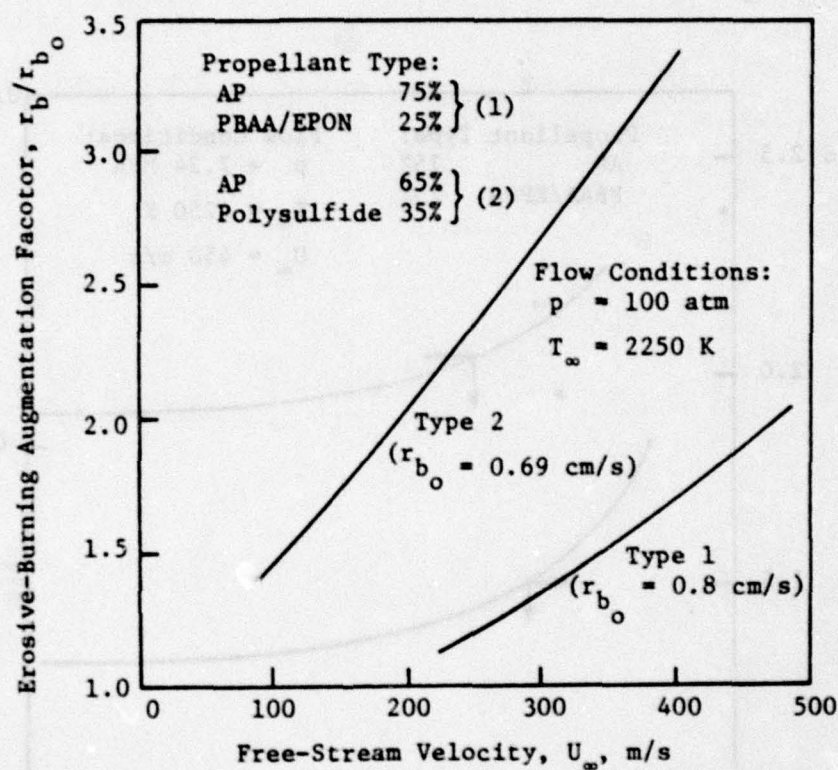


Figure 39 The Effect of Normal Burning Rate on the Erosive-Burning Augmentation Factor

Many composite solid propellants have some roughness, depending on the particle size of the oxidizer. Figure 40 demonstrates the effect of surface roughness on the augmentation factor for different free-stream velocities. As the roughness height increases, the augmentation factor also increases. This is to be expected since roughness aids the fuel and oxidizer mixing process because of increased turbulent activity closer to the propellant surface. However, the effect of roughness diminishes for lower free-stream velocities. This is because the viscous sublayer thickness increases at low velocities, submerging the roughness elements in the sublayer and, therefore, lessening their effect on the erosive-burning process.



Figure 40. Comparison of erosive-burning augmentation factor for different free-stream velocities and roughness heights.

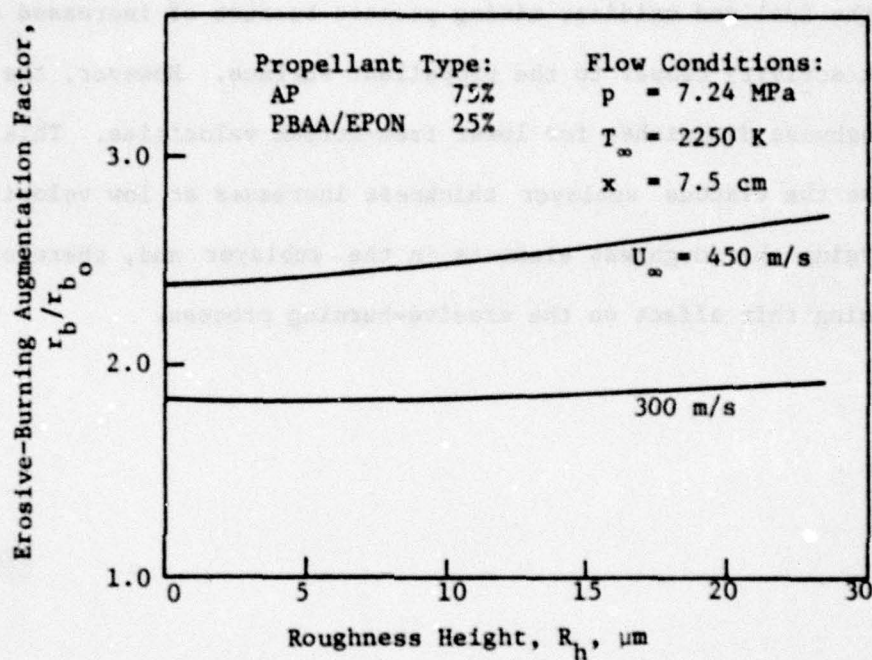


Figure 40 Computed Erosive-Burning Augmentation Factor Showing the Effect of Propellant-Surface Roughness Height at Different Free-Stream Velocities

CHAPTER 6

SUMMARY AND CONCLUSIONS

6.1 Summary

The basic purpose of this investigation was to formulate and verify a theoretical model for the erosive-burning problem commonly encountered in solid-propellant rocket motors.

A theoretical model was developed, based on the aerothermochemical analysis of the problem. The propellant burning process was described by analyzing a steady, two-dimensional, chemically reacting, turbulent boundary layer over the propellant surface. A "two-equation" turbulence closure model was employed, in which the turbulence is characterized by its kinetic energy and dissipation. The diffusion-controlled chemical reaction rate was realistically modeled by using the eddy-break-up concept in which the rate of consumption of fuel gases is assumed to be proportional to the rate at which fuel eddies break up into smaller eddies. In the solid phase, heat-transfer mechanism was described by a heat conduction equation which was related to the propellant-surface temperature and the burning rate. Appropriate boundary conditions were prescribed to complete the theoretical model.

The system of six nonlinear, coupled, parabolic, partial differential equations describing the theoretical model was solved numerically on a computer. The differential equations were approximated by finite difference equations after the introduction of coordinate transformations. A computer code was developed to obtain numerical solutions of the theoretical model. The numerical solution technique and various models introduced for turbulence closure were tested by comparing computed results for various turbulence quantities

with experimental data available in literature. All of these comparisons indicated good agreement.

Experimental apparatus for measuring the erosive-burning rate of a propellant was designed and fabricated. Consistent with the theoretical model, the burning of a composite solid propellant slab was studied in a chemically-reacting turbulent boundary layer formed by the flow of hot combustion gases over the propellant surface. The gas flow was generated by burning an N-4 star-shaped propellant grain in a driver motor. The burning rate of the propellant at various pressures and free-stream velocities was measured by a high-speed motion picture technique in which the burning propellant surface was photographed during a test firing. Pressures in the test chamber were measured at three different locations by a piezo-electric measuring system. The burning rate of a test propellant and the chamber pressure were properly coordinated by event markers.

The predicted burning rates from the theoretical model were compared with the measurements at various pressures and velocities. The comparison showed a close agreement between theoretical and experimental data. Theoretical predictions for a different propellant were also compared with the data obtained by Marklund and Lake (26); again, good agreement was achieved. A correlation was developed for the measured burning rates in terms of pressure and free-stream velocity.

6.2 Conclusions

The following observations and conclusions can be made from the present study:

- (1) The basic mechanism for the erosive-burning effect is believed to be the increased heat feedback to the propellant surface, introduced by the turbulence-enhanced mixing and reaction of the oxidizer and fuel gases and by the increase in transport coefficients in the gas phase. The increase in free-stream gas velocity brings the location of the peak turbulence intensity and the reaction zone closer to the propellant surface. Thus, more heat is released near the surface, increasing the heat feedback to the propellant surface and the burning rate of a solid propellant.
- (2) The predicted results show that propellants with lower normal burning rates are more sensitive to erosive burning than those with higher normal burning rates.
- (3) Surface roughness of a propellant sample increases the erosive burning effect of a composite solid propellant. However, the roughness effect diminishes with a decrease in free-stream velocity.
- (4) Both experimental and theoretical results show that the erosive-burning rate is more pronounced at higher pressures than that at lower pressures.
- (5) At low pressures and low velocities, the erosive effect is found to be small.
- (6) The erosive burning rate correlates well with chamber pressure and free-stream velocity. Correlations of this type can be used

conveniently in the design considerations of a solid propellant rocket motor.

- (1) The basic mechanism for the erosive-burning effect is believed to be the increased heat feedback to the propellant surface, introduced by the turbulent-entrained gases and reaction of the oxidizer and fuel gases and by the impingement of the propellant particles in the gas phase. The increase in propellant surface area and velocity change the location of the heat feedback interface and the reaction zone closer to the propellant surface. Thus, more heat is retained near the surface, increasing the heat feedback to the propellant surface and the burning rate of a solid propellant.
- (2) The present results show that propellants with lower burning rates are more sensitive to erosive burning than those with higher burning rates.
- (3) Increase in pressure of a propellant sample increases the erosive burning effect of a composite solid propellant. However, the erosive effect decreases with a decrease in grain diameter.
- (4) Both experimental and analytical results show that the erosive-burning rate is more pronounced at higher pressures than at lower pressures.
- (5) At low pressures and low velocities, the erosive effect is found to be small.
- (6) The erosive burning rate correlates well with chamber pressure and grain surface velocity. Correlations of this type can be used

6.3 Recommendations for Future Study

6.3.1 Theoretical Work

- (1) The conservation equations for the current erosive-burning model are based on a two-dimensional geometry and are applicable to a turbulent boundary layer over a flat plate. The reason for choosing a two-dimensional geometry in the current erosive-burning investigation was to develop a model which could easily be verified experimentally. The test rig for measuring erosive-burning rates was designed with fewer complications than are necessary for an axisymmetric geometry. In many actual rocket motors, the flow configuration, however, is axisymmetric. In order to predict the erosive-burning rates in such rocket motors, the current two-dimensional model should be extended to the axisymmetric flow configuration. This can be done by developing the governing equations and boundary conditions in a way similar to that followed in this study. The axisymmetric model can include the consideration for both the potential core region as well as the fully developed region in a rocket-motor propellant grain.
- (2) The erosive burning computer code for axisymmetric flow configuration can be coupled with a well-established rocket performance code to predict the pressure-time history in a rocket motor.
- (3) The current model can be modified to study the effect of pressure-velocity coupled oscillations on the instantaneous burning rates of a propellant in a rocket motor.

6.3.2 Experimental Work

- (1) The pressure-velocity coupled effect on propellant burning rate can be experimentally studied by inducing pressure oscillations; for example, by partially blocking and unblocking the exit nozzle at a known frequency.
- (2) The surface roughness of a burning solid propellant sample can be studied by extinguishing the propellant through a rapid depressurization of the chamber and studying the surface roughness under an electron microscope.
- (3) The experimental test rig for the present study was designed to measure the burning rate by two methods; the high-speed motion picture method, and the laser-photodiode servo-mechanism method. The latter method was not used in the present study because the combustion products deposited carbon particles on the plexiglass window, blocking the laser beam. One way to solve this problem is to design a window through which a high-pressure nitrogen gas can be injected to purge the path for the laser beam.

REFERENCES

1. Geckler, R. D., et. al., Aerojet Engineering Corporation, Report 445, (1950).
2. Vandekerckhove, J. A. and A. Jaumotte, "Remarks on the Burning Mechanism and Erosive Burning of Ammonium Perchlorate Propellants," Eighth Symposium (International) on Combustion, pp. 689-692, (1960).
3. Blatz, P. J., "A simplified Approach to Erosive Burning," Eighth Symposium (International) on Combustion, pp. 745-753, (1960).
4. Dickinson, L. A., F. Jackson, and A. L. Odgers, "Erosive Burning of Polyurethane Propellants in Rocket Engines," Eighth Symposium (International) on Combustion, pp. 754-759, (1960).
5. Vandekerckhove, J. A., University of Brussels Inst. Aeron. Tech. Note 2 on Contract AF61 (052)-354, (1961).
6. Zucrow, M. J., J. R. Osborn and J. M. Murphy, "An Experimental Investigation of the Erosive Burning Characteristics on a Non-Homogeneous Solid Propellant," AIAA Preprint No. 64-107, Solid Propellant Rocket Conference, Palo Alto, California, January 29-31, 1964.
7. Kreidler, J. W., "Erosive Burning: New Experimental Techniques and Methods of Analysis," AIAA Preprint No. 64-155, Solid Propellant Rocket Conference, Palo Alto, California, January 29-31, 1964.
8. Saderholm, C. A., "A Characterization of Erosive Burning for Composite H-Series Propellants," AIAA Solid Propellant Rocket Conference, Palo Alto, California, January 29-31, 1964.
9. Peretz, A., "Investigation of the Erosive Burning of Solid-Propellant Grains with Variable Port Area by Means of Interrupted Burning Experiments," Israel Journal of Technology, Vol. 3, pp. 94-101, (1965).
10. Miller, E. "Erosive Burning of Composite Solid Propellants," Combustion and Flame, Vol. 10, pp. 330-336, (1966).
11. Lawrence, W. J. and L. I. Deverall, "The Erosive Burning Behavior of Selected Composite Propellants," 4th ICRPG Combustion Conference, Stanford, CPIA Publication No. 162, Vol. 1, pp. 459-465, (1967).
12. Vilyunov, V. N. and A. A. Dvoryashin, "An Experimental Investigation of the Erosive Burning Effect," Combustion, Explosion and Shockwaves, Vol. 7, No. 1, pp. 38-42, (1971).

REFERENCES (continued)

13. Takishita, Y., K. Sumi and N. Kubota, "Erosive Burning Phenomena," Japan Defense Agency, Technical Research and Development Institute, (1973).
14. Parr, R. G. and B. L. Crawford, "A Physical Theory of Burning of Double-Base Propellants," Journal of Physical Chemistry, Vol. 54, pp. 929-954, (1950).
15. Lenngren, C. E., L. Person and S. Peterson, "A Method of Investigation of the Erosion of Rocket Propellants," Tech. Rept. NZP 7-55, Bofors, (1955).
16. Fenech, E. J. and J. S. Billheimer, "Use of Internal Grain Configuration to Predict Erosive Burning Constant," Western States Section, The Combustion Institute Paper No. 61-8, (1961).
17. Stone, W. C., "A Practical Method for Compensation of Erosive Pressure Peaks," American Rocket Society, Solid Propellant Rocket Conference, Salt Lake City, Utah, February 1-3, 1961.
18. Barrère, M. and P. Larue, "Contribution to the Study of Erosive Burning in Composite Rocket Grains," La Recherche Aerospatiale, 95, pp. 25-36, (1963).
19. Murphy, J. M., "Analytical Approaches to Erosive Burning," The Performance of High Temperature Systems, Proceedings of the Third Conference, Pasadena, California, Vol. 1, December 7-9, 1964.
20. Lawrence, W. J., D. R. Matthews and L. I. Deverall, "The Experimental and Theoretical Comparison of the Erosive Burning Characteristics of Composite Propellants," AIAA Paper No. 68-531, ICRPG/AIAA 3rd Solid Propulsion Conference, Atlantic City, New Jersey, June 4-6, 1968.
21. Williams, F. A., M. Barrère and N. C. Haung, "Fundamental Aspects of Solid Propellant Rockets," AGARDograph-116, Technivision, pp. 395-456, (1969).
22. Jankowski, A., "Mechanism of Erosive Burning of Solid Rocket Propellants," Archiwum Procesow Spalania, Vol. 3, No. 3, pp. 249-277, (1972).
23. Yamada, K., M. Goto and Y. Takishita, "A Study on Flow in a Pipe with Intense Transpiration," Defense Academy Research Report on the Institute of Science and Engineering, Japan, Vol. 11, No. 2, (1973).
24. Nagaoka, T., K. Shirota, K. Toreki and S. Saito, "An Experimental Study on Erosive Burning in Solid Propellant Motors," Int. Symp. on Space Tech. and Science, 10th Tokyo, Japan, pp. 83-90 September 2-3, 1973.

REFERENCES (continued)

25. Green, L., Jr., "Erosive Burning of Some Composite Solid Propellants," Jet Propulsion, Vol. 24, pp. 9-15, (1954).
26. Marklund, T. and A. Lake, "Experimental Investigation of Propellant Erosion," ARS Journal, Vol. 3, No. 2, pp. 173-178, (1960).
27. Lenoir, J. M. and G. Robillard, "A Mathematical Method to Predict the Effects of Erosive Burning in Solid-Propellant Rockets," Sixth Symposium (International) on Combustion, pp. 663-667, (1957).
28. Vandekerckhove, J. A., "Erosive Burning of a Colloidal Solid Propellant," Jet Propulsion, Vol. 28, pp. 599-603, (1958).
29. King, M. K., "A Modification of the Composite Propellant Erosive Burning Model of Lenoir and Robillard," Combustion and Flame, Vol. 24, pp. 365-368, (1975).
30. Corner, J., "The Effect of Turbulence on Heterogeneous Reaction Rates," Trans. Faraday Soc., Vol. 43, pp. 635-642, (1947).
31. Tsuji, H., "An Aerothermochemical Analysis of Erosive Burning of Solid Propellant," Ninth Symposium (International) on Combustion, pp. 384-393, (1963).
32. Razdan, M. K., "Theoretical Studies on the Erosive Burning of Double-Base Solid Propellants," Master of Technology Thesis, Indian Institute of Technology, Kanpur, June 1974.
33. Lengellé, G., "Model Describing the Erosive Combustion and Velocity Response of Composite Propellants," AIAA Journal, Vol. 13, pp. 315-322, (1975).
34. Jojic, B. and D.J. Blagojevic, "Theoretical Prediction of Erosive Burning Characteristics of Solid Rocket Propellant Based on Burning Rate Dependence of Pressure and Initial Temperature and its Energetic Characteristics," AIAA Paper No. 76-697, AIAA/SAE 12th Propulsion Conference, Palo Alto, California, July 26-29, 1976.
35. Rout, R. K., H. S. Makunda and V. K. Jain, "Erosive Burning Characteristic of Solid Propellant Rocket Motor," AIAA Paper No. 78-1097, AIAA/SAE 14th Joint Propulsion Conference, Las Vegas, Nevada, July 25-27, 1978.
36. Parkinson, R. C. and P. D. Penny, "A Transpired Boundary Layer Model of Erosive Burning," AIAA Paper No. 78-980, AIAA/SAE 14th Joint Propulsion Conference, Las Vegas, Nevada, July 25-27, 1978.
37. Schuyler, F. L. and T. P. Torda, "An Aerothermochemical Analysis of Solid Propellant Combustion," AIAA Journal, Vol. 4, No. 12, pp. 2171-2177, (1966).

REFERENCES (continued)

38. Yamada, K., M. Goto and N. Ishikawa, "A Simulative Study on the Erosive Burning of Solid Rocket Motors," AIAA Paper No. 75-1201, AIAA/SAE 11th Propulsion Conference, Anaheim, California, September 29-October 1, 1975.
39. King, M. K., "An Analytical and Experimental Study of the Erosive Burning of Composite Propellants," Final Report, AFOSR-TR-78-0060, (1977).
40. King, M. K., "Model for Steady State Combustion of Unimodal Composite Solid Propellants," AIAA Paper No. 78-216, AIAA 16th Aerospace Sciences Meeting, Huntsville, Alabama, January 16-18, 1978.
41. Beddini, R. "Reacting Turbulent Boundary-Layer Approach to Solid Propellant Erosive Burning," AIAA Journal, Vol. 16, No. 9, pp. 898-905, (1978).
42. Kuo, K.K. and M. K. Razdan, "Review of Erosive Burning of Solid Propellants," 12th JANNAF Combustion Meeting, CPIA Publication 273, Vol. II, pp. 323-338, (1975).
43. King, M. K., "Review of Erosive Burning Models," JANNAF Workshop on Erosive Burning/Velocity Coupling, Lancaster, California, March 7-8, 1977.
44. Summerfield, M., G. S. Sutherland, M. J. Webb, H. J. Taback and K. P. Hall, "Burning Mechanism of Ammonium Perchlorate Propellants," Solid Propellant Rocket Research, Progress in Astronautics and Rocket Series, Vol. 1, Academic Press, New York, pp. 141-182, (1960).
45. Steinz, J. A., P. L. Stang and M. Summerfield, "The Burning Mechanism of Ammonium Perchlorate-Based Composite Solid Propellants," Aerospace and Mechanical Science Report No. 830, ONR Contract Nonr. 1858, 32, (1969).
46. Hermance, C. E., "A Model of Composite Propellant Combustion Including Surface Heterogeneity and Heat Generation," AIAA Journal, Vol. 4, No. 9, pp. 1629-1637, (1966).
47. Beckstead, M. W., R. L. Derr and C. F. Price, "A Model of Composite Solid-Propellant Combustion Based on Multiple Flames," AIAA Journal, Vol. 8, No. 12, pp. 2200-2207, (1970).
48. Squire, L. C., "The Constant Property Turbulent Boundary Layer with Injection; A Reanalysis of Some Experimental Results," Int. J. Heat Mass Transfer, 13, (1970).
49. Marxman, G. and M. Gilbert, "Turbulent Boundary Layer Combustion in the Hybrid Rocket," Ninth Symposium (International) on Combustion, pp. 371-383, (1963).

REFERENCES (continued)

50. Denison, M. R., "The Turbulent Boundary Layer on Chemically Active Ablating Surfaces," J. Aero. Sci., Vol. 28, pp. 471-479, (1961).
51. Rosner, D. E., "Correlation and Prediction of Boundary Layer Energy Transfer Rates in the Presence of Chemical Reactions and Mass Injection," Combustion Science and Technology, Vol. 10, pp 97-108, (1975).
52. Lockwood, F. C. and A. S. Naguib, "The Prediction of the Fluctuations in the Properties of Free, Round-Jet, Turbulent, Diffusion Flames", Combustion and Flame, Vol. 24, pp. 109-124, (1975).
53. Gosman, A. D., F. C. Lockwood and S. A. Syed, "Prediction of a Horizontal Free Turbulent Diffusion Flame," Sixteenth Symposium (International) on Combustion, pp. 1543-1555, (1976).
54. Spalding, D. B., "Mathematical Models of Turbulent Flames, A Review," Combustion Science and Technology, Vol. 13, pp. 3-25, (1976).
55. Elghobashi, S. E. and W. M. Pun, "A Theoretical and Experimental Study of Turbulent Diffusion Flames in Cylindrical Furnaces," Fifteenth Symposium (International) on Combustion, pp. 1353-1365, (1974).
56. Spalding, D. B., "Mixing and Chemical Reaction in Steady Confined Turbulent Flames," Thirteenth Symposium (International) on Combustion, pp. 649-657, (1971).
57. Williams, F. A., Combustion Theory, Addison-Wesley, (1965).
58. Favre, A., "Equations des gaz turbulents compressibles," J. de Mechanique, Vol. 4, No. 3, pp. 361-390, (1965).
59. Laufer, J., "Thought on Compressible Turbulent Boundary Layers," NASA SP-216, (1968).
60. Kistler, A. L., "Fluctuation Measurement in a Supersonic Turbulent Boundary Layer," The Physics of Fluids, Vol. 2, No. 3, pp. 290-296, (1959).
61. Wooldridge, C. E. and R. J. Muzzy, "Measurements in a Turbulent Boundary Layer with Porous Injection and Combustion," Tenth Symposium (International) on Combustion, pp. 1351-1362, (1965).
62. Eschenroeder, A. G., "Turbulent Spectra in a Reacting Gas," AIAA Journal, Vol. 4, pp. 1839-1845, (1965).
63. Kulgein, N. G., "Transport Processes in a Compressible Turbulent Boundary Layer," Journal of Fluid Mechanics, Vol. 12, pp. 417-437, (1962).

REFERENCES (continued)

64. Launder, B. E. and D. B. Spalding, Mathematical Models of Turbulence, Academic Press, (1972).
65. Mason, H. B. and D. B. Spalding, "Prediction of Reaction Rates in Turbulent Pre-Mixed Boundary Layer Flows," Combustion Institute, First European Symposium, pp. 601-606, (1973).
66. Lockwood, F. C., "The Modeling of Turbulent Premixed and Diffusion Combustion in the Computation of Engineering Flows," Combustion and Flame, Vol. 29, pp. 111-122, (1977).
67. Spalding, D. B., "Concentration Fluctuations in a Round, Turbulent, Free Jet," Chem. Eng. Sci., Vol. 26, pp. 95-107, (1971).
68. Van Driest, E. R., "On Turbulent Flow Near a Wall," Journal of the Aeronautical Sciences, Vol. 23, pp. 1007-1011, (1956).
69. Chambers, T. L. and D. C. Wilcox, "Critical Examination of Two-Equation Turbulence Closure Models for Boundary Layers," AIAA Journal, Vol. 15, No. 6, pp. 821-828, (1977).
70. Patankar, S. V. and D. B. Spalding, Heat and Mass Transfer in Boundary Layers, Intertext Books, London, (1970).
71. White, F. M., Viscous Fluid Flow, McGraw-Hill Book Company, p. 593, (1974).
72. Schlichting, H., Boundary-Layer Theory, McGraw-Hill Book Company, (1968).
73. Sparrow, E. M. and H. S. Yu, "Local Non-Similarity Thermal Boundary-Layer Solutions," Transactions of the ASME, Journal of Heat Transfer, pp. 328-334, (1971).
74. Baker, R. J. and B. E. Launder, "The Turbulent Boundary Layer with Foreign Gas Injection - I. Measurements in Zero Pressure Gradient," Int. J. Heat Mass Transfer, Vol. 17, pp. 275-291, (1974).
75. Klebanoff, P. S., "Characteristics of Turbulence in a Boundary Layer with Zero Pressure Gradient," N.A.C.A. TN 3178, (1954).
76. Hottel, H. C. and A. F. Sarofim, Radiative Transfer, McGraw-Hill Book Company, New York, (1967).
77. Peretz, A., K. K. Kuo, L. H. Caveny and M. Summerfield, "Starting Transient of Solid Propellant Rocket Motors with High Internal Gas Velocities," AIAA Journal, Vol. 11, No. 12, pp. 1719-1727, (1973).

REFERENCES (continued)

78. Kays, W. M., "Heat Transfer to the Transpired Turbulent Boundary Layer," Int. J. Heat Mass Transfer, Vol. 15, pp. 1023-1044, (1972).
79. Gordon, S. and B. J. McBride, "Computer Program for Calculation of Chemical Equilibrium Compositions, Rocket Performance, Incident and Reflected Shocks, and Chapman-Jouguet Detonations," NASA SP-273, (1971).
80. Lin, C. C. and S. F. Shen, "A Similarity Theory for Turbulent Boundary Layer Over a Flat Plate in Compressible Flow," NACA Tech. Note 2542, (1951).
81. Herring, J. H. and G. L. Mellor, "A Method of Calculating Compressible Turbulent Boundary Layers," NASA SP-216, (1968).
82. Shapiro, A. H., The Dynamics and Thermodynamics of Compressible Fluid Flow, Vol. 1, The Ronald Press Company, New York, (1953).

APPENDIX A

ORDER-OF-MAGNITUDE ANALYSIS

For the order of magnitude analysis of Equations (11) through (14), the dependable variables will be referred to their value at some reference point, r , outside the boundary layer, and coordinates x and y will be referred, respectively, by a representative dimension. Thus, we write

$$\bar{u} = U_r, \bar{v} = \frac{\delta}{L} U_r, \bar{\rho} = \rho_r, \bar{h} = h_r$$

Also for a boundary layer, we have

$$\frac{\partial}{\partial x} = \frac{1}{L}, \quad \frac{\partial}{\partial y} = \frac{1}{\delta} \quad (\text{A.1})$$

Order of magnitude of correlations involving density fluctuations: The density fluctuations, ρ' , result from several causes (80-81) listed below.

- (a) Mixing of fluid elements by turbulent bulk transport from regions of different density, velocity, and enthalpy.
- (b) Turbulent pressure fluctuations--compressibility effect.
- (c) Molecular viscous dissipation caused by the fluctuating velocity and molecular heat transfer driven by the fluctuating enthalpy.

According to references 59-60 and 80-81, (a) is considered to be the dominant cause for production of ρ' . Therefore, we may assume that the mass transport in y -direction is proportional to the product of the gradient of the transported property (ρ) and the velocity fluctuation.

$$\overline{\rho'v'} = \overline{u'v'} \left(\frac{\partial \bar{\rho}}{\partial y} \right) / \left(\frac{\partial \bar{u}}{\partial y} \right) \quad (\text{A.2})$$

where $\overline{u'v'}$ is the turbulent shear stress.

Furthermore, if the equations are to describe a boundary layer flow, the turbulent shear stress term, $\frac{\partial}{\partial x} (\bar{\rho} \overline{u'v'})$, must be of the same order as the inertia terms in the x-momentum equation of Equation (12).

Therefore

$$\frac{\partial}{\partial y} (\bar{\rho} \overline{u'v'}) = \left[\overline{u'v'} \frac{\partial \bar{\rho}}{\partial y} + \bar{\rho} \frac{\partial \overline{u'v'}}{\partial y} \right] \sim 0 \left(\bar{\rho} \bar{u} \frac{\partial \bar{u}}{\partial x} \right)$$

Using Equation (A.1), we write

$$\overline{u'v'} \frac{\bar{\rho}_r}{\delta} \left[1 + 0 \left(\frac{\Delta \rho}{\bar{\rho}_r} \right) \right] \sim 0 \left(\bar{\rho}_r \frac{U_r^2}{L} \right) \quad (\text{A.3})$$

Assume $\frac{\Delta \rho}{\bar{\rho}_r} \sim 0(1)$, since the temperature ratio across the boundary layer is of the order of unity; therefore, from Equation (A.3), we get

$$\overline{u'v'} \sim 0 \left(\frac{\delta}{L} U_r^2 \right) \quad (\text{A.4})$$

From Equations (A.2) and (A.4), therefore

$$\bar{\rho} \overline{v'^2} \sim 0 \left(\frac{\delta}{L} U_r^2 \right) \left(\frac{\Delta \rho}{\delta} \right) / \left(\frac{U_r}{\delta} \right) \sim 0 \left(\frac{\delta}{L} \Delta \rho U_r \right) \quad (\text{A.5})$$

Similarly, we can write the order of magnitude of $\bar{\rho} \overline{u'^2}$ as

$$\bar{\rho} \overline{u'^2} \sim 0 \left(\frac{\delta}{L} \Delta \rho U_r \right) \quad (\text{A.6})$$

Order of magnitude of correlations involving h' : Kistler (60) has experimentally found that the distribution of static temperature fluctuations is very nearly proportional to the static temperature difference across a boundary layer. Therefore, we can assume that the enthalpy fluctuations, h' , result mostly from the turbulent bulk transport of fluid elements. By following the same approach that yielded

Equation (A.5), we can write

$$\overline{\rho' h'} = 0 \left[\overline{u' v'} \left(\frac{\partial \bar{\rho}}{\partial y} \right) \left(\frac{\partial \bar{h}}{\partial y} \right) / \left(\frac{\partial \bar{u}}{\partial y} \right)^2 \right]$$

Using Equation (A.1) and (A.4), we get

$$\overline{\rho' h'} = 0 \left(\frac{\delta}{L} \Delta \rho \Delta h \right) \quad (\text{A.7})$$

Similarly one can show that

$$\overline{u' h'} = \overline{v' h'} = 0 \left(\frac{\delta}{L} \Delta h U_r \right) \quad (\text{A.8})$$

$$\overline{u' Y'_k} = \overline{v' Y'_k} = 0 \left(\frac{\delta}{L} \Delta Y_k U_r \right) \quad (\text{A.9})$$

Order of magnitude of correlations involving H' : From definition

$$H = h + \frac{1}{2} u_i u_i$$

Reynolds' decomposition gives

$$\bar{H} + H' = \bar{h} + h' + \frac{1}{2} \bar{u}_i \bar{u}_i + u'_i \bar{u}_i + \frac{1}{2} u'_i u'_i \quad (\text{A.10})$$

Time averaging reduces Equation (A.10) to

$$\bar{H} = \bar{h} + \frac{1}{2} (\bar{u}_i \bar{u}_i + \overline{u'_i u'_i}) \quad (\text{A.11})$$

Subtracting Equation (A.11) from Equation (A.10), we get

$$H' = h' + u'_i \bar{u}_i + \frac{1}{2} u'_i u'_i - \frac{1}{2} \overline{u'_i u'_i} \quad (\text{A.12})$$

Multiply Equation (A.12) by ρ' and then time average, so that

$$\overline{\rho' H'} = \overline{\rho' h'} + \overline{\rho' u'_i \bar{u}_i} + \frac{1}{2} \overline{\rho' u'_i u'_i} \quad (\text{A.13})$$

Assuming $\overline{\rho' u'_i u'_i} \ll \overline{\rho' u'_i}$ and using Equations (A.6) and (A.7), we find

$$\begin{aligned}\overline{\rho' H'} &= 0 \left(\frac{\delta}{L} \Delta h \Delta \rho \right) + 0 \left(\frac{\delta}{L} \Delta \rho U_r^2 \right) \\ &= 0 \left[\frac{\delta}{L} \Delta \rho (\Delta h + U_r^2) \right] = 0 \left(\frac{\delta}{L} U_r \Delta H \right)\end{aligned}\quad (\text{A.14})$$

Similarly it can be shown that

$$\overline{u' H'} = \overline{v' H'} = 0 \left(\frac{\delta}{L} \Delta H U_r \right) \quad (\text{A.15})$$

Now we write

$$\overline{(\rho u)' H'} = \bar{\rho} \overline{u' H'} + \bar{u} \overline{\rho' H'} + \overline{\rho' u' H'} ,$$

and using Equation (A.14) and (A.15), neglecting third order correlations, we get

$$\begin{aligned}\overline{(\rho u)' H'} &= 0 \left(\rho_r \frac{\delta}{L} U_r \Delta H + U_r \frac{\delta}{L} \Delta \rho \Delta H \right) \\ &= 0 \left[\left(1 + \frac{\Delta \rho}{\rho_r} \right) \frac{\delta}{L} \rho_r U_r \Delta H \right] = 0 \left(\frac{\delta}{L} \rho_r U_r \Delta H \right)\end{aligned}\quad (\text{A.16})$$

Similarly

$$\overline{(\rho v)' H'} = 0 \left(\frac{\delta}{L} \rho_r U_r \Delta H \right) \quad (\text{A.17})$$

$$\overline{(\rho v)' Y_k} = \overline{(\rho u)' Y_k} = 0 \left(\frac{\delta}{L} \rho_r U_r \Delta Y_k \right) \quad (\text{A.18})$$

Using various orders of magnitude derived above, the steady state, two-dimensional, conservation equations are written and the relative orders of magnitude of the terms are given below each equation.

Mass Conservation Equation:

$$\frac{\partial}{\partial x} (\bar{\rho} \bar{u}) + \frac{\partial}{\partial x} (\bar{\rho}' \bar{u}') + \frac{\partial}{\partial y} (\bar{\rho} \bar{v}) + \frac{\partial}{\partial y} (\bar{\rho}' \bar{v}') = 0$$

$$\left(1 + \frac{\Delta \rho}{\rho_r}\right) \left(\frac{\delta}{L} \frac{\Delta \rho}{\rho_r}\right) \left(1 + \frac{\Delta \rho}{\rho_r}\right) \left(\frac{\Delta \rho}{\rho_r}\right) \quad (\text{A.19})$$

x-Momentum Conservation Equation:

$$\bar{\rho} \bar{u} \frac{\partial \bar{u}}{\partial x} + \bar{\rho}' \bar{u}' \frac{\partial \bar{u}}{\partial x} + \bar{\rho} \bar{v} \frac{\partial \bar{u}}{\partial y} + \bar{\rho}' \bar{v}' \frac{\partial \bar{u}}{\partial y}$$

$$(1) \left(\frac{\Delta \rho}{\rho_r} \frac{\delta}{L}\right) (1) \left(\frac{\Delta \rho}{\rho_r}\right)$$

$$= - \frac{\partial \bar{p}}{\partial x} + \mu \left[\frac{\partial^2 \bar{u}}{\partial y^2} + \frac{4}{3} \frac{\partial^2 \bar{u}}{\partial x^2} + \frac{1}{3} \frac{\partial^2 \bar{v}}{\partial x \partial y} \right] - \frac{\partial}{\partial x} (\bar{\rho} \bar{u}' \bar{u}') +$$

$$\left(\frac{L}{\rho_r U_r}\right)^2 \frac{\partial \bar{p}}{\partial x} \left(\frac{L}{\delta}\right)^2 \frac{1}{Re_L} \left[(1) \left(\frac{\delta}{L}\right)^2 \left(\frac{\delta}{L}\right)^2 \right] \left(1 + \frac{\Delta \rho}{\rho_r}\right) \left(\frac{\delta}{L}\right)$$

$$- \frac{\partial}{\partial y} (\bar{\rho} \bar{u}' \bar{v}') - \frac{\partial}{\partial x} (\bar{u} \bar{\rho}' \bar{u}') - \frac{\partial}{\partial y} (\bar{v} \bar{\rho}' \bar{u}')$$

$$\left(1 + \frac{\Delta \rho}{\rho_r}\right) \left(\frac{\Delta \rho}{\rho_r} \frac{\delta}{L}\right) \left(\frac{\Delta \rho}{\rho_r} \frac{\delta}{L}\right) \quad (\text{A.20})$$

y-Momentum Conservation Equation:

$$\bar{\rho} \bar{u} \frac{\partial \bar{v}}{\partial x} + \bar{\rho}' \bar{u}' \frac{\partial \bar{v}}{\partial x} + \bar{\rho} \bar{v} \frac{\partial \bar{v}}{\partial y} + \bar{\rho}' \bar{v}' \frac{\partial \bar{v}}{\partial y}$$

$$\left(\frac{\delta}{L}\right) \frac{\Delta \rho}{\rho_r} \left(\frac{\delta}{L}\right)^2 \left(\frac{\delta}{L}\right) \left(\frac{\Delta \rho}{\rho_r} \frac{\delta}{L}\right)$$

$$= - \frac{\partial \bar{p}}{\partial y} + \mu \left[\frac{\partial^2 \bar{v}}{\partial x^2} + \frac{4}{3} \frac{\partial^2 \bar{v}}{\partial y^2} + \frac{1}{3} \frac{\partial^2 \bar{u}}{\partial x \partial y} \right] - \frac{\partial}{\partial x} (\bar{\rho} \bar{u}' \bar{v}') +$$

$$\left(\frac{L}{\rho_r U_r}\right)^2 \frac{\partial \bar{p}}{\partial y} \left(\frac{L}{\delta}\right)^2 \frac{1}{Re_L} \left[\left(\frac{\delta}{L}\right)^3 \left(\frac{\delta}{L}\right) \left(\frac{\delta}{L}\right) \right] \left(1 + \frac{\Delta \rho}{\rho_r}\right) \left(\frac{\delta}{L}\right)$$

$$\begin{aligned}
& - \frac{\partial}{\partial y} (\bar{\rho} \overline{v'v'}) - \frac{\partial}{\partial x} (\bar{u} \overline{\rho'v'}) - \frac{\partial}{\partial y} (\bar{v} \overline{\rho'v'}) \\
& \quad \left(1 + \frac{\Delta \rho}{\rho_r}\right) \quad \left(\frac{\Delta \rho}{\rho_r} \frac{\delta}{L}\right) \quad \left(\frac{\Delta \rho}{\rho_r} \frac{\delta}{L}\right) \quad (A.21)
\end{aligned}$$

Species Conservation Equation: We assume that $D \overline{\rho'Y'}_{k,1} \ll D \bar{\rho} \bar{Y}_{k,1}$ in Equation (13). Therefore, we write:

$$\bar{\rho} \bar{u} \frac{\partial \bar{Y}_k}{\partial x} + \bar{\rho} \overline{u'} \frac{\partial \bar{Y}_k}{\partial x} + \bar{\rho} \bar{v} \frac{\partial \bar{Y}_k}{\partial y} + \bar{\rho} \overline{v'} \frac{\partial \bar{Y}_k}{\partial y}$$

$$(1) \quad \left(\frac{\Delta \rho}{\rho_r} \frac{\delta}{L}\right) \quad (1) \quad \left(\frac{\Delta \rho}{\rho_r}\right)$$

$$= \frac{\partial}{\partial x} (\bar{\rho} D \frac{\partial \bar{Y}_k}{\partial x}) + \frac{\partial}{\partial y} (\bar{\rho} D \frac{\partial \bar{Y}_k}{\partial y})$$

$$\frac{1}{Re_L Sc} \quad \left(\frac{L}{\delta}\right)^2 \frac{1}{Re_L Sc}$$

$$- \frac{\partial}{\partial x} (\overline{(\rho u)'Y'_k}) - \frac{\partial}{\partial y} (\overline{(\rho v)'Y'_k}) + \bar{\omega}_k$$

$$\left(\frac{\delta}{L}\right) \quad (1) \quad \left(\frac{L}{\rho_r U_r Y_{k,r}} \bar{\omega}_k\right) \quad (A.22)$$

Energy Conservation Equation: It is assumed that $\overline{u'_j \tau'_{ij}} \ll \bar{u}_j \bar{\tau}_{ij}$ in the energy conservation equation, Equation (14), and it can be shown that $\bar{u}_j \bar{\tau}_{ij} \sim \mu \bar{u} \frac{\partial \bar{u}}{\partial y}$. Therefore, we can write:

$$\bar{\rho} \bar{u} \frac{\partial \bar{H}}{\partial x} + \bar{\rho} \overline{u'} \frac{\partial \bar{H}}{\partial x} + \bar{\rho} \bar{v} \frac{\partial \bar{H}}{\partial y} + \bar{\rho} \overline{v'} \frac{\partial \bar{H}}{\partial y}$$

$$(1) \quad \left(\frac{\Delta \rho}{\rho_r} \frac{\delta}{L}\right) \quad (1) \quad \left(\frac{\Delta \rho}{\rho_r}\right)$$

$$\begin{aligned}
&= \frac{\lambda}{C_p} \left[\frac{\partial^2 H}{\partial x^2} - \frac{1}{2} \frac{\partial^2}{\partial x^2} (\bar{u}_1 \bar{u}_1) - \frac{1}{2} \frac{\partial^2}{\partial x^2} (\overline{u_1' u_1'}) \right] - \frac{\partial}{\partial x} (\overline{(\rho u)' H'}) \\
&\quad \left(\frac{1}{Pr Re_L} \right) \left(\frac{1}{Pr Re_L} \frac{U_r^2}{H_r} \right) \left(\frac{1}{Pr Re_L} \frac{\delta}{L} \frac{U_r^2}{H_r} \right) \left(\frac{\Delta H}{H_r} \frac{\delta}{L} \right) \\
&+ \frac{\lambda}{C_p} \left[\frac{\partial^2 H}{\partial y^2} - \frac{1}{2} \frac{\partial^2}{\partial y^2} (\bar{u}_1 \bar{u}_1) - \frac{1}{2} \frac{\partial^2}{\partial y^2} (\overline{u_1' u_1'}) \right] - \frac{\partial}{\partial y} (\overline{(\rho v)' H'}) \\
&\quad \left(\frac{1}{Pr Re_L} \left(\frac{L}{\delta} \right)^2 \right) \left(\frac{1}{Pr Re_L} \left(\frac{L}{\delta} \right)^2 \frac{U_r^2}{H_r} \right) \left(\frac{1}{Pr Re_L} \left(\frac{L}{\delta} \right) \frac{U_r^2}{H_r} \right) \left(\frac{\Delta H}{H_r} \right) \\
&+ \frac{\partial}{\partial y} (\mu \bar{u} \frac{\partial \bar{u}}{\partial y}) \\
&\quad \left(\frac{1}{Re_L} \left(\frac{L}{\delta} \right)^2 \frac{U_r^2}{H_r} \right) \tag{A.23}
\end{aligned}$$

Procedure for the order of magnitude analysis of K-equation, Equation (20), is similar to that followed above. The result is that except for the convection terms on the left-hand side of Equation (20), all the terms with mean gradients with respect to x are negligible in comparison to those with mean gradients with respect to y . The last term of Equation (20) is simplified as follows:

$$\overline{u_1' \tau_{ij,j}} = \overline{u_1' (\mu (u_{1,j}' + u_{j,1}' - \frac{2}{3} \delta_{ij} u_{\ell,\ell}'))}_{,j} \tag{A.24}$$

In the above equation, the expression for $\tau_{ij,j}'$ has been substituted from Equation (6). This equation can be simplified further as

$$\overline{u_1' \tau_{ij,j}} = \overline{u_1' (\mu u_{1,j}')}_{,j} + \overline{u_1' (\mu u_{j,1}')}_{,j} - \frac{2}{3} \overline{u_1' (\mu u_{\ell,\ell}')}_{,i} \tag{A.25}$$

The last two terms of Equation (A.25) reduce to $\frac{1}{3} \mu \overline{u_1' u_{\ell, \ell 1}'}$ if μ is assumed to be constant. For an incompressible flow this term is zero because $u_{\ell, \ell}' = 0$. Here we will assume this term to be negligible in comparison to $\overline{u_1' (\mu u_{1,j}')}, j$. Therefore, Equation (A.25) simplifies to

$$\begin{aligned} \overline{u_1' \tau_{1j,j}'} &= \overline{u_1' (\mu u_{1,j}')}, j \\ &= \left\{ \mu \left(\frac{\overline{u_1' u_1'}}{2} \right), j \right\}, j - \mu \overline{u_{1,j}' u_{1,j}'} \\ &= \frac{\partial}{\partial y} \left(\mu \frac{\partial K}{\partial y} \right) - \bar{\rho} \epsilon \end{aligned} \quad (\text{A.26})$$

The two terms on the right-hand side of Equation (A.26) are: the diffusion of K by the molecular action of the fluid, and the dissipation of K through the action of viscosity, respectively. A separate equation is solved for the latter term, i.e., the dissipation equation (Equation 32). The above mentioned simplifications have been used in obtaining Equation (31) from Equation (20).

After a comparison is made between the various orders of magnitude in each equation, Equation (A.19) through (A.23), only the dominant terms are retained. It is noted that

$$\frac{\delta}{L} \ll 1, \quad Re_L \gg 1, \quad \left(\frac{L}{\delta}\right)^2 \frac{L}{Re_L} \sim 0 \quad (1)$$

$$Pr \sim Sc \sim 0 \quad (1)$$

Finally, we obtain the steady, two-dimensional boundary-layer equations for a chemically reacting, compressible, turbulent boundary layer over a flat plate, given in Section 2.

APPENDIX B

NEAR-WALL TREATMENT IN THE NUMERICAL PROCEDURE

The dependable variables vary steeply in a region close to the wall (propellant surface). Therefore, to obtain the fluxes of mass, momentum, and energy at the wall with reasonable accuracy, exact solutions of the conservation equations for these variables are obtained under the assumption of Couette flow. The basic Couette-flow assumption implies that the local x-wise convection of the dependable variables is negligible. This is a good assumption, particularly if the region near the wall is specified as very small where the velocity \bar{u} is small. With this assumption, the partial differential equations, Equations (28) through (30), reduce to ordinary differential equations, which can be integrated within the Couette-flow region. Details of this analysis are given in Reference 70. Further, we assume that within the Couette-flow region the changes in fluid flow properties (μ , μ_{eff} , Pr , etc.) are negligible. From the integration of the ordinary differential equations for \bar{u} , \bar{Y}_k and \bar{H} , the following relations can be derived (70):

$$s = \frac{B[1 - \{\exp(B \text{Re}_c) - 1 - B \text{Re}_c\} G/(B^2 \text{Re}_c)]}{\exp(B \text{Re}_c) - 1} \quad (\text{B.1})$$

$$S_k = \frac{B}{\exp(\text{Sc} B \text{Re}_c) - 1} \quad (\text{B.2})$$

$$S_h = \frac{B}{\exp(\text{Pr} B \text{Re}_c) - 1} \quad (\text{B.3})$$

where

$$B \text{ is the blowing parameter } \equiv \rho_s r_b / (\rho u)_c \quad (\text{B.4})$$

$$G \text{ is the pressure-gradient parameter } \equiv \left(\frac{y}{\rho u^2} \right)_c \frac{dp}{dx} \quad (\text{B.5})$$

$$\text{Re}_c \text{ is the Reynolds number based on the Couette-flow thickness } \equiv \left(\frac{\rho u y}{\mu} \right)_c \quad (\text{B.6})$$

c refers to the edge of the Couette-flow region. s , S_k and S_h are defined in terms of diffusional fluxes of momentum, species mass-fraction, and enthalpy at the wall:

$$\left(\mu \frac{\partial u}{\partial y} \right)_w \equiv \tau_w \equiv s(\rho u^2)_c \quad (\text{B.7})$$

$$\left(\frac{\mu}{Sc} \frac{\partial Y_k}{\partial y} \right)_w \equiv S_k (Y_{kc} - Y_{kw}) (\rho u)_c \quad (\text{B.8})$$

$$\left(\frac{\mu}{Pr} \frac{\partial h}{\partial y} \right)_w \equiv S_h \left\{ H_c - H_w + (Pr-1) \frac{u_c^2}{2} \right\} (\rho u)_c \quad (\text{B.9})$$

Subscript w designates the wall or surface condition, and k designates fuel, oxidizer, or product gases. In order to use Equations (B.8) and (B.9), the wall values of Y_k and H must be known. In the following, we will simplify the wall boundary conditions developed in Section 2 for enthalpy and species equation. First, rewrite Equations (49) and (57) as follows:

$$\left(\frac{\mu}{Sc} \frac{\partial Y_F}{\partial y} \right)_w = \rho_s r_b (Y_{Fw} - Y_{FS}) \quad (\text{B.10})$$

$$\left(\frac{\mu}{Sc} \frac{\partial Y_O}{\partial y} \right)_w = \rho_s r_b (Y_{Ow} - Y_{OS}) \quad (\text{B.11})$$

$$\left(\lambda \frac{\partial T}{\partial y} \right)_w = \rho_s r_b [C_p T_{ps} - C_s T_{pi} + \bar{Q}_s + (C_s - C_p) \bar{T}_{ps}] \quad (\text{B.12})$$

From the definition of stagnation enthalpy, Equation (5), we find

$$C_p \left. \frac{\partial T}{\partial y} \right|_w = \left. \frac{\partial H}{\partial y} \right|_w - \sum_k \Delta h^\circ_{f,k} \left. \frac{\partial Y_k}{\partial y} \right|_w \quad (B.13)$$

$$C_p T_{ps} = H_w - \sum_k \Delta h^\circ_{f,k} Y_{kw} + C_p T^\circ \quad (B.14)$$

Substituting Equations (B.13) and (B.14) in Equation (B.12), and also using the definition of Prandtl number ($Pr \equiv C_p \mu / \lambda$) to eliminate λ from Equation (B.12), we get

$$\begin{aligned} \rho_s r_b H_w - \frac{\mu}{Pr} \left. \frac{\partial H}{\partial y} \right|_w &= \rho_s r_b \sum_k \Delta h^\circ_{f,k} Y_{kw} - \frac{\mu}{Pr} \sum_k \Delta h^\circ_{f,k} \left. \frac{\partial Y_k}{\partial y} \right|_w \\ &\quad - \rho_s r_b [C_p T^\circ - C_s T_{pi} + \bar{Q}_s + (C_s - C_p) \bar{T}_{ps}] \end{aligned} \quad (B.15)$$

Substitute Equations (B.10) and (B.11) in Equation (B.15), and noting that the species summation index k represents fuel, oxidizer and product species, and that $Y_p = 1 - Y_O - Y_F$, we get

$$\begin{aligned} J_{tot,H,I} &= \rho_s r_b [\Delta h^\circ_{f,F} Y_{FS} + \Delta h^\circ_{f,O} Y_{OS} - C_p T^\circ + C_s T_{pi} \\ &\quad - \bar{Q}_s - (C_s - C_p) \bar{T}_{ps}] \end{aligned} \quad (B.16)$$

where the total flux of H at I boundary, $J_{tot,H,I}$, is equal to the left-hand side of Equation (B.15). Similarly, Equations (B.10) and (B.11) can be expressed in terms of total fluxes:

$$J_{tot, Y_F, I} \equiv \rho_s r_b Y_{Fw} - \left(\frac{\mu}{Sc} \frac{\partial Y_F}{\partial y} \right)_w = \rho_s r_b Y_{FS} \quad (B.17)$$

$$J_{tot, Y_O, I} \equiv \rho_s r_b Y_{Ow} - \left(\frac{\mu}{Sc} \frac{\partial Y_O}{\partial y} \right)_w = \rho_s r_b Y_{OS} \quad (B.18)$$

Surface Value of H : At the wall, since $u = 0$, from the definition of H

we can write

$$\left(\frac{\partial H}{\partial y}\right)_w = \left(\frac{\partial h}{\partial y}\right)_w \quad (\text{B.19})$$

Using Equations (B.9) and (B.19) in Equation (B.16), we get

$$H_w = [S_h(\rho u)_c \{H_c + (\text{Pr}-1) \frac{u^2}{2}\} + \rho_s r_b \{\Delta h_{f,F}^{\circ} Y_{FS} + \Delta h_{f,O}^{\circ} Y_{OS} \\ - C_p T^{\circ} + C_s T_{pi} - \bar{Q}_s - (C_s - C_p) \bar{T}_{ps}\}] / [\rho_s r_b + S_h(\rho u)_c] \quad (\text{B.20})$$

Surface Values of Y_F and Y_O : Substituting Equation (B.8) with $k=F$ and 0 in Equations (B.10) and (B.11), respectively, we find

$$Y_{Fw} = \frac{S_k(\rho u)_c Y_{Fc} + \rho_s r_b Y_{FS}}{\rho_s r_b + S_k(\rho u)_c} \quad (\text{B.21})$$

$$Y_{Ow} = \frac{S_k(\rho u)_c Y_{Oc} + \rho_s r_b Y_{OS}}{\rho_s r_b + S_k(\rho u)_c} \quad (\text{B.22})$$

The surface temperature, T_{ps} , is found from the definition of H given in Equation (5), after H_w is evaluated from Equation (B.20). Equations (B.8) and (B.9) are used with guessed surface values, and iterations of the solution are made to satisfy Equations (B.20) through (B.22). The Couette-flow region in the present study was identified as the region between the surface and the first grid point along ω -coordinate.

APPENDIX C

FINITE-DIFFERENCE EQUATIONS

To form the finite-difference equations for Equation (77), the boundary layer is divided into N strips from $\omega=0$ to $\omega=1$. The variation of ϕ between the grid points is assumed to be linear, except in the half-interval region near the boundaries at $\omega=0$ and $\omega=1$ (see Figure C.1). In the half-interval near the wall, the Couette-flow analysis (Appendix B) is used to give a better variation of ϕ . The finite-difference equations are formed by integrating Equation (77) in a small control volume of the flow field near a grid point (i,j) , where i and j represent the grid locations in x - and ω -directions respectively, as shown in Figure C.1. In this way the finite-difference equations are obtained; these relate $\phi_{i,j}$ to $\phi_{i,j-1}$ and $\phi_{i,j+1}$. At the boundaries, two points are identified corresponding to the true value of ϕ (ϕ_1 and ϕ_{N+3} at I and E boundaries, respectively), and a false or 'slip' value of ϕ (ϕ_2 and ϕ_{N+2} at I and E boundaries, respectively). The slip value is the one which would be obtained if ϕ was assumed to be linear near the boundaries. The integration of Equation (77) over the half-interval region near the boundaries gives the finite-difference equations expressing slip value of ϕ in terms of the true value, and the value of ϕ at the next grid close to the boundary. For example, at I boundary ϕ_2 is related to ϕ_1 and ϕ_3 through a finite-difference equation. The function of the slip value ϕ_2 is to orient $\phi_2 - \phi_3$ line so that a better representation is obtained for the region from $\omega_{2.5}$ (corresponding to $\phi_{2.5}$ in Figure C.1) to ω_3 than that given by $\phi_1 - \phi_3$ line.

The details of the integration procedure to obtain the finite-difference equations are given in Reference 70. We will summarize only

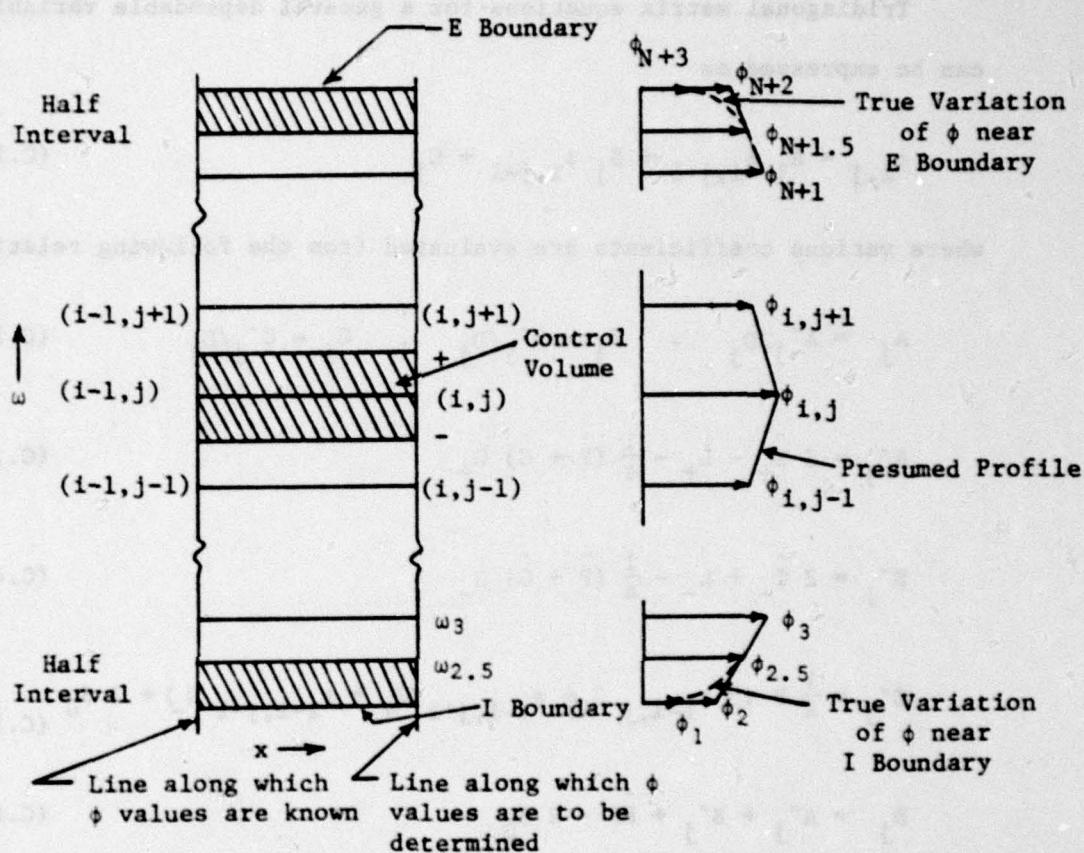


Figure C.1 Location of Nodal Points Referred to in the Finite-Difference Equations

the final results obtained for the coefficients of the finite-difference equations of the conservation equations considered in the present study.

Tridiagonal matrix equations for a general dependable variable, ϕ , can be expressed as

$$\phi_{i,j} = A_j \phi_{i,j+1} + B_j \phi_{i,j-1} + C_j \quad (C.1)$$

where various coefficients are evaluated from the following relations:

$$A_j = A'_j/D_j, \quad B_j = B'_j/D_j, \quad C_j = C'_j/D_j \quad (C.2)$$

$$A'_j = 2 \hat{T}_+ - L_+ - \frac{1}{4} (\hat{P} + \hat{G}) \Omega_+ \quad (C.3)$$

$$B'_j = 2 \hat{T}_- + L_- - \frac{1}{4} (\hat{P} + \hat{G}) \Omega_- \quad (C.4)$$

$$C'_j = \frac{1}{4} \hat{P} (3 \phi_{i-1,j} \Omega_+ + \phi_{i-1,j+1} \Omega_+ + \phi_{i-1,j-1} \Omega_-) + 2 S_U \quad (C.5)$$

$$D_j = A'_j + B'_j + \hat{P} \Omega - 2 S_D \quad (C.6)$$

In these coefficients, $i-1$ and i represent upstream and downstream locations of the integrating region along x -direction, and $j-1$, j , and $j+1$ represent locations along ω -direction. Subscripts $+$ and $-$ denote a half step between j and $j+1$, and $j-1$ and j , respectively (see Figure C.1). Other definitions which have been introduced in the coefficients are:

$$\hat{P} \equiv (\psi_E - \psi_I) / \Delta x \quad \text{where } \Delta x = x_i - x_{i-1} \quad (C.7)$$

$$\hat{G} \equiv (\dot{m}_I - \dot{m}_E) \quad (C.8)$$

$$L_+ \equiv \dot{m}_I - \frac{\hat{G}}{2} (\omega_{j+1} + \omega_j) \quad (C.9)$$

$$L_- \equiv \dot{m}_I - \frac{\hat{G}}{2} (\omega_j + \omega_{j-1}) \quad (C.10)$$

$$\Omega_+ \equiv \omega_{j+1} - \omega_j, \quad \Omega_- \equiv \omega_j - \omega_{j-1}, \quad \Omega \equiv \Omega_+ + \Omega_- \quad (C.11)$$

Coefficients for grid point 2:

For $\phi = \bar{u}$:

$$A'_2 = 2\hat{T}_{2.5} - L_{2.5} - \hat{T}_1 - \frac{1}{4}(\hat{P} + \hat{G})\omega_3 + \frac{1}{2}S_D \quad (C.12)$$

$$B'_2 = 2(\hat{T}_1 + \dot{m}_I) \quad (C.13)$$

$$C'_2 = \frac{1}{4}\hat{P}\omega_3 (3\phi_{i-1,2} + \phi_{i-1,3}) + 2S_U \quad (C.14)$$

$$D'_2 = A'_2 + B'_2 + \hat{P}\omega_3 - 2S_D \quad (C.15)$$

Where $T_1 = s(\rho u)_{2.5}$, and it is evaluated from Couette-flow analysis discussed in Appendix B.

For $\phi = H, Y_O$ or Y_F :

$$A'_2 = 2\hat{T}_{2.5} - L_{2.5} - \frac{1}{4}(\hat{P} + \hat{G})\omega_3 + \frac{1}{2}S_D \quad (C.16)$$

$$B'_2 = 0$$

$$C'_2 = \frac{1}{4}\hat{P}\omega_3 (3\phi_{i-1,2} + \phi_{i-1,3}) + 2S_U + 2J_{\text{tot},\phi,I} \quad (C.17)$$

$$D'_2 = A'_2 + 2\dot{m}_I + \hat{P}\omega_3 - 2S_D \quad (C.18)$$

Where $J_{\text{tot}, \phi, I}$ is evaluated from the boundary conditions and the Coutte-flow analysis discussed in Appendix B.

Coefficients for grid point N+2:

For all variables:

$$A'_{N+2} = -2\dot{m}_E \quad (\text{C.19})$$

$$B'_{N+2} = 2\hat{T}_{N+1.5} + L_{N+1.5} - \frac{1}{4} (\hat{P} + \hat{G}) (1-\omega_{N+1}) + \frac{1}{2} S_D \quad (\text{C.20})$$

$$C'_{N+2} = \frac{1}{4} \hat{P} (1-\omega_{N+1}) (3\phi_{i-1, N+2} + \phi_{i-1, N+1}) + 2 S_U \quad (\text{C.21})$$

$$D'_{N+2} = A'_{N+2} + B'_{N+2} + \hat{P} (1-\omega_{N+1}) - 2 S_D \quad (\text{C.22})$$

In Equations (C.19) through (C.22), the gradient of the dependable variable has been set equal to zero, which is in conformity with free-stream boundary conditions.

Mathematical relations for \hat{T}_+ , \hat{T}_- , S_U , and S_D for each dependable variable at grid point (i,j) are given in Table C.1. First derivatives listed in Table C.1 are approximated as:

$$\left. \frac{\partial \phi}{\partial y} \right|_+ = \frac{\phi_{j+1} - \phi_j}{y_{j+1} - y_j} \quad (\text{C.23})$$

$$\begin{aligned} \left. \frac{\partial \phi}{\partial y} \right|_j &= \frac{y_j - y_{j-1}}{(y_{j+1} - y_j)(y_{j+1} - y_{j-1})} (\phi_{j+1} - \phi_j) \\ &+ \frac{y_{j+1} - y_j}{(y_j - y_{j-1})(y_{j+1} - y_{j-1})} (\phi_j - \phi_{j-1}) \end{aligned} \quad (\text{C.24})$$

These equations have second-order accuracy in step size along ω -coordinate. In Table C.1 any variable ϕ referred to \pm location is

Table C.1
Coefficients in the Finite-Difference Equations of Each Dependable Variable

ϕ	$\hat{T}_+(y_{j+1}-y_j)$	$\hat{T}_-(y_j-y_{j-1})$	S_U	S_D
\bar{u}	$\mu_{eff}, +$	$\mu_{eff}, -$	$-\frac{1}{2} \frac{d\bar{p}}{dx} (y_{j+1}-y_{j-1})$	0
\bar{H}	$(\frac{\mu}{P_r})_{eff}, +$	$(\frac{\mu}{P_r})_{eff}, -$	$\frac{1}{2} [(\Gamma_{eff} \frac{\partial \bar{u}^2}{\partial y})_+ - (\Gamma_{eff} \frac{\partial \bar{u}^2}{\partial y})_-]$	0
\bar{Y}_F	$(\frac{\mu}{Sc})_{eff}, +$	$(\frac{\mu}{Sc})_{eff}, -$	$-\frac{1}{2} C_\omega (\bar{\rho} \sqrt{K} \frac{\partial \bar{Y}_F}{\partial y})_j (y_{j+1}-y_{j-1})$	0
\bar{Y}_{OF}	Same	Same	0	0
K	$(\mu + \frac{\mu_t}{C})_+$	$(\mu + \frac{\mu_t}{C})_-$	$\frac{1}{2} (\mu_t (\frac{\partial \bar{u}}{\partial y})^2)_j (y_{j+1}-y_{j-1})$	$-\frac{1}{2} (\bar{\rho} \frac{\epsilon}{K})_j (y_{j+1}-y_{j-1})$
ϵ	$(\mu + \frac{\mu_t}{C})_+$	$(\mu + \frac{\mu_t}{C})_-$	$C_3 S_{U_K} (\frac{\epsilon}{K})_j$	$-\frac{1}{2} C_4 S_{D_K}$

Where $\Gamma_{eff} = \mu_{eff} - (\frac{\mu}{P_r})_{eff}$

found from the average between ϕ_j and ϕ_{j+1} .

Expressions for mass entrainment rate (\dot{m}_E) at the external boundary are obtained from the degenerate form of Equation (77) as $\omega \rightarrow 1$; using finite-difference approximations, we get

$$\dot{m}_{E,U} = \frac{-2\mu_{\text{eff}, N+1.5}}{(y_{N+2} - y_{N+1})} \quad (\text{C.25})$$

$$\dot{m}_{E,H} = \frac{-2(\mu/\text{Pr})_{\text{eff}, N+1.5}}{(y_{N+2} - y_{N+1})} \quad (\text{C.26})$$

$$\dot{m}_{E,K} = \frac{-2(\mu + \frac{\mu_t}{C_1})_{N+1.5}}{(y_{N+2} - y_{N+1})} \quad (\text{C.27})$$

Where $(y_{N+2} - y_{N+1})$ is the step size at the external boundary. Maximum value calculated from Equations (C.25) through (C.27) were used in the numerical solutions. Entrainment rate at the inner boundary is given by $\dot{m}_I = \rho_s r_b$.

y distribution corresponding to a given ω distribution is obtained from the numerical integration of the following equation:

$$dy = \frac{\psi_E - \psi_I}{\rho u} d\omega \quad (\text{C.28})$$

This equation is obtained from the definition of the coordinate transformations, Equations (74) and (75).

ω -Distribution: In the present study, the boundary layer was divided into 100 cross-stream intervals. Variable grid size was used along ω -direction. The following formula was used to specify the ω -distribution:

$$\begin{aligned} \omega_1 &= \omega_2 = 0 \\ \omega_j &= \Delta\omega \left(\frac{\Delta\omega^{j-2}}{\Delta\omega_{\text{inc-1}}} \right), \quad j = 3, 4, \dots, 54 \end{aligned} \quad (\text{C.29})$$

$$\omega_j = \omega_{j-1} + (1 - \omega_{54})/48, \quad j = 55, 56, \dots, N+2 \quad (C.30)$$

$$\omega_{N+3} = \omega_{N+2} = 1$$

where

$$\Delta\omega = 0.1 (\Delta\omega_{inc}^{50} - 1) / (\Delta\omega_{inc}^{50} - 1) \quad (C.31)$$

and the increment in $\Delta\omega$, $\Delta\omega_{inc} = 1.15$

Step Size Along x-Direction: Step size, Δx , along the x-direction was set equal to 0.3 times the boundary layer thickness (y_{N+3}). However, a limit was set on Δx by the equation:

$$\Delta x \leq 0.01 (\psi_E - \psi_I) / (\dot{m}_I - \dot{m}_E) \quad (C.32)$$

Δx found from the above equation is dependent on the fraction of the mass entrained by the boundary layer during a forward step in the solution procedure.

Initial Temperature Distribution: In order to start the numerical computations, the temperature distribution was guessed and evaluated from the following relation:

$$T_j = T_{ps} + (T_\infty - T_{ps}) \frac{[1 - \exp(\omega_j)]}{[1 - \exp(\omega_{N+3})]}, \quad j = 1, 2, \dots, N+3 \quad (C.33)$$

For the velocity and species mass fraction, uniform initial distributions were assumed: $\bar{u} = U_\infty$, $Y_F = 0.001$, $Y_{OF} = 0.001$

Initial K and ϵ Distributions: The distributions of K and ϵ were evaluated from the following equations (also used in Reference 69):

$$K = \frac{u^2}{\sqrt{C_u}} \cos^2\left(\frac{1}{2} \pi y/\delta\right) \quad (C.34)$$

$$\varepsilon = C_{\mu} \frac{K^{3/2}}{\ell_d} \quad (C.35)$$

$$\ell_d = \begin{cases} k C_{\mu}^{1/4} y & \text{for } ky \leq 0.096 \\ 0.09 C_{\mu}^{1/4} \delta & \text{for } ky > 0.096 \end{cases} \quad (C.36)$$

APPENDIX D

PARAMETRIC STUDY IN THE EROSION-BURNING TEST-RIG DESIGN

The test rig consists of four major components: the driving motor, the test chamber, the feed mechanism chamber and the pressure equalizer chamber (see Figure D.1). The design of these components of the test rig depends on the gas dynamic operating conditions for pressure, temperature, and velocity required in the test chamber. Therefore, the equations of mass and energy balance in the driving motor and the test chamber are considered. Through these equations, the effect of various geometric inputs of the test rig on the gas dynamic operating condition can be studied.

The equations for mass and energy balance in the driving motor and test chamber can be derived by considering a control volume in each of these components, and introducing the following assumptions:

1. All the properties are functions of time only, and
2. Perfect gas law is valid.

Mass balance in the driving motor:

$$\left(\frac{dm}{dt}\right)_d = \dot{m}_{ign} + (\dot{m}_b)_d - (\dot{m}_{exit})_d \quad (D.1)$$

Energy balance in the driving motor:

$$\left(\frac{d(me)}{dt}\right)_d = \dot{m}_{ign} h_{ign} + (\dot{m}_b C_p T_f)_d - (\dot{m}_{exit} H_{exit})_d - (\dot{q}_{loss})_d \quad (D.2)$$

where the subscript d refers to the driving motor.

Using $m = \rho V$ and perfect gas law

$$p = \frac{\rho R_u T}{W}, \quad e = C_v T \quad (D.3)$$

we find,

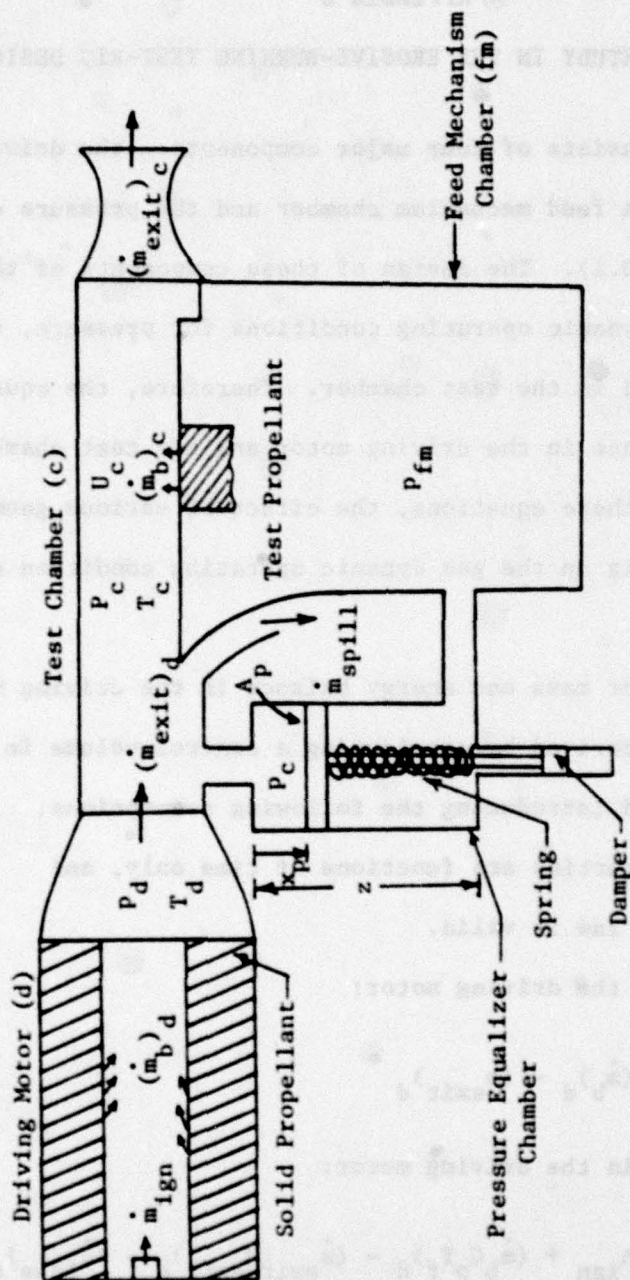


Figure D.1 Schematic Diagram Showing Mass Flow Rates in and out of Each Chamber of the Test Rig

$$\frac{dm}{dt} = \rho \frac{dV}{dt} + \frac{V}{RT} \frac{dp}{dt} - \frac{Vp}{T} \frac{dT}{dt} \quad (D.4)$$

From Equations (D.3) and (D.4), we have

$$\frac{d(me)}{dt} = C_v \rho T \frac{dV}{dt} + \frac{C_v V}{R} \frac{dp}{dt} \quad (D.5)$$

Substituting Equations (D.4) and (D.5) into Equations (D.1) and (D.2) respectively, we have

$$\left\{ \rho \frac{dV}{dt} + \frac{V}{RT} \frac{dp}{dt} - \frac{Vp}{T} \frac{dT}{dt} \right\}_d = \dot{m}_{ign} + (\dot{m}_b)_d - (\dot{m}_{exit})_d \quad (D.6)$$

$$\left\{ C_v \rho T \frac{dV}{dt} + \frac{C_v V}{R} \frac{dp}{dt} \right\}_d = \dot{m}_{ign} h_{ign} + (\dot{m}_b C_p T_f)_d - (\dot{m}_{exit} H_{exit})_d - (\dot{q}_{loss})_d \quad (D.7)$$

In the driving motor, the rate of change of volume is given by the following equation:

$$\left(\frac{dV}{dt} \right)_d = (r_b A_b)_d \quad (D.8)$$

Multiplying Equation (D.6) by $(C_v T)_d$, subtracting from Equation (D.7), and using Equation (D.8), we finally get:

$$\begin{aligned} \left(\frac{dT}{dt} \right)_d &= \left(\frac{\gamma-1}{\rho R V} \right)_d [(\dot{m}_{ign} h_{ign}) + (\dot{m}_b C_p T_f)_d - (\dot{m}_{exit} H_{exit})_d \\ &\quad - (\dot{q}_{loss})_d - (\dot{m}_{ign} + \dot{m}_b - \dot{m}_{exit})_d \left(\frac{R}{\gamma-1} \right)_d T_d] \end{aligned} \quad (D.9)$$

From Equations (D.7) and (D.8) we get

$$\begin{aligned} \left(\frac{dp}{dt} \right)_d &= \left(\frac{\gamma-1}{V} \right)_d [\dot{m}_{ign} h_{ign} + (\dot{m}_b C_p T_f)_d - (\dot{m}_{exit} H_{exit})_d - (\dot{q}_{loss})_d \\ &\quad - \left(\frac{R \rho}{\gamma-1} \right)_d (r_b A_b T)_d] \end{aligned} \quad (D.10)$$

Mass balance in the test chamber:

$$\left(\frac{dm}{dt}\right)_c = (\dot{m}_{exit})_d + (\dot{m}_b)_c - (\dot{m}_{exit})_c - (\dot{m}_{spill})_c \quad (D.11)$$

Energy balance in the test chamber:

$$\begin{aligned} \left(\frac{d(me)}{dt}\right)_c &= (\dot{m}_{exit} H_{exit})_d + (\dot{m}_b C_p T_f)_c - (\dot{m}_{exit} H_{exit})_c \\ &\quad - (\dot{m}_{spill} H_{spill})_c - (\dot{q}_{loss})_c \end{aligned} \quad (D.12)$$

The subscript c refers to the test chamber. A simplification of Equations (D.11) and (D.12) similar to that followed earlier for the driving motor results in the following equations:

$$\begin{aligned} \left(\frac{dT}{dt}\right)_c &= \left(\frac{\gamma-1}{\rho R V}\right)_c [(\dot{m}_{exit} H_{exit})_d + (\dot{m}_b C_p T_f)_c - (\dot{m}_{exit} H_{exit})_c \\ &\quad - (\dot{m}_{spill} H_{spill})_c - (\dot{q}_{loss})_c - \{(\dot{m}_{exit})_d + (\dot{m}_b)_c - (\dot{m}_{exit})_c \\ &\quad - (\dot{m}_{spill})_c\} \left(\frac{R}{\gamma-1}\right)_c T_c] \end{aligned} \quad (D.13)$$

$$\begin{aligned} \left(\frac{dp}{dt}\right)_c &= \left(\frac{\gamma-1}{V}\right)_c [(\dot{m}_{exit} H_{exit})_d + (\dot{m}_b C_p T_f)_c - (\dot{m}_{exit} H_{exit})_c \\ &\quad - (\dot{m}_{spill} H_{spill})_c - (\dot{q}_{loss})_c - \left(\frac{R \rho}{\gamma-1}\right)_c \left(\frac{dV}{dt}\right)_c T_c] \end{aligned} \quad (D.14)$$

In Equations (D.9) through (D.10) and Equations (D.13) and (D.14), \dot{m}_{exit} , and H_{exit} are calculated by the following equations:

$$\dot{m}_{exit} = C_d A_{exit} \rho \sqrt{2 C_p T \left\{ \left(\frac{p_{exit}}{p}\right)^{\frac{2}{\gamma}} - \left(\frac{p_{exit}}{p}\right)^{\frac{1+\gamma}{\gamma}} \right\}} \quad (D.15)$$

$$H_{exit} = C_p T + \frac{U^2}{2} \quad (D.16)$$

Equation (D.15) is based on the assumption of isentropic flow in a nozzle.

We can also write for the volume in the test chamber,

$$V_c = (V_o)_c + A_p x_p \quad (D.17)$$

$$\frac{dV_c}{dt} = A_p u_p \quad (D.18)$$

where $(V_o)_c$ is the volume of the test chamber when $x_p = 0$ (see Figure D.1). u_p and x_p depend on the pressure difference across the piston. The pressure equalizer chamber consists of a steel cylinder which contains a piston, a spring, and a damper. A force balance for the piston, spring, and damper system with the cylinder gives the following equations:

$$\frac{du_p}{dt} = \frac{1}{m_p} [(p_c - p_{fm}) A_p - d_c u_p - \zeta_k x_p] \quad (D.19)$$

$$\frac{dx_p}{dt} = u_p \quad (D.20)$$

where m_p is the piston mass, d_c is the damping factor, ζ_k is the spring constant. To evaluate p_{fm} , we assume a polytropic compression of the gas in the feed mechanism chamber. Therefore, we have

$$p_{fm} = (p_{fm})_o \left[\frac{(V_o)_{fm} + \frac{A_p Z}{p}}{(V_o)_{fm} + (Z - x_p) A_p} \right]^n \quad (D.21)$$

where $(V_o)_{fm}$ is the volume in the feed mechanism chamber excluding the free volume in cylinders, $(p_{fm})_o$ is the initial pressure, and n is the exponent in the polytropic compression.

Surface temperature of the propellant sample in the test chamber is given by the following equation

$$\left(\frac{dT_{ps}}{dt}\right)_c = \frac{4 \alpha_s h_{conv}^2 (T_c - T_{ps})^3}{3 \lambda_s^2 (T_{ps} - T_{pi}) (2 T_c - T_{ps} - T_{pi})} \quad (D.22)$$

This equation is derived from the transient, one-dimensional heat conduction equation in a solid propellant (see Reference 77).

In Equation (D.22) the convective heat transfer coefficient, h_{conv} , is calculated from the Dittus-Boelter equation. T_{ps} is assumed constant after it has equalled the ignition temperature.

Equations (D.8) through (D.10), (D.13), (D-14), and (D.18) through (D.22) were solved on the computer, using fourth-order Hamming's Modified Predictor-Corrector Scheme. The properties used in the calculations are listed in Table D.1. A parametric study was performed to determine the effect of various geometric inputs on the gas dynamic properties: pressure, temperature, velocity, etc., in the test rig. The results of these calculations have been plotted and are shown in Figures D.2 through D.5.

Conclusions drawn from the parametric study are:

1. Steady state conditions for pressure, temperature, and velocity can be achieved in the test chamber after a very short transient interval (see Figures D.2 and D.3).
2. Various gas velocities and pressures can be achieved in the test chamber by controlling the exit-nozzle area, as shown by the results plotted in Figure D.4.
3. Velocity can also be controlled by the variation of height, h_{tc} , in the test chamber, as indicated by the results in Figure D.5.

Table D.1
Properties Used in Parametric Study

Property	Dimensions	Numerical Value
a'	$\text{cm/s}/(\text{atm})^{n'}$	8.812×10^{-2}
$(C_p)_c$	Kcal/Kg-K	0.35
$(C_p)_d$	Kcal/Kg-K	0.35
Pr	-----	1.0
$(T_f)_c$	K	2225
$(T_f)_d$	K	2258
$(T_{\text{ign}})_c$	K	700
T_{pi}	K	298
$(W)_c$	Kg/Kmole	22.01
$(W)_d$	Kg/Kmole	22.01
α	$\text{cm}^{2.8}/\text{s}^{0.2}\text{Kg}^{0.8}$	6.129
$(\alpha_s)_c$	cm^2/s	1.875×10^{-3}
β	-----	105
$(\lambda_s)_c$	Kcal/cm-s-K	9.0×10^{-7}
$(\mu)_c$	Kg/cm-s	5.7×10^{-7}
$(\rho_s)_c$	Kg/cm ³	1.6×10^{-3}
$(\rho_s)_d$	Kg/cm ³	1.6×10^{-3}

$$(r_b)_d = a' p^{n'}$$

$$(r_b)_c = a' p^{n'} + \frac{\alpha G^{0.8}}{x^{0.2}} \exp\left(-\frac{\beta r_b \rho_s}{\rho_\infty U_\infty}\right), \quad \text{Lenoir-Robillard Equation}$$

Erosive-burning law (27)

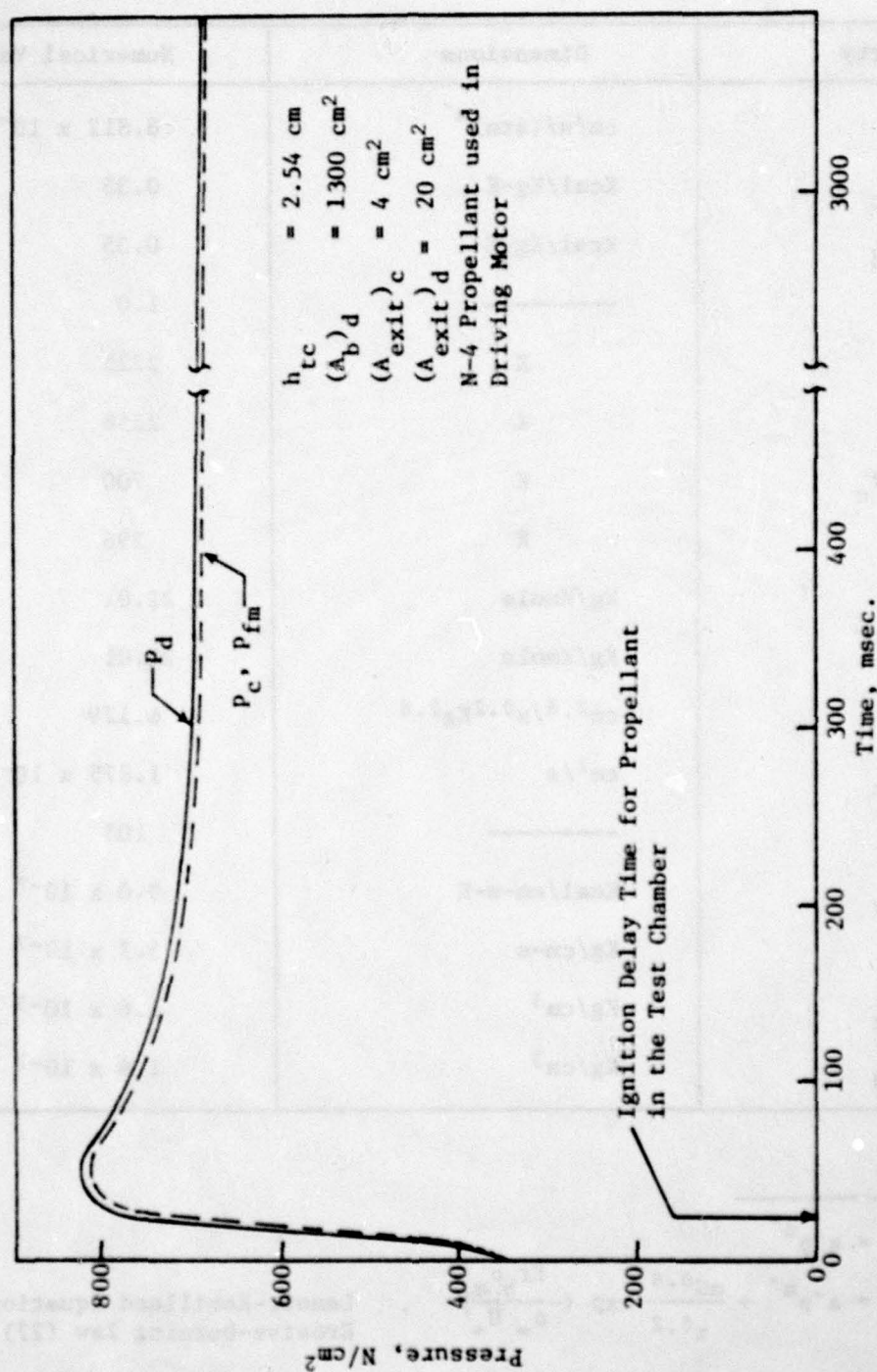


Figure D.2 Calculated Pressure-Time Traces in the Test Rig

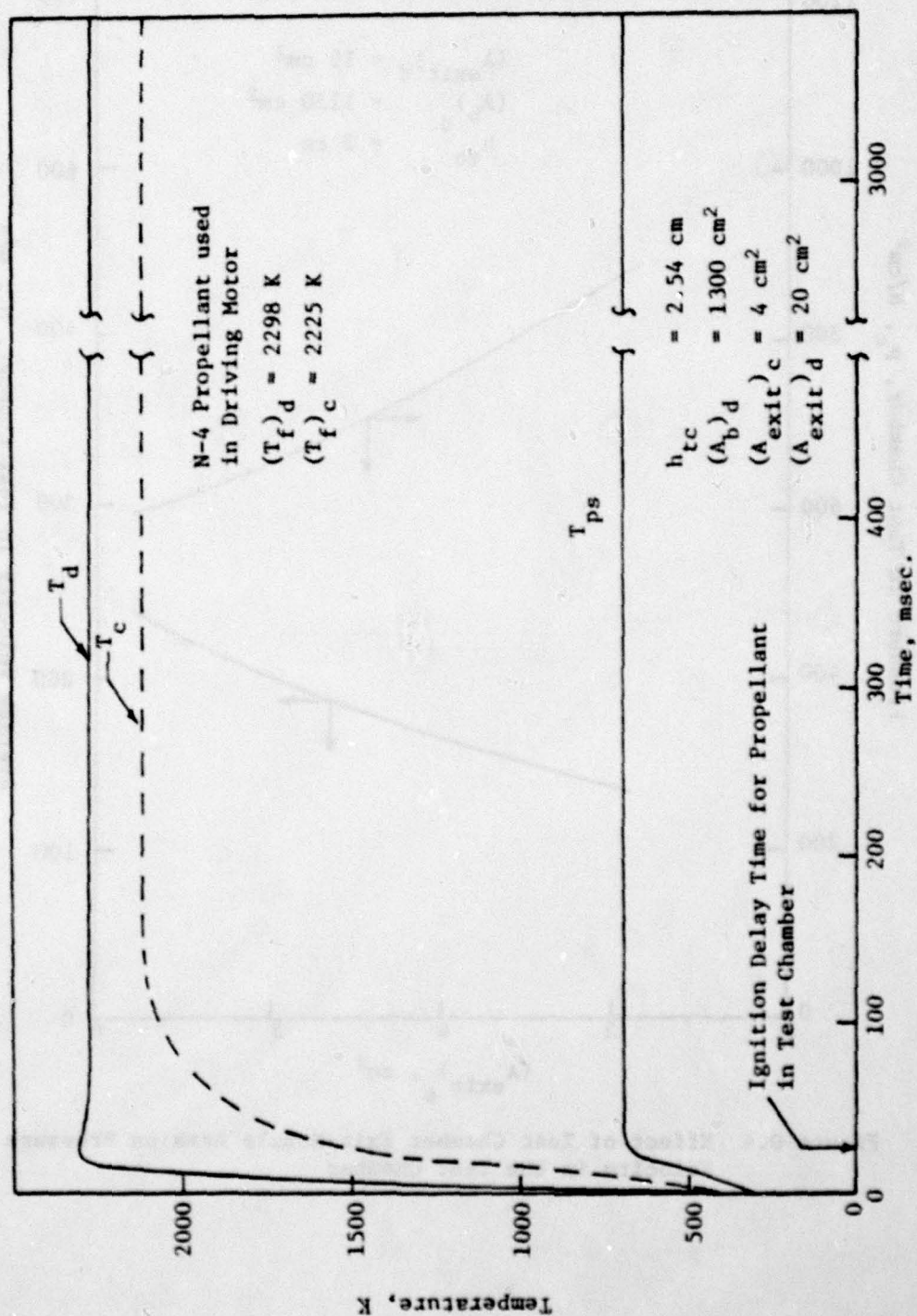


Figure D.3 Calculated Temperature-Time Traces in the Test Rig

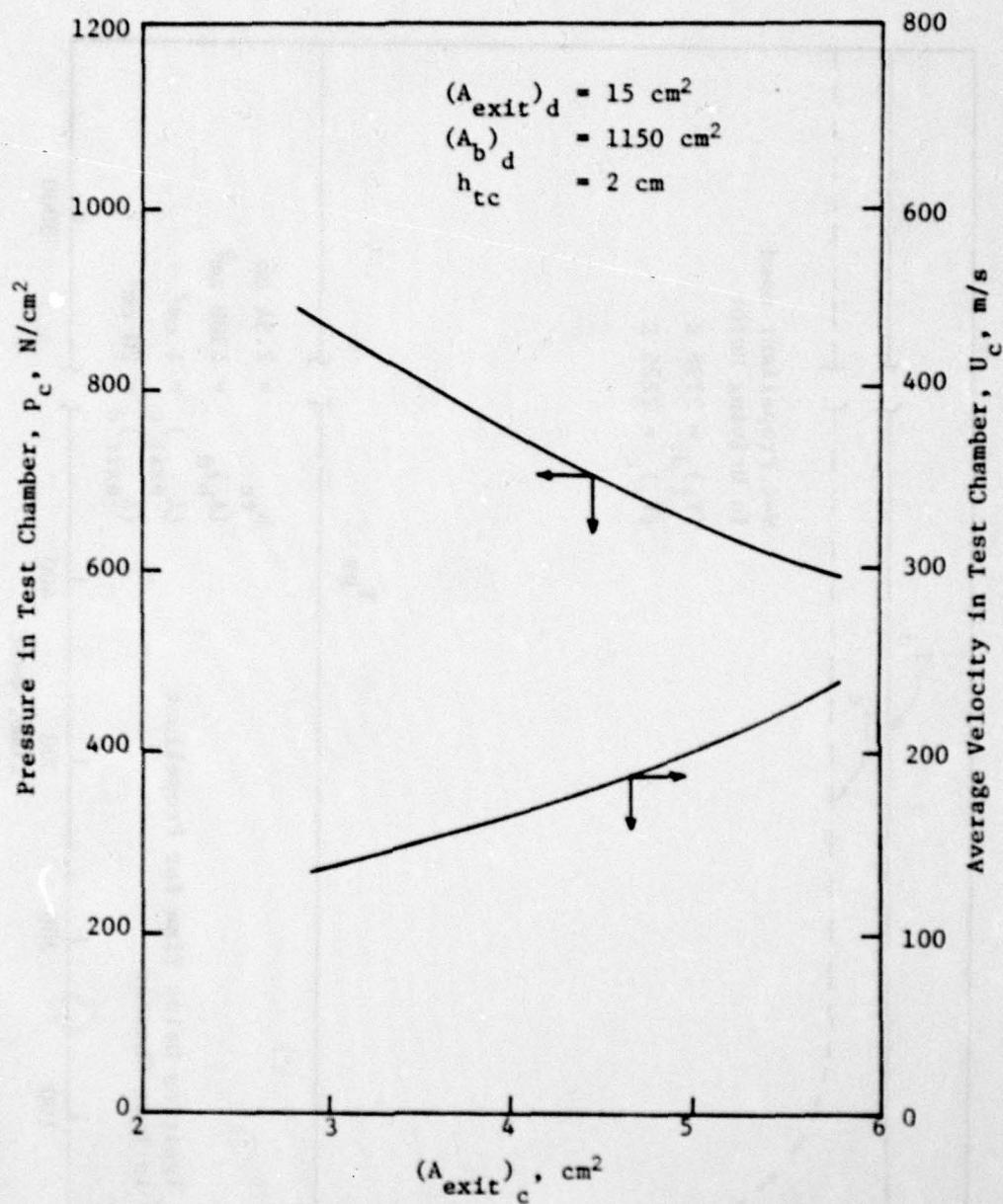


Figure D.4 Effect of Test Chamber Exit-Nozzle Area on Pressure and Velocity in the Test Chamber

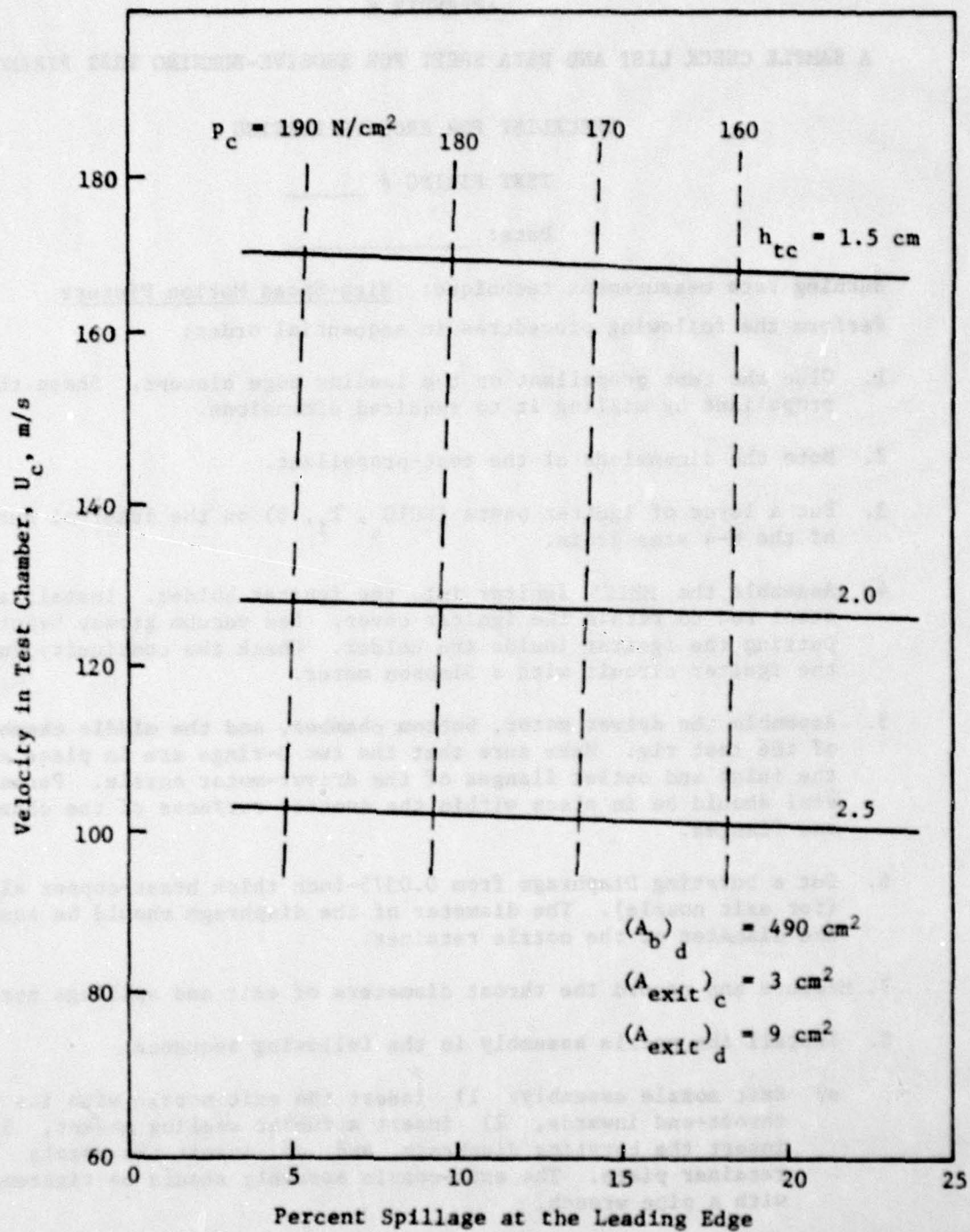


Figure D.5 Effect of Test Chamber Height and Spillage on the Velocity and Pressure in the Test Chamber

APPENDIX E

A SAMPLE CHECK LIST AND DATA SHEET FOR EROSION-BURNING TEST FIRINGS

CHECKLIST FOR EROSION BURNING

TEST FIRING # _____

Date: _____

Burning rate measurement technique: High-Speed Motion Picture

Perform the following procedures in sequential order:

1. Glue the test propellant on the leading edge element. Shape the propellant by milling it to required dimensions.
2. Note the dimensions of the test-propellant.
3. Put a layer of igniter paste ($KClO_4$, T_1 , B) on the internal surfaces of the N-4 star grain.
4. Assemble the MK125 Igniter into the igniter holder. Install a steel rod to retain the igniter cover. Use vacuum grease before putting the igniter inside the holder. Check the continuity in the igniter circuit with a Simpson meter.
5. Assemble the driver motor, bottom chamber, and the middle chamber of the test rig. Make sure that the two O-rings are in place at the inlet and outlet flanges of the driver-motor nozzle. Permatex seal should be in place within the contact surfaces of the chamber and flanges.
6. Cut a bursting Diaphragm from 0.0375-inch thick brass-copper alloy (for exit nozzle). The diameter of the diaphragm should be equal to the diameter of the nozzle retainer.
7. Measure and record the throat diameters of exit and spillage nozzles.
8. Install the nozzle assembly in the following sequence:
 - a) Exit nozzle assembly: 1) insert the exit nozzle with its throat-end inwards, 2) insert a rubber sealing gasket, 3) insert the bursting diaphragm, and 4) insert the nozzle retainer piece. The exit-nozzle assembly should be tightened with a pipe wrench.
 - b) Spillage nozzle assembly: 1) insert the spillage nozzle with its throat-end inwards, and 2) insert the nozzle retainer piece. The spillage-nozzle assembly should be tightened with a crescent wrench.
9. Put a layer of Halocarbon grease (25-5S) on the back, front, and trailing surfaces, and on a small portion of the leading edge of

the test propellant sample. Assemble the leading edge piece with the test rig, with bolts and torque down these bolts.

10. Check to see that the plexiglass window assembly ($1\frac{1}{2} + 1 + \frac{1}{2}$ inches thickness) fits into the steel top chamber window. This may need some filing.
11. Clean the plexiglass window-assembly. Put a thin layer of Halocarbon grease (25-5S) on the side of the sacrificial plexiglass window facing the propellant, but only on the portion that is not blocked by the propellant.
12. Assemble the plexiglass window in the top chamber. A cork gasket may be needed for a tight seal.
13. Assemble the top chamber and steel window-retainer with the test-rig assembly. Use permatex seal for both the chamber surface and the window retainer surface.
14. Torque down all the bolts of the test rig.
15. Make sure that the test-rig-stand assembly is secure, with bolts and nuts tightened.
16. Connect the exhaust gas pipes at spillage and exit-nozzle locations.
17. Put the pressure transducers into their respective locations after the transducer sensitivity for each is noted and the surface of each transducer has been covered with silicon rubber for thermal insulation.
18. Connect water input and output lines to the waterjackets of each transducer. Run the water through the jackets and check for leaks. Turn off the water supply.
19. Test cell power, ignition and transformer switches must be all OFF (down) position prior to connecting camera and igniter wires. Igniter wire plug is disconnected from the lead which is connected to relay box.
20. Switch ON power to charge-amplifier, biomatron, and tape recorder (allow 15 minutes to warm up).
21. Set up camera lights and test to see that they are working.
22. Set up camera and its various connections, including that for the LED driver unit. Check the following:
 - a) Full frame head is connected with the camera.
 - b) Bullet proof glass is attached.
 - c) START/STOP switch on camera speed controller is in STOP position.

- d) Framing rate PPS dial is set, Multiplier dial is set, Break dial is set, servo is set, H/L speed reducer is set, and camera is focused and set at desired f-stop.
 - e) LED driver switch is in ON position.
 - f) Pulse code is set at desired pulses/sec.
 - g) Camera and LED driver electrical plugs are securely inserted in power receptacles.
23. Turn on only the test-cell power and check the following:
- a) LED driver idiot-light is ON.
 - b) Common-time trip indicator on LED driver is not lit.
 - c) Check the functioning of two light emitting diodes.
 - d) Turn test-cell power to OFF.
24. Perform the following on charge amplifiers:
- a) Check the drift of charge amps.
 - b) Check the input voltages to charge amps. These voltages should be based on the transducer sensitivity and pressure scale dial setting on the charge amps.
 - c) Connect transducer cable plugs to the pressure transducers. Clean each plug with Freon TF spray and dry each before connecting.
 - d) Short circuit the positive and ground leads of transducer cable with a screw driver, then clean as in (c). Connect to charge input receptacles on charge amps. Make sure that the connection is made with the charge amp. whose sensitivity dial setting conforms with that on the transducer.
 - e) Clean and cap the calibration receptacle of charge amps.
 - f) Check sensitivity dial setting, pressure scale dial setting, and time-constant setting of charge amps.
 - g) Keep charge/calibration toggle switch on charge mode and ground/operate switch on ground position.
 - h) Both toggle switches on calibration panel are in OFF (up) position, and rotary switch is in a null position.
 - i) Connect charge amp output from calibration panel to tape recorder input channels.
25. Perform the following checks on the Ignition-circuit Relay Box:
- a) Common-Time lead connected (also to camera and tape inputs).
 - b) 50 VAC lead connected to relay from the transformer power source.
 - c) 12 VDC lead connected to electromagnet input of the relay.

26. Perform a pre-ignition test by connecting a fuse wire to the igniter wire and loading the camera with a dummy film, and then follow with steps 43, 45 and 46.
27. Check procedure 19 again.
28. Load the camera with new film. Push micro-switch on the camera upwards, and keep the eye piece blockage knob on the camera in upward position.
29. Load the driver motor with the N-4 star grain.
30. Assemble the flange covers on the igniter end of the driver motor. Make sure that the two O-rings are in place. Torque down the bolts on these flanges after the angle-iron support assembly is in place.
31. Insert the MK125 igniter assembly into the flange cover of the driver motor. Two O-rings should be in place.
32. Tighten down the MK125 igniter assembly by using a chain wrench. Care should be taken in not tightening too much because the igniter wire may be cut.
33. Carefully test the continuity of the igniter wire with the Simpson meter.
34. Make sure the desired tape is mounted on the tape recorder and the location of the tape is recorded on the data sheet.
35. Connect igniter wire to the feed-through (positive) and a bolt (ground) on the igniter assembly.
36. Turn on water supply.
37. Turn on camera lights.
38. Turn on exhaust fan.
39. Close the test cell door.
40. Turn on test-cell power (must be on for at least 20 seconds prior to firing with the camera speed controller).
41. Connect the igniter wire plug to the lead connected to the relay box.
42. Turn on tape recorder and record the test firing number and other information on the voice channel.
43. Turn on DC voltage supply to relay.
44. Unground charge amplifiers.

45. Turn on power supply to the transformer which supplies 50 VAC and 5 Amps to MK125 igniter.
46. Turn on ignition switch.
47. As soon as the test firing is completed, turn the following switches to OFF:
 - a) Ground/Operate switch to ground (down) position on the charge amplifier.
 - b) DC supply switch to relay.
 - c) Test cell power and ignition switches.

DATA SHEET FOR ERODIVE-BURNING EXPERIMENTS

Test Firing # _____

Date _____

TEMPERATURE: T_{room} _____ °F $T_{\text{test cell}}$ _____ °FBurning Rate Measurement Technique: High Speed Motion Picture

INITIAL PROPELLANT DIMENSIONS:

Length, L = _____ cm Width, W_p = _____ cm Thickness, t = _____ cmLength of Tapered Portion from Leading Edge: l = _____ cmExtra Width Left: Window Side: W_{F1} = _____ cm Back Side: W_{B1} = _____ cm W_{F2} = _____ cm W_{B2} = _____ cm

Propellant Type: _____ Propellant Inhibitor: _____ Type of Glue: _____

Igniter: _____ Input Voltage: _____ Igniter Paste on N-4 Grain _____

N-4 Grain: Length = _____ cm Section Code: _____

CAMERA:

Type of Lens _____

F Stop _____

Framing Rate _____ Frames/sec

Time Marker _____ pulses/sec

Remote Firing at _____ ft. of film

Pictures per Frame _____

FILM:

ASA No. _____, Type _____

Black & White _____, Color _____

Type of LED on 2 msec Com. Time _____

Type of LED on Time Marker _____

Film Processing Instructions: _____

PPS Dial: _____, Multiplier: _____,

Brake Dial: _____

Servo: _____, H/L Speed Reducer: _____

NOZZLES AND BURSTING DIAPHRAGMS:

Exit Nozzle:

Throat Diameter: _____ cm Diaphragm Material: _____ cm

Thickness: _____ cm Bursting Pressure: _____ psig

Spillage Nozzle:

Throat Diameter: _____ cm Diaphragm Material: _____ cm

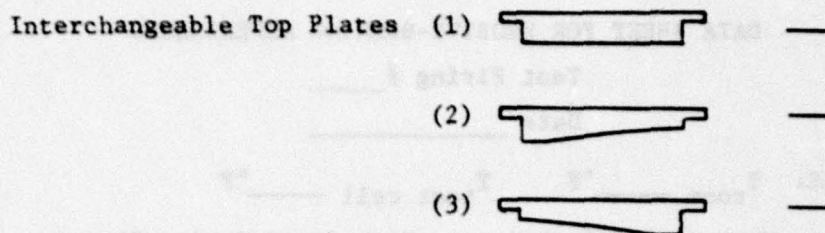
Thickness: _____ cm Bursting Pressure: _____ psig

Type of Window in Contact with Propellant Sample: _____ Thickness: _____ cm

Chamber Prepressurization Condition: Yes _____ psig No _____

No. of Camera Lights _____, Wattage (a) _____, (b) _____,

(c) _____, (d) _____



DATA ACQUISITION:

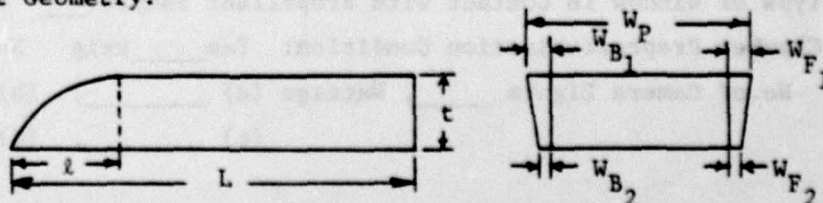
Tape # _____ Tape Location _____ to _____ Tape Speed _____ ips

Pressure Transducer Type and Serial No.				Common Time	Voice
Location					
Transducer Sensitivity					
Charge Amp. No.					
Time Constant Setting					
Range Multiplier					
Sensitivity Setting on Charge Amps.					
Pressure Scale KPSI/volt					
Voltage Divider Channel					
Tape Recorder Channel					

Participants: _____, _____, _____

Remarks:

Propellant Geometry:



APPENDIX F

FREE-STREAM VELOCITY CALCULATION

Direct measurement of the velocity in the test section is very difficult because of the presence of high-temperature and high-pressure gases. Therefore, the free-stream velocity is indirectly calculated from the gas dynamic theory. The mass flow rate through the exit nozzle of the test rig can be written as

$$\dot{m}_{th} = \rho_{th}^* U_{th}^* A_{th}^* \quad (F.1)$$

where the subscript th refers to throat of the nozzle and the superscript * refers to choked flow condition in the throat (in the present tests, gas flow was always choked).

Similarly, the mass flow rate through the test section can be written as

$$\dot{m}_{ts} = \rho_{ts} U_{ts} A_{ts} \quad (F.2)$$

where the subscript ts refers to the conditions in the test section. Test section is identified as the portion of the test chamber above the test propellant sample. A_{ts} is the flow cross-sectional area above the test propellant sample. U and ρ in Equations (F.1) and (F.2) represent the average gas-flow velocity and density. It may be noted that in Equation (F.2), the mass addition due to the burning of the test propellant is included, and the equation is applicable at a location close to the trailing edge of the propellant sample.

Equating Equations (F.1) and (F.2) in order to conserve mass, we get

$$U_{ts} = \left(\frac{\rho_{th}^*}{\rho_{ts}} \right) \left(\frac{A_{th}}{A_{ts}} \right) U_{th}^* \quad (F.3)$$

Squaring Equation (F.3) and using ideal gas law to replace density in terms of pressure and temperature, and also dividing both sides of the equation by γ (noting that $M_{th}^* = 1$), we get

$$M_{ts}^2 = \left(\frac{p_{th}^*}{p_{ts}}\right)^2 \left(\frac{T_{ts}}{T_{th}^*}\right) \left(\frac{A_{th}}{A_{ts}}\right)^2 \quad (F.4)$$

We now use the following isentropic relations (82):

$$\frac{T_o}{T} = 1 + \frac{\gamma-1}{2} M_{ts}^2 \quad (F.5)$$

$$\frac{p_o}{p} = \left(\frac{T_o}{T}\right)^{\frac{\gamma}{\gamma-1}} = \left(1 + \frac{\gamma-1}{2} M_{ts}^2\right)^{\frac{\gamma}{\gamma-1}} \quad (F.6)$$

From Equations (F.5) and (F.6), we find

$$\frac{T_{ts}}{T_{th}^*} = \frac{\gamma+1}{2} / \left(1 + \frac{\gamma-1}{2} M_{ts}^2\right) \quad (F.7)$$

$$\left(\frac{p_{th}^*}{p_{ts}}\right) = \left(1 + \frac{\gamma-1}{2} M_{ts}^2\right)^{\frac{\gamma}{\gamma-1}} / \left(\frac{\gamma+1}{2}\right)^{\frac{\gamma}{\gamma-1}} \quad (F.8)$$

Using Equations (F.7) and (F.8) in Equation (F.4), we obtain the following relation in terms of the Mach number at the test section:

$$M_{ts} = \left[\frac{2}{\gamma+1} + \frac{\gamma-1}{\gamma+1} M_{ts}^2 \right]^{\frac{\gamma+1}{2(\gamma-1)}} \left(\frac{A_{th}}{A_{ts}}\right) \quad (F.9)$$

For the choked flow condition in the exit-nozzle throat, we can also write an equation for the mass flow rate (see Reference 82):

$$\dot{m}_{th} = \left[\frac{\gamma}{R} \left(\frac{2}{\gamma+1}\right)^{\frac{\gamma+1}{2}} \right]^{1/2} \frac{p_o}{\sqrt{T_o}} A_{th} \quad (F.10)$$

where p_o and T_o are the stagnation pressure and temperature, respectively. Equating Equations (F.2) and (F.10), for mass conservation, and using ideal gas law, we get

$$U_{ts} = [\gamma R \left(\frac{2}{\gamma+1} \right)^{\frac{\gamma+1}{\gamma-1}}]^{1/2} \left(\frac{p_o}{p} \right) \left(\frac{T}{T_o} \right) \sqrt{T_o} \left(\frac{A_{th}}{A_{ts}} \right) \quad (F.11)$$

Substituting the isentropic relations, Equations (F.5) and (F.8), in Equation (F.11), we get the expression for average velocity in the test section:

$$U_{ts} = \left(\frac{A_{th}}{A_{ts}} \right) \sqrt{T_o} [\gamma R \left(\frac{2}{\gamma+1} \right)^{\frac{\gamma+1}{\gamma-1}}]^{1/2} \left[1 + \frac{\gamma-1}{2} M_{ts}^2 \right]^{\frac{1}{\gamma-1}} \quad (F.12)$$

The solution of Equations (F.11) and (F.12) gives the average velocity in the test section. To obtain an expression for free-stream velocity, correction should be made in the average velocity to account for the boundary layer developed over the propellant surface and the top plate of the test chamber. Average velocity is defined as

$$U_{ts} = \frac{2}{h_{ts}} \int_0^{h_{ts}/2} u \, dy \quad (F.13)$$

where h_{ts} is the height of the test-section channel. Equation (F.13) can also be written as

$$U_{ts} = \frac{2}{h_{ts}} \left[\int_0^{\delta} u \, dy + \int_{\delta}^{h_{ts}/2} U_{\infty} \, dy \right] \quad (F.14)$$

since beyond the boundary-layer thickness $u = U_{\infty}$.

For the boundary-layer velocity we use a power law distribution of the following type:

$$u = U_{\infty} \left(\frac{y}{\delta} \right)^{\eta} \quad (F.15)$$

Substitution of Equation (F.15) in Equation (F.14), gives the expression for the free-stream velocity, and is given by

AD-A077 351

ATLANTIC RESEARCH CORP ALEXANDRIA VA
TURBULENT BOUNDARY-LAYER ANALYSIS AND EXPERIMENTAL INVESTIGATION--ETC(U)
MAR 79 M K RAZDAN , K K KUO

F/G 21/9.2

F49620-78-C-0016

NL

AFOSR-TR-79-1155

UNCLASSIFIED

3 OF 3

AD-
A077351



END
DATE
FILMED

12-79
DDC

$$U_{\infty} = \frac{U_{ts}}{[1 - (\frac{\eta}{1+\eta}) \frac{2\delta}{h_{ts}}]} \quad (F.16)$$

δ was evaluated from a formula in terms of Reynolds number and downstream distance, x (see Reference 72). η was taken equal to $1/7$.

Stagnation temperature for Equation (F.12), for the present calculations, was obtained from N-4 star grain ballistic data and was equal to 2258 K.

APPENDIX G

TABULATED EXPERIMENTAL DATA FOR EROSION-BURNING RATES AT
VARIOUS PRESSURES AND FREE-STREAM VELOCITIES

Normal burning rate formula: $r_{b_o} = a' p^{n'}$, $a' = 0.2452 \text{ cm/s/(MPa)}^{n'}$
 $n' = 0.41$

Temperature of combustion gases
 generated from N-4 Star grain: $T_o = 2258 \text{ K}$

Propellant Type: AP (75%), PBAA-EPON (25%)

Pressure, MPa	Free-Stream Velocity U_∞ , m/s	Burning Rate, r_b , cm/s
7.2375	319.3	1.213
7.2375	305.6	1.176
7.2375	288.5	1.1278
7.2375	245.0	0.9953
7.2375	231.2	0.9526
7.2375	219.4	0.9165
7.17	274.0	1.0846
7.17	258.0	1.037
7.065	212.5	0.8956
7.065	200.9	0.8619
6.62	189.1	0.829
6.62	178.1	0.7993
6.62	171.7	0.7816
6.41	168.7	0.7731
6.41	162.7	0.7553
6.41	152.0	0.7177
6.066	147.1	0.697
6.0	141.3	0.668
6.0	136.2	0.6375
5.86	131.4	0.6049
5.65	128.3	0.5824
5.65	119.7	0.527

APPENDIX G (continued)

Pressure, MPa	Free-Stream Velocity U_{∞} , m/s	Burning Rate, r_b , cm/s
5.5143	306.2	0.9536
5.5143	294.0	0.91
5.3075	283.3	0.8725
5.2386	273.8	0.841
5.2386	264.1	0.8113
5.1	248.4	0.77
4.963	241.82	0.756
4.963	232.0	0.7385
4.825	225.7	0.73
4.825	217.2	0.721
4.825	208.5	0.714
4.687	203.5	0.71
4.55	196.7	0.705
4.55	192.5	0.701
4.55	185.7	0.692
4.55	178.0	0.6755
4.273	500.0	1.1083
4.273	464.4	1.016
4.136	178.8	0.6524
4.032	509.7	0.921
4.032	486.5	0.8892
4.032	466.6	0.86
4.0	166.3	0.623
4.0	162.2	0.61
4.0	157.4	0.575
4.0	153.2	0.54
3.791	149.4	0.5
3.791	145.0	0.462
3.791	141.2	0.44
3.791	137.7	0.44

APPENDIX G (continued)

Pressure, MPa	Free-Stream Velocity U_{∞} , m/s	Burning Rate, r_b , cm/s
3.584	430.0	0.911
3.1225	393.2	0.79
3.0	406.0	0.756
3.0	373.0	0.633
3.0	354.3	0.60
2.67	336.0	0.59
2.67	333.8	0.585
2.67	327.0	0.565
2.47	318.75	0.546
2.47	315.0	0.5273
2.47	300.5	0.5214
2.4125	290.8	0.503
2.4125	276.7	0.5
2.371	290.4	0.486
2.371	275.3	0.465
2.343	270.7	0.461
2.343	260.0	0.456